Distributed Acoustic Sensing using straight, sinusoidally and helically shaped fibres for seismic applications

Al Hasani, M.M.K.

Important note
To cite this publication, please use the final published version (if applicable).
Please check the document version above.

Distributed Acoustic Sensing using straight, sinusoidally and helically shaped fibres for seismic applications

Distributed Acoustic Sensing using straight, sinusoidally and helically shaped fibres for seismic applications

Dissertation

for the purpose of obtaining the degree of doctor
at Delft University of Technology,
by the authority of the Rector Magnificus, prof. dr. ir. T.H.J.J. van der Hagen,
chair of the Board for Doctorates,
to be defended publicly on
Monday, February 5th 2024 at 15 o'clock

by

Musab Mansoor Khalfan AL HASANI

Master of Science in Geophysics, Curtin University, Australia
born in Muscat, Oman

This dissertation has been approved by the promotors:

Dr. ir. G. G. Drijkoningen
Prof. dr. ir. C. P. A. Wapenaar

Composition of the doctoral committee:

Rector Magnificus	chairman
Dr. ir. G. G. Drijkoningen	Delft University of Technology
Prof. dr. ir. C. P. A. Wapenaar	Delft University of Technology

Independent members:

Prof dr. K.A. Innanen	University of Calgary, Canada
Dr. T. Dean	Anglo American, Australia
Prof dr. L.G. Evers	Delft University of Technology
Dr. T.A. Bogaard	Delft University of Technology
Prof dr. Z. Li	Delft University of Technology

Cover illustration: Ola Al Salhi with the help of DALL-E.

Typesetting system: L^AT_EX.

An electronic version of this dissertation is available at http://repository.tudelft.nl/.

To my family and friends.

Summary

Distributed Acoustic Sensing (DAS) is a versatile dynamic strain sensing method that has been adopted for a wide range of seismic applications. In DAS, optical fibres are interrogated and used as sensors, where a strain or strain-rate measurement is made along a specific length of the fibre, called the gauge length. Its main appeal is the spatially dense data over long distances. The main limitations of DAS, however, are that it is mainly sensitive along the axial direction of the fibre and that the signal-to-noise ratio is worse than that of standard geophones. The first issue limits its adoption in surface reflection seismic when the fibre is deployed horizontally. Also, due to the very nature of the measurement (i.e. elongation and contraction of the fibre), it is commonly considered as a single-component measurement, therefore it lacks the information from the other components.

This thesis studies the potential of obtaining multi-component information from DAS as well as investigating the use of combined fibre configurations for surface-seismic applications. We approach this by examining several fibre-shaping approaches with static and dynamic strain measurements. First, the concept of the sinusoidally shaped fibre is examined to make a directional strain sensor in a direction other than the fibres' axial direction using a static-strain approach. Secondly, the combined use of straight and helically wound fibres for obtaining multi-component information from DAS data as well as assessing the usefulness of using such a combination is investigated in a surface-seismic setting.

Using the sinusoidally shaped fibre, two approaches are investigated. The first approach involves the use of the sinusoidally shaped fibre embedded in a homogenous material. An analytical model is presented to describe what happens to the deformed fibre in three main directions, which was validated via a finite-element model. Along with the model, loading experiments were performed on a sinusoidally shaped fibre embedding in a polyurethane-type (i.e. called Conathane®) strip in the following directions: in-line (i.e. transversal in-plane with the sinusoidal fibre), broadside (i.e. perpendicular to the sinusoidal fibre), and along-strip (i.e. along the strip's

longest dimension). We saw that the fibre is mainly sensitive to the in-line and broadside directions, and it is slightly more sensitive in the in-line direction relative to the broadside direction. We also saw that the geometrical parameters of the fibre, as well as the mechanical properties of the embedding material, affect its directional sensitivity. This is exploited in the second approach where the embedding material is now adapted to a low Poisson's ratio metamaterial as well as further adaptations in the geometry of the fibre, aiming to create a unidirectional strain sensor. Experimental results showed improvements in the sensitivity but not as much as predicted by the analytical or numerical modelling.

Using DAS in field settings, multiple configurations of straight (SF) and helically wound fibres (HWF) with different wrapping angles (α) were buried in a 2-m trench in farmland in the province of Groningen in the Netherlands. Significant amplitude differences are observed between the straight and helically wound fibres. It is observed that shaping the fibre into a helix dampens the amplitude inside the surface wave significantly. Also, a polarity flip is observed with the use of HWF with a wrapping angle of 30°. This hints that there is a contribution of the vertical component on the response measured by the HWF as also supported by the theoretical models. The reflection response is also examined using a set of engineered SF and HWF fibres. The main seismic reflections are present in both fibres with higher amplitude in SF compared to HWF, contrary to what was expected. Also, using post-stack images we see that the SF and HWF provide reflection structural images comparable to surface-deployed geophones but with an (expected) lower signal-to-noise ratio. We show that the combined use of SF and HWF is useful, as reflections were better shown for the shallow section, unlike HWF which provided better reflections in deeper sections.

Furthermore, we discuss the effect of gauge length on the retrieval of surface waves along with the use of different fibre shapes using active and passive sources. With the active-source data, we show that the gauge length plays an essential role in the retrieval of surface waves depending on their wavelength range, as it might cause distortions in the waveform which appears as notches in the (frequency, horizontal-wavenumber)–domain, as well as complicates picking the dispersion curves of these waves. On the other hand, the helically wound fibres might require a longer gauge length to retrieve the surface wave properly. This decreased sensitivity of the helically wound fibres is also shown from virtual shots obtained by passive interferometry as well as a recorded earthquake in the area.

Samenvatting

Distributed Acoustic Sensing (DAS) is een veelzijdige methode voor dynamische rek-sensoren die is overgenomen in een breed scala van seismische toepassingen. Bij DAS worden optische vezels "ondervraagd" en gebruikt als sensoren, waarbij een meting van rek of de tijds-afgeleide ervan wordt uitgevoerd langs een specifieke lengte van de vezel die de meetlengte wordt genoemd. Het belangrijkste voordeel is de ruimtelijk dichte data over lange afstanden. De belangrijkste beperkingen van DAS zijn echter dat het voornamelijk gevoelig is langs de axiale richting van de vezel en dat de signaal-ruis verhouding slechter is dan die van standaard geofoons. Het eerste punt beperkt het gebruik ervan in oppervlakte reflectie seismiek wanneer de vezel horizontaal wordt ingezet. Ook wordt het, vanwege de aard van de meting (uitrekking en inkrimping van de vezel), doorgaans beschouwd als een enkelvoudige meting, waardoor het informatie mist van de andere componenten.

Dit proefschrift onderzoekt de mogelijkheid om multi-component informatie uit DAS te verkrijgen en onderzoekt het gebruik van gecombineerde vezelconfiguraties voor oppervlakte-seismische toepassingen. We benaderen dit door verschillende vezelvormingconfiguraties te onderzoeken met statische en dynamische rekmetingen. Ten eerste wordt het concept van de sinusvormig gevormde vezel onderzocht om een directionele reksensor te maken in een richting anders dan de axiale richting van de vezels met behulp van een statische rekbenadering. Ten tweede wordt het gecombineerde gebruik van rechte en helisch gewonden vezels onderzocht om multi-component informatie uit DAS-gegevens te verkrijgen, evenals de bruikbaarheid van een dergelijke combinatie in een oppervlakte-seismische opzet.

Met behulp van de sinusvormig gevormde vezel worden twee benaderingen onderzocht. De eerste benadering omvat het gebruik van de sinusvormig gevormde vezel die is ingebed in een homogeen materiaal. Er wordt een analytisch model gepresenteerd om te beschrijven wat er gebeurt met de gedeformeerde vezel in drie hoofdrichtingen, wat werd gevalideerd via een eindige-elementenmodel. Samen met dat werden belastingsexperimenten uitgevoerd op een sinusvormig gevormde vezel

die is ingebed in een polyurethaan-type (zgn. Conathane®) strip in de volgende richtingen: in-lijn (d.w.z. dwars in het vlak van de sinusvormige vezel), breedzijde (d.w.z. loodrecht op de sinusvormige vezel) en langs de strip (d.w.z. langs de langste afmeting van de strip). We zagen dat de vezel voornamelijk gevoelig is voor de in-lijn en breedzijde richtingen, en dat deze enigszins gevoeliger is in de in-lijn richting ten opzichte van de breedzijde richting. We zagen ook dat de geometrische parameters van de vezel, evenals de mechanische eigenschappen van het inbeddings-materiaal, van invloed zijn op de directionele gevoeligheid. Dit wordt benut in de tweede benadering, waarbij het inbeddingsmateriaal nu wordt aangepast aan een metamateriaal met een lage Poisson-verhouding, evenals verdere aanpassingen in de geometrie van de vezel om een eenrichtingsreksensor te creëren. Experimentele resultaten toonden verbeteringen in de gevoeligheid, maar niet zo veel als voorspeld door de analytische of numerieke modellering.

Bij het gebruik van DAS in veldomstandigheden zijn meerdere configuraties van rechte (SF) en helisch gewonden vezels (HWF) met verschillende wikkelhoeken (α) begraven in een 2 meter diepe sleuf op een boerderij in de provincie Groningen in Nederland. Er worden aanzienlijke verschillen in amplitude waargenomen tussen de rechte en helisch gewonden vezels. Er wordt waargenomen dat het vormen van de vezel tot een helix de amplitude binnen de oppervlaktegolf aanzienlijk dempt. Ook wordt een polariteitsomkering waargenomen bij het gebruik van HWF met een wikkelhoek van 30°. Dit wijst in de richting dat de verticale component bijdraagt via deze wikkelhoek, zoals ook wordt ondersteund door de theoretische modellen. De reflectierespons wordt ook onderzocht met behulp van een reeks geëngineerde SF- en HWF-vezels. De belangrijkste seismische reflecties zijn aanwezig in beide vezels, met een hogere amplitude in SF in vergelijking met HWF, tegenovergesteld van wat verwacht was. Ook met behulp van post-stack beelden zien we dat SF en HWF vergelijkbare reflectiestructurele beelden bieden als oppervlakte-geplaatste geofoons, maar met een (verwachte) lagere signaal-ruisverhouding. We laten zien dat het gecombineerde gebruik van SF en HWF nuttig is, aangezien reflecties beter worden getoond voor het ondiepe deel, in tegenstelling tot HWF, dat betere reflecties voor het diepere deel biedt.

Bovendien bespreken we het effect van de meetlengte op de verkrijging van op-pervlaktegolven, samen met het gebruik van verschillende vezelvormen met actieve en passieve bronnen. Met de actieve-bron gegevens laten we zien dat de meetlengte een essentiële rol speelt bij de verkrijging van oppervlaktegolven, afhankelijk van hun golflengtebereik, omdat dit vervormingen in de golfvorm veroorzaakt, wat zich uit als inkepingen in het (frequentie, horizontale-golfgetal)-domein, evenals proble-men bij het bepalen van de dispersiecurven van deze golven. Aan de andere kant zouden de helisch gewonden vezels mogelijk een langere meetlengte vereisen om de oppervlaktegolf correct te verkrijgen. Deze verminderde gevoeligheid van de helisch gewonden vezels wordt ook aangetoond vanuit virtuele opnames verkregen door pas-sieve interferometrie, evenals een opgenomen aardbeving in het gebied.

Contents

1

Introduction

'Thus, the photons which constitute a ray of light behave like intelligent human beings: out of all possible curves they always select the one which will take them most quickly to their goal"

Max Planck

Optical fibre sensors have been attracting attention for the last 50 years due to their versatility and flexibility. Their story begins in the mid-1960s with the Fotonic sensor, which was used to locate the position of a gap between two fibres [*Culshaw and Kersey*, 2008]. Later, advances in creating low-loss fibre in the late 1970s allowed the emergence of measuring the optical properties of light travelling in optical fibres [*Hartog*, 2017]. A decade later, optical fibre sensors started to be adopted for physical sensing such as measuring strain and temperature; most of these early adoptions were point sensors [*Culshaw and Kersey*, 2008; *Udd*, 1995]. Another application of optical fibre sensors is Fibre Bragg Gratings (FBGs); these quasi-distributed sensors can be used for measuring strain [*Grattan and Meggitt*, 2000]. An FBG is a refractive index modulation of an in-fibre piece to a narrow wavelength band that acts as a reflector of the light within that band which will be shifted if the fibre is strained [*Hartog*, 2017; *Paschotta*, 2008]. Distributed fibre sensors started to appear after that, giving an opportunity to obtain cheaper and denser measurements for temperature and strain. The basic idea of most current distributed fibre-optic systems is based on *Dakin and Lamb* [1990]. A review of this early work, which covers a wide range of applications of distributed sensors, is written by *Dakin* [1993].

For distributed strain sensing, two physical scattering mechanisms are exploited; these are Brillouin and Rayleigh scattering. Sensors based on Brillouin scattering have the benefit of measuring absolute strain values. In contrast, Rayleigh-based sensors, commonly known as Distributed Acoustic Sensing (DAS) or Distributed

Vibrations Sensing (DVS), have superior strain sensitivity in terms of spatial and strain resolutions compared to Brillouin-based systems; hence they are more suitable for geophysical applications [*Masoudi and Newson*, 2017a, 2016]. An overview of the following relevant topics is presented in this chapter:

- The physics of light propagation in optical fibres.

- Losses, dispersion and scattering in optical fibres.

- Dynamic-strain measurements with optical fibres.

- Applications of DAS in geophysics.

- Fibre broadside sensitivity: reality and possible solutions.

This is followed by the section on the research questions and the outline of the thesis.

1.1   Light propagation in optical fibres

■ 1.1.1   Wave-equation representation

An optical fibre is a circular waveguide that traps an electromagnetic wave propagating from one end to the other. To describe an electromagnetic wave, a derivation of the wave equation based on Maxwell's equations is needed, where the wave equation is then solved to describe the different ways or modes, that light propagates through the fibre. As it is an electromagnetic wave, it has both electric and magnetic components oscillating normally to each other. It is usually described by solving a wave equation of an oscillating electric field $\vec{E}$ in cylindrical coordinates. The wave equation describing $\vec{E}$ as a function of the position along the fibre x, the radius r that is the distance from the centre of the fibre, and the angle θ in the x-transformed Fourier domain is given by:

$$\left(\frac{1}{r} \frac{\partial}{\partial r} \tilde{E} + \frac{\partial^2}{\partial r^2} \tilde{E} \right) + \frac{1}{r^2} \frac{\partial^2}{\partial \theta^2} \tilde{E} - k_x^2 \tilde{E} = -k^2 \tilde{E}, \tag{1.1.1}$$

where k is the wavenumber inside a medium with refractive index n and angular frequency ω (i.e. $k = n\,\omega/c$). After solving equation 1.1.1, multiple solutions could result depending on the parameters of the fibre, namely the size and the refractive index of the core (n_1) and cladding (n_2). Full derivation and solutions can be found in *Mitschke* [2010]. These solutions are called fibre modes. For linearly polarised light (i.e. the field intensity distribution being the same at any distance x), they can be described by **LP$_{lm}$** convention [*Paschotta*, 2008]. The subscripts l and m denote the azimuthal and radial distribution, respectively. Theoretical **LP** modes intensity distribution across an optical fibre showing different modes is illustrated in Figure 1.1. The common propagation mode used for our applications is the fundamental mode **LP$_{01}$** and I refer to the fibres used in the work of this thesis as single-mode (SM) fibres. We see in the figure that the **LP$_{01}$** mode closely resembles a Gaussian function. Multi-mode fibres, on the other hand, are commonly used for

other sensing methods like distributed temperature sensing [*Hartog et al.*, 1985]. Further discussion of higher fibre modes is out of the context of this overview.
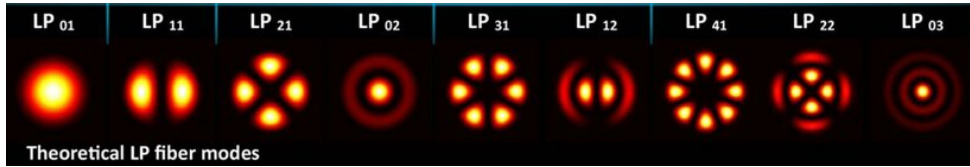
Figure 1.1: *Illustration of modelled linearly polarised (LP) fibre modes showing the light intensity in a cross-section of a fibre. Adapted from Velázquez-Benítez et al. [2018]*

■ 1.1.2   Ray representation

A simple description of light propagation in an optical fibre is based on Snell's law which follows from a high-frequency approximation of the wave equation. The light within its core is guided via total internal reflection honouring Snell's law as shown in Figure 1.2. A simple step-index fibre consists of two dielectric materials (e.g. silica or polymer) with slightly differing indices of refraction, namely the core n_1 and the cladding n_2. A total internal reflection happens at a critical angle (i_c):

$$i_c = \sin^{-1}\left(\frac{n_2}{n_1}\right). \tag{1.1.2}$$

However, for light to be guided, it has to be entering the fibre at a maximum acceptance angle α to satisfy the condition, $i \geq i_c$ as shown in Figure 1.2. Assuming that light is coming from air (i.e. $n_{air} \approx n_0$), Snell's law can be written as

$$n_0 \sin \alpha = n_1 \cos i_c. \tag{1.1.3}$$

The term $n_0 \sin \alpha$ is called the numerical aperture (A_N) of the fibre and is independent of the variation in n_0.

The A_N of a step-index fibre can be expressed as

$$A_N = \sqrt{n_1{}^2 - n_2{}^2}. \tag{1.1.4}$$

We see in expression 1.1.4 that a fibre should have a core with a refractive index n_1 higher than the cladding refractive index n_2. For a single-mode fibre, A_N is commonly in the order of 0.1. Higher A_N values will decrease the losses associated with fibre bending but will increase the propagation losses when it is straight [*Paschott*, 2012]. Therefore, it would be taken into account when purchasing an optical fibre for sensing purposes with shaped fibres as is the case in the work of this thesis. The next section will describe the processes experienced by light as it travels through the optical fibre.
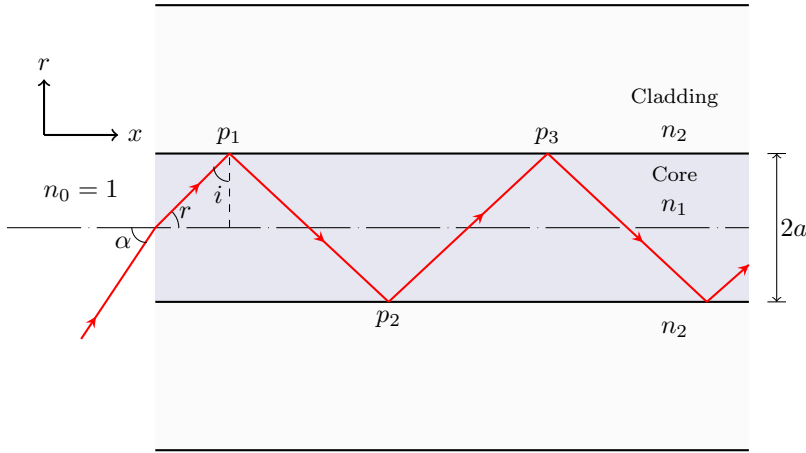
Figure 1.2: *Internal reflection of light in step-index optical fibre.*

1.2   Losses, dispersion and scattering in optical fibres

■ 1.2.1   Losses

As light propagates through the fibre, the decay in field power as a function of distance is described by the total loss or attenuation that is measured in dB/km [*Paschotta*, 2008]. The sources of these losses can be categorised into two main types:

- Intrinsic losses: These fundamental and wavelength-dependent losses are related to the different absorption bands of the fibre material. The sources of these losses, based on *Mitschke* [2010], include a) losses due to the absorption at the ultraviolet band, b) losses due to the absorption at the infrared band, c) Rayleigh scattering that is related to the inhomogeneities within the fibre. At conventional operating wavelength, i.e. $1.55\,\mu$m, Rayleigh scattering dominates and could be considered as the main source of attenuation.

- Extrinsic losses: One source of these losses is related to the undesired presence of fibre impurities like Hydroxyl ion OH^- that causes losses around 1.24 and 1.39 μm [*Paschotta*, 2008]. Another source of losses is the bending of optical fibre that might be in micro and macro scale. These bends might affect the light in-core guidance increasing the power loss to the cladding layer [*Udd and Spillman*, 2011]. This escaping mechanism happens at bends that exceed a specific bending limit called the minimum bend radius. For applications that require bending the fibre, bend-insensitive fibres are commercially available.

■ 1.2.2 Dispersion

The broadening of an optical pulse travelling in a fibre can be defined as dispersion. Despite that, single-mode fibres are less susceptible to dispersion compared to multi-mode fibres that are affected by modal dispersion, even a small degree of dispersion can be undesirable [*Grattan and Meggitt*, 2000]. This phenomenon arises from the wavelength dependency of the time-travel duration of the pulse [*Udd and Spillman*, 2011]. The total dispersion that a pulse experiences in a single-mode fibre can be attributed to three main sources. The main one is the material dispersion caused by the dispersive nature of the refractive index of the fibre's core which is dependent on the light's wavelength (λ). Another source is the waveguide dispersion related to the increasing contribution of cladding for longer light wavelengths as the cladding refractive index is λ-dependent. The last source of dispersion, which is a minor one, is the profile dispersion related to the changes in the refractive index of the core and cladding along the fibre. Dispersion is quite a significant phenomenon to consider, especially for very short optical or fast varying pulses [*Paschotta*, 2008] as shorter pulses are continuously adopted for sensing purposes to increase the spatial resolution.

■ 1.2.3 Scattering mechanism in optical fibres

As light propagates through the fibre, local variations in the refractive index cause a package of photons to scatter. A summary of the different scattering processes is illustrated in Figure 1.3. The scattering mechanisms can be either elastic or inelastic. In this context, elastic means that the energy of the incident photons is preserved, hence the frequency of the scattered photons (ω_{sc}) will have the same frequency as the incident photons (ω_0). Rayleigh scattering is an elastic type and the dominant one that is caused by light encountering inhomogeneities as it propagates in the fibre.

In contrast, inelastic scattering happens when there is an exchange of energy between the incident photons and the medium (i.e. optical fibre glass). It has an anti-Stokes component when scattered photons gain energy and a Stokes component when the photons lose energy to the medium [*Muanenda et al.*, 2019]. This is shown in Figure 1.3 as a positive frequency shift for the anti-Stokes component and a negative shift for the Stokes component

These inelastic processes include Brillouin and Raman processes that happen at the molecular level [*Frings and Walk*, 2011]. The Brillouin scattering is a spontaneous process occurring due to the interaction of the incident light with acoustic vibrations within the optical fibre material happening in the frequency range of 10-30 GHz called acoustic phonons [*Hartog*, 2017; *Paschotta*, 2008]. This process is sensitive to strain as well as temperature and can be stimulated and exploited for sensing [*Niklès et al.*, 1997, 1996].

Raman scattering is caused on the other hand by the vibration in the crystal lattice of the silica material. It shows the effect that the Stokes component is *not* sensitive to the temperature while the anti-Stokes component is sensitive to it (i.e. changes in the amplitude as illustrated in Figure 1.3). This is the basic mechanism

behind the method commonly known as Distributed Temperature Sensing (DTS) [*Hartog et al.*, 1985].
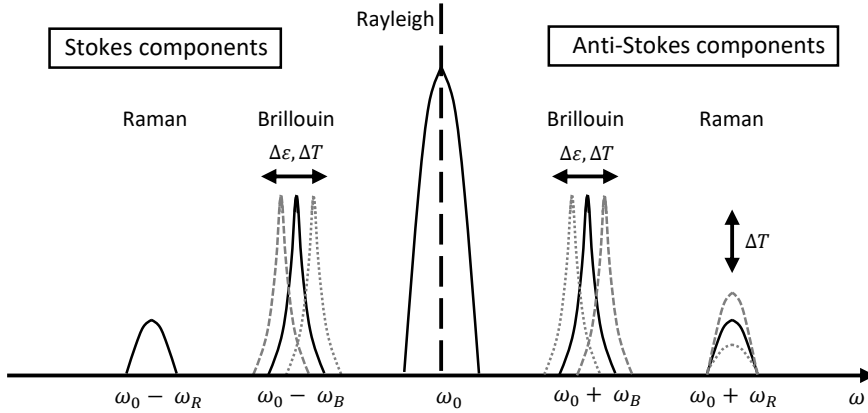
Figure 1.3: *Effect of strain $\Delta\varepsilon$ and temperature ΔT changes on the scattering in optical fibres (modified from Muanenda et al. [2019])*

■ 1.2.4   Optical Time Domain Reflectometer (OTDR)

Through a laser source connected to one end of the fibre, an optical pulse is injected into it, where the light is scattered in all directions by the Rayleigh scattering mechanism as explained previously. After that, the backscattered light, i.e. the reflections propagating towards the OTDR device, is detected by a photodiode [*Mitschke*, 2010]. This instrument is called Optical Time Domain Reflectometer or OTDR. It is the standard technology used for measuring fibre parameters, measuring losses and locating faults in optical fibres used in communication networks or sensing fibres. An idealised OTDR trace for a fibre connected to an OTDR device is shown in Figure 1.4a, where several events are illustrated. The attenuation of the fibre can be measured by the slope of the section from the OTDR trace with the least amount of events. Typical values of attenuation in conventional silica fibres are below 0.2 dB/km for a light source with a wavelength of 1.55 μm [*Grattan and Meggitt*, 2000].

Poor-quality connectors usually result in strong reflections. The strength of the reflection, which is commonly quantified by its reflectance, depends on the type and the condition of the connector; for instance, unclean or broken connectors will cause a high reflectance as well as a high loss. Furthermore, strong reflections are found at the end of the fibre due to the high contrast in the index of refraction between the fibre material and the air. For a given reflection, the reflectance is measured in *dB* as the difference in intensity between the base and peak of the event as shown in Figure 1.4b. Also, a dead zone is expected after a strong reflection; the size of

this dead zone is also a function of the pulse width. Finally, the loss induced by a reflection event can be measured by the difference in intensity as illustrated in Figure 1.4b. On the other hand, bends and fusion splicing (i.e. a jointing process that involves fusing two fibre ends with a high-voltage arc [*Paschotta*, 2008]) does not cause high-intensity reflections —unless it is a bad splice— as shown in Figure 1.4a. Taking an OTDR measurement to check the sensing fibre for breaks, bad splices, and broken connectors is standard practice before acquiring DAS measurements. Also, the total loss needs to be known and below a certain threshold to make sure that enough backscattered light is captured for DAS measurement to work.
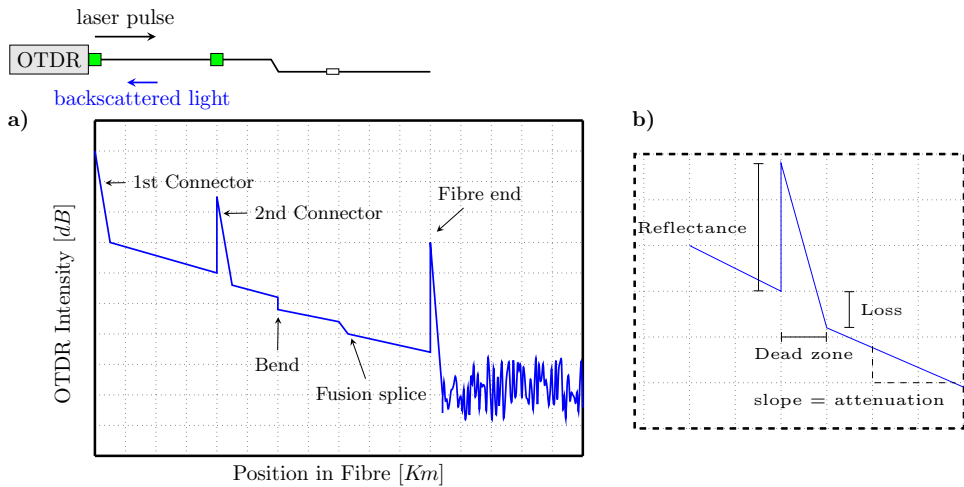
Figure 1.4: *Idealised OTDR Example Trace.*

1.3 DVS/DAS interrogation methods

■ 1.3.1 Basic anatomy of a DVS/DAS system

Strain measurement gauges material deformation relative to its original length, representing a dimensionless ratio that is independent of specific units. A dynamic measurement of strain refers to the variation of this quantity over time. Such measurement can be acquired by a DVS/DAS system consisting of an interrogation unit or an interrogator, an optical fibre and a mechanical disturbance to be recorded. Figure 1.5a contains a depiction of a DAS measurement. The interrogation unit contains an optical source, i.e. a laser, that injects a probe pulse through the transit sensing fibre. As the pulse propagates, it is scattered, by the process of Rayleigh scattering, in all directions by randomly distributed inhomogeneities infused in the fibre material. These tiny scatterers are the impurities added to the fibre as dopants while manufacturing [*Lumens*, 2014]. The backscattered light is collected by a photodetector at the receiver.

To understand how DAS records a passing seismic wave, a very simplistic illustration is presented in Figure 1.5. To properly describe this, two-time scales are considered, namely a fast time τ and a slow time t. The fast time τ corresponds to the transit time of light within the optical fibre, while the slow time t corresponds to the time of the passing seismic wave. For the sake of simplicity, imagine just two scattering points separated by a distance of x in the rest position as shown in Figure 1.5b. As a wave passes in t time, the relative distance between the scattering points is changed by δx and therefore the phase of the back-scatter light is illustrated in Figure 1.5c which results in the measured strain shown in Figure 1.5d.
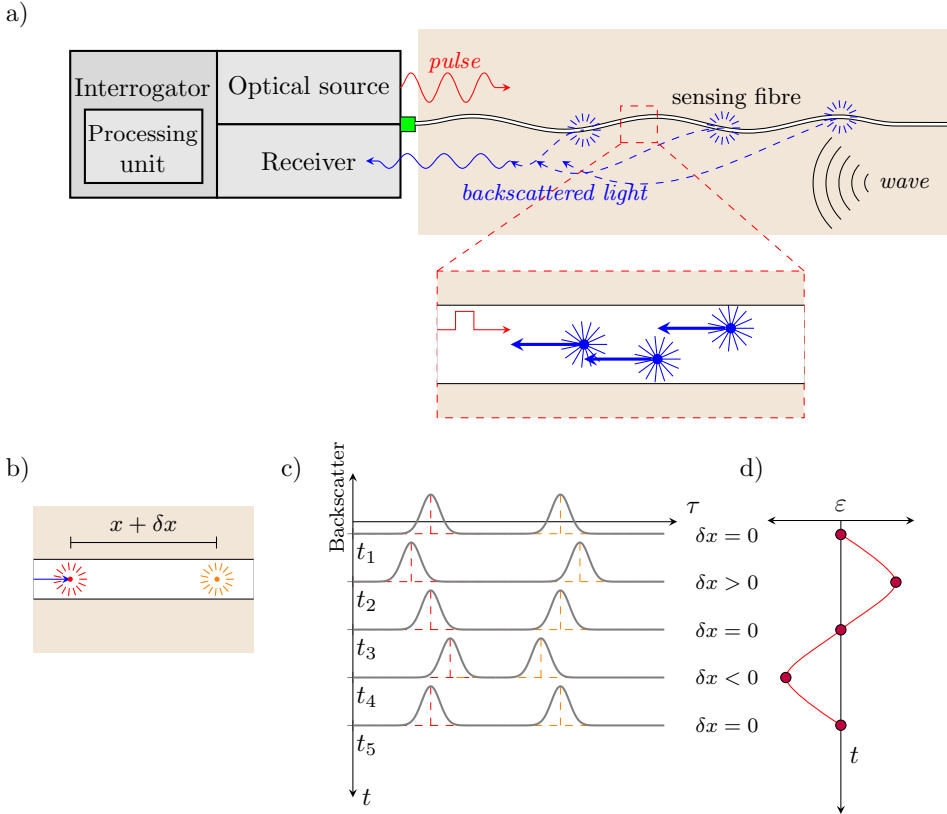
Figure 1.5: *Illustration of DAS principle. a) Main components of a DAS system: an optical source sending a pulse into the fibre, and back-scattered light to be captured and processed. b) Two scattering points separated by distance $x + \delta x$. c) Perturbation of phase of the back-scattered light from the scattering points in (a), to be translated into a strain measurement as in (d).*

■ 1.3.2 What are we measuring with DVS/DAS ?

Unlike geophones (velocity sensors) and hydrophones (pressure sensors) that measure the seismic disturbance at a particular sensing point, fibre measures that seismic disturbance as the strain or strain rate distributed (i.e. averaged) in a defined length that is commonly referred to as the gauge length L_g. The DVS/DAS data is spatially sampled at a particular channel spacing Δr which is determined by the sampling frequency f_s and the two-way group velocity in the fibre v_g with the relationship, $\Delta r = v_g/f_s$ [*Dean et al.*, 2015a]. The gauge length is usually larger than the channel spacing as illustrated in Figure 1.6. It is important to note that the spatial resolution is mainly controlled by the gauge length not the channel spacing; that is, higher spatial resolution can be achieved with shorter gauge length. However, there is a trade-off between the signal quality and L_g; particularly, a very short gauge length will result in a lower signal-to-noise ratio. According to *Dean et al.* [2017], to find the most suitable gauge length with minimal sacrifices, one should consider the frequencies and velocities of the seismic waves to be measured. For example, in case the fibre is deployed vertically in a well, multiple gauge lengths that vary in depth can be used if the interrogator allows it.
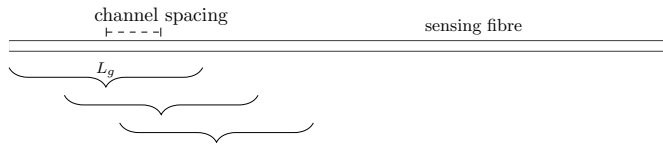
Figure 1.6: *Illustration of L_g and channel spacing.*

There are some similarities between hydrophone and fibre measurements in terms of the polarity of the recording, i.e. same first break polarity as the geophone but reversed polarity in the reflections as shown in Figure 1.7. The measured strain cannot differentiate the direction of the impinging seismic waves as shown experimentally by *Papp et al.* [2017]. To convert the strain response of the fibre to comparable response to geophone velocities responses, the data can be either integrated with respect to time or fibre length as presented by *Correa et al.* [2017].

■ 1.3.3 Measuring dynamic strain with coherent OTDR (C-OTDR)

The basic idea of measuring dynamic strain with fibre is based on optical time domain reflectometry. In contrast to sources used in conventional OTDR, coherent pulses with ultrashort temporal length are used in coherent OTDR (C-OTDR); this is because coherent sources can produce pulses with preserved and consistent phase and amplitude that are only altered when the propagating lights hit a scatterer. In other words, the benefit of using C-OTDR is the ability to correlate an OTDR measurement to a reference measurement [*Lumens*, 2014]. This is especially important for DVS/DAS since the method is based on the relative changes in distance

between the scatterers within the fibre as described in section 1.3.1. Two main schemes with C-OTDR are followed to retrieve the dynamic strain measurements. The first is amplitude-based, where it is based on comparing two consecutive measurements at each fibre location. This scheme was first proposed by *Taylor and Lee* [1991] for intrusion detection and implemented in practice by *Juarez et al.* [2005]. The name phase ϕ-OTDR is sometimes used to describe such a system even though it is mainly based on changes in the intensity, not the phase. According to *Hartog et al.* [2013], the problem with these systems is their non-linearity in the strain response. This source of non-linearity is the unpredictable phase changes happening to the backscattered light. However, recent improvements in ϕ-OTDR systems allowed enhancement in the linearity such as the use of chirped-pulse in HiFi-DAS based on the work of *Pastor-Graells et al.* [2016] with a strain resolution of $1 - 4\mu\varepsilon$ [*Pastor-Graells et al.*, 2017].
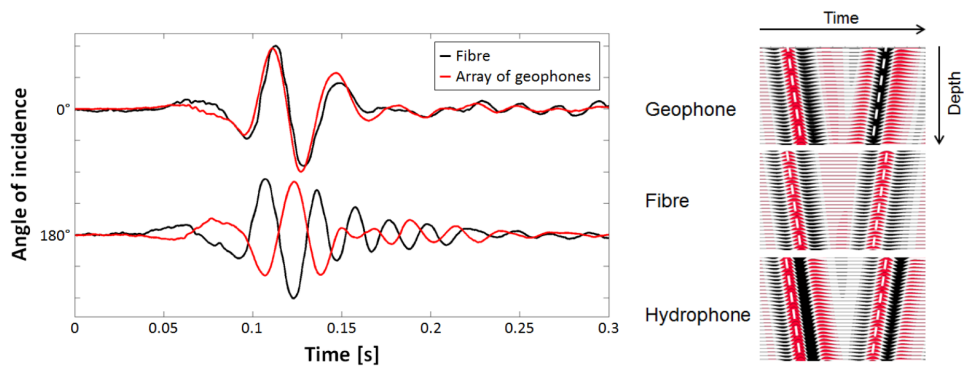
Figure 1.7: *Comparison on the polarity of geophone vs. fibre vs. hydrophone (Dean et al. [2015b]).*

On the other hand, mainstream DVS/DAS systems are based on the phase information in the backscattered signal that is sometimes called differential-phase ($\Delta\phi$)-OTDR where improved linearity is usually found by using the phase information of two different locations of the fibre simultaneously [*Hartog et al.*, 2013]. For the unperturbed length of the fibre, i.e. unchanged path length, the phase of the backscattered light remains constant. However, if the fibre is perturbed by an impinging seismic wave, the phase difference $\Delta\phi$ as a function of path length l is altered. The relationship to derive this phase shift is derived by *Hocker* [1979] as

$$\Delta\phi(l) \;=\; \varepsilon l \left[\beta - \frac{1}{2}\beta n^2 [(1-\nu)p_{12} - \nu p_{11}] \right], \tag{1.3.1}$$

where ε is the strain, β is the propagation constant, n is the refractive index, ν is the fibre's Poisson's ratio, p_{11} and p_{12} are strain-optic coefficients. To retrieve the phase-difference, that is later converted to strain, three main approaches are commonly

used. An issue with these approaches is the fading of the backscattered signal; this occurs due to the destructive summation of the electric-field phases resulting in a very weak backscattered signal [*Hartog et al.*, 2018; *Wang et al.*, 2020]. Next, I discuss the three main methods used for phase retrieval.

Dual-pulse approach

This approach was first proposed by *Dakin and Lamb* [1990]. The basic arrangement of such a system is shown in Figure 1.8a. It works by sending two pulses separated by a duration τ with frequencies f_1 and f_2. An acousto-optic modulator is used to modulate the pulses separated by ΔT. The separation ΔT is proportional to the gauge length L_g such that $\Delta T = L_g/(2\ c\ n)$. The performance and linearity of such systems, among other factors, are determined by L_g as well as τ [*Dean et al.*, 2017; *Hartog et al.*, 2013]. The backscattered light of both signals is mixed back in the detector to create an interference pattern that is linearly related to the strain applied to the fibre [*Masoudi and Newson*, 2017a].

Single-pulse approach

Posey et al. [2000] proposed this approach by using one pulse instead of two to recover the relative phase difference at two locations at the fibre. This interferometric approach involves splitting the backscattered light within a Mach-Zehnder interferometer (MZI) with a certain ΔL to obtain two traces. The gauge length here is determined by the ΔL of the interferometer. To determine the phase relationship, hence the strain information, the resultant signals are recombined. Improved versions of such have been proposed by *Masoudi and Newson* [2017b] and *Farhadiroushan* [2010].

Heterodyne approach

This method was proposed by *Hartog and Kader* [2012], where multiple pulses with a shifted frequency of Δf are used to interrogate the fibre. The main difference between this approach compared to the previous two is that the phase-retrieval process allows setting the gauge length after acquiring the data, unlike other approaches.

■ 1.3.4   Advances in DAS technology

The two main areas where DAS is continuously improving are the enhancement of the recorded signal, which is done by lowering the noise floor as much as possible and increasing the length range for the measurements. These two are tackled in two components of the DAS system including the sensing fibre and the interrogator unit. I describe next the major two areas of development that are relevant to geophysical applications.
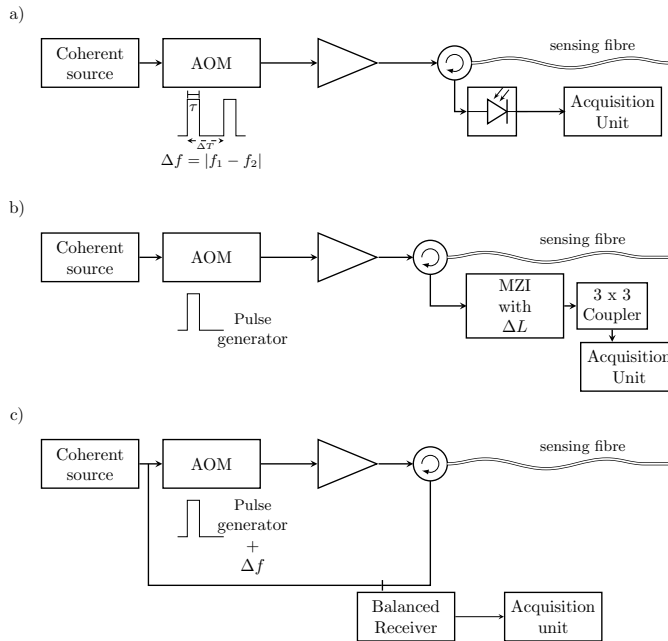
Figure 1.8: *System set-up of common DVS/DAS interrogation approaches adapted from Masoudi and Newson [2017a]: a) Dual-pulse, B) Single-pulse and C) Heterodyne. AOM in the figure stands for acoustic-optic modulator.*

Engineered fibres

Part of the recorded DAS signal is the noise that is related to the interrogation process and the differential phase retrieval. To enhance the DAS signal, optical fibres are adapted to increase the amount of overall backscattered energy. This can be directly done by increasing the amount of dopants in the optical fibre while manufacturing. However, such an approach will come at the cost of increasing the overall attenuation and therefore decreasing the range of the measurement substantially. Recent advances to enhance the backscattered light includes engineering the fibre so it has increased scatter centres at regular intervals. Adaption of such an approach could yield as much as 20 dB gain in the dynamic range as described by *Shatalin et al.* [2021]. This could be by the use of ultra-weak fibre Bragg grating fused in the sensing fibre [*Shan et al.*, 2019; *Zhang et al.*, 2019; *Li et al.*, 2020]. This, however, will increase the cost of the fibre which is a major disadvantage, particularly as one of the main attractions of adopting DAS is that standard optical fibres can be used.

Long-range measurements

Increasing the length range of DAS measurement has been of interest to large-scale applications of earthquake monitoring and subsurface characterisation onshore and

offshore settings [*Ajo-Franklin et al.*, 2019a; *Lindsey et al.*, 2019; *Nayak et al.*, 2021a; *Cheng et al.*, 2023]. In those applications, dark fibres are commonly used, which are unused optical fibres in the telecommunication infrastructure. Longer ranges can be obtained through the use of wider laser pulses but this will come at the cost of decreased spatial resolution. Another way to increase the range is by the use of optical amplifiers along the sensing fibre [*Parker et al.*, 2014]. However, this poses engineering and logistical challenges; including the increased system complexity of such implementations as well as possible limitations related to the access to certain areas along the fibre. Recent advances in the interrogation process to increase the range include using chirped signals as a light source instead of pulses [*Pastor-Graells et al.*, 2017; *Fernández-Ruiz et al.*, 2019; *Waagaard et al.*, 2021]. This will allow illuminating longer lengths of fibre with limited compromise in the spatial resolution. For instance, a whopping range of 171 km is achieved with a dynamic range of 57 dB using such an approach [*Waagaard et al.*, 2021].

1.4   Applications of DAS in geophysics

Implementation of DAS technology for geophysical applications was investigated in 2010 with the field trials of Vertical Seismic Profiling (VSP) conducted by a system developed by Shell and OptaSense. *Mestayer et al.* [2011] showed the acquired seismic data collected in CO_2 storage facility in Alberta, Canada, where comparable results were found by DAS compared to conventional geophones in terms of clear direct and reflected arrivals. Another trial acquired at another Shell asset in the USA showed comparable results with minor deviations in the velocity profiles [*Mestayer et al.*, 2011]. In both trials, the noise floor for the DAS data is higher than conventional geophones. Another DAS system, called iDAS, developed by the company Sillixa, has shown significant improvement in the signal-to-noise between its first and second generation in VSP surveys [*Correa et al.*, 2017; *Daley et al.*, 2013]. Furthermore, Schlumberger has developed a DAS system and was incorporated in a wireline cable based on the system of *Hartog and Kader* [2012] called hDVS. VSP measurement from this system is presented in *Frignet and Hartog* [2014].

The oil and gas industry is one of the main industries that assisted in popularising the use of DAS. Due to the potential of permanent fibre installations in wells, DAS was used for time-lapse VSP with acceptable repeatability as illustrated by *Cheraghi et al.* [2018] and *Mateeva et al.* [2017]. Also, for measuring seismic parameters like attenuation, which is an essential parameter for amplitude-related analyses such as acoustic and elastic inversions as well as Amplitude-versus-Offset analysis (AVO) [*Pirogova et al.*, 2019]. Another application of DAS is fracture characterisation based on the velocity variation as in *James et al.* [2017]. It can be also used for monitoring hydraulic fracturing processes [*Jin and Roy*, 2017; *Grandi Karam et al.*, 2013]. For crustal studies, the technology has been adapted for fault localisation and delineation by *Jousset et al.* [2018]. A recent special section on DAS including a wide range of applications was recently published [*Jin et al.*, 2023].

1.5 On the issue of broadside sensitivity

The implementations of DVS/DAS in land seismic have been very limited but it is continuously gaining popularity. One of the few examples of such implementation is the near-surface velocity estimation with Multichannel Analysis of Surface Waves (MASW) with passive and active sources presented in *Cole et al.* [2018]. For conventional land seismic, including refraction and reflection surveys, fewer examples have been presented so far. This is attributed to the decreased broadside sensitivity of fibre as a function of $\cos^2(\theta)$, compared to geophones whose amplitude response has a function of $\cos(\theta)$, where θ is the angle of incidence [*Mateeva et al.*, 2014]. An indirect approach to obtaining seismic data with DAS was implemented by *Bakulin et al.* [2017]; their approach involved obtaining reflection data by using multiple shallow upholes.

A more direct way to resolve the broadside sensitivity issue is through fibre shaping. One of the few attempts of using DAS in land seismic, by enhancing its broadside sensitivity, is a field trial implemented by *Hornman* [2017] using helically wound fibre-optic cable (HWC) that is deployed in shallow a horizontal borehole, where he compared his measurements to a streamer containing hydrophones. Despite the difference of 14 *dB* in signal-to-noise found between HWC and hydrophone measurements in favour of the latter, the dense spatial resolution of DAS measurements allowed satisfactory seismic recording with comparable clear events. The enhancement in broadside sensitivity comes from shaping the fibre in a particular orientation that was modelled by *Kuvshinov* [2016]. Similar fibre geometry is used by *Urosevic et al.* [2018], where superior detailed data, i.e. including reflections with fewer surface waves, were observed using the shaped fibre compared to a straight fibre. Fibre shaping to helix has been adopted and extended to theoretically estimate the full strain tensor by *Ning and Sava* [2018a] and *Innanen and Eaid* [2018]. *Ning and Sava* [2018a] used the former approach including deriving the full strain tensor based on using multiple helices wrapped with different pitch angles, whereas *Innanen and Eaid* [2018] modelled the response of 2-helix configuration (a helix inside a helically shaped fibre). Furthermore, to measure multi-component data, several approaches were implemented, which include a field deployment of a large shaped fibre configuration that was presented in *Innanen et al.* [2019] and used to estimate strain-rate components [*Hall et al.*, 2021]. Another attempt uses optical fibres wrapped around a polyvinyl chloride frame in three directions to provide 3-component data at a specific point of deployment [*Takekawa et al.*, 2022].

1.6 Research questions and outline

DAS, as described earlier, is significantly more sensitive in the axial direction of the sensing fibre. Due to this very nature, obtaining seismic multi-component information is not trivial. This thesis tries to answer whether multi-component information can be obtained via the use of fibre shaping into several shapes including straight, sinusoidally shaped and helically wound fibres. Several questions are tackled to achieve that. As a first step, in chapters 2 and 3, I look at the question of whether a

directional strain sensor could be achieved using the concept of a sinusoidally shaped fibre embedded in a homogeneous material (i.e. chapter 2). Based on the results obtained there, I try increasing this directional sensitivity via the use of low-Poisson's ratio metamaterial.

Since the results were not very promising, I went to further investigate a more common approach of using the helically wound fibres *in combination with straight fibres* to see whether multi-component information could be obtained using such a configuration. Surface-deployed DAS was acquired to address this using active-source seismic in chapter 4. I also see during these field experiments, that the effects of fibre geometry and gauge lengths play an essential role in the measured DAS response. So these effects are considered and investigated in chapter 5.

The following outline contains brief descriptions of the main chapters:

- Chapter 2: *Directional strain sensitivity of sinusoidally shaped optical fibre embedded in polyurethane strip*:
  In this chapter, I examine the directional strain sensitivity of a sinusoidally shaped fibre using BOFDA (Brillouin Optical Frequency Domain Analysis). The sinusoidal fibre is embedded within a polyurethane-type material that is called Conathane®. I look at its static strain response from a theoretical and experimental point of view. I examine its response to loading in three directions. I also present an analytical model as well as a numerical model to compare it to the experimental measurements.

- Chapter 3: *On zero-Poisson-ratio structures for directional strain sensing: concept, experimental results and numerical modelling*

  In this chapter, I examine a novel concept of adapting a zero-Poisson's ratio metamaterial as the embedding material to enhance the sinusoidal fibre strain sensitivity. I use several 3D printing technologies to come up with a prototype and examine its directional sensitivity with laboratory and numerical experiments.

- Chapter 4: *Experiences with Distributed Acoustic Sensing using both straight and helically wound fibres in surface-deployed cables - a case history in Groningen, The Netherlands*

  In this chapter, I present a case history of acquiring DAS measurements using a combination of straight and helically wound fibres. I examine the differences and similarities between the different fibre configurations. This includes several observations in the phase and amplitude differences for the surface waves and the reflections. I also present analytical and numerical models to explain these differences.

- Chapter 5:*Effects of gauge length and fibre geometry on active- and passive-source DAS data*

  In this chapter, I specifically look at the effect of gauge length along the fibre configuration on the retrieval of surface waves including active and passive methods.

2

Directional strain sensitivity of sinusoidally shaped optical fibre embedded in polyurethane strip

Abstract Distributed strain sensing using a straight optical-fibre cable suffers from a decreased strain sensitivity away from the fibre's axis. In this study, the directional sensitivity of a fibre optic cable is enhanced via sinusoidally shaping the fibre that is embedded in a polyurethane strip. First, the directional sensitivity is quantified via an analytical model, validated with a numerical model. Second, static-strain measurements using a Brillouin Optical Frequency Domain Analysis (BOFDA) system are carried out on a physical sample of such a strip. Three different loading directions are examined, namely in-line, broadside and along-strip orientations. The first means deforming the transversal in-plane of the sinusoidal fibre, the second means deforming the plane normal to it, and the third means deforming along the strip's longest dimension. Comparing the in-line and broadside loading theoretical models and experimental results, it can be observed that the response to the compressive stress in these orientations is opposite, i.e. the fibre experiences negative strain, so shortening, for an in-line deformation, and a positive strain, so stretching, for a broadside deformation. It is found that the fibre is slightly more sensitive in the in-line direction which agrees with the behaviour as predicted by the models. For the along-strip loading, in our case extension, negative strain is predicted theoretically and measured experimentally. Also, we see that the measured strain along the optical fibre is mainly influenced by the elastic properties of the embedding material due to, most importantly, the Poisson's ratio as well as the geometrical parameters of the sinusoidally shaped fibre.

2.1   Introduction

Distributed fibre optical sensing is an emerging technology in the field of static and dynamic strain sensing. This technology has been utilised in a wide range of applications including for monitoring the integrity of structures as well as for monitoring the strain and temperature for various settings. Distributed Strain Sensing (DSS) is an umbrella term used to describe a number of technologies to measure static and dynamic strains. Distributed Acoustic Sensing (DAS) or Distributed Vibration Sensing (DVS) are commonly used terms that refer to technologies that are developed to retrieve dynamic-strain measurements [*Reinsch et al.*, 2021]. In seismology, DAS/DVS has been adapted for passive and active seismic measurements. Early adoptions were implemented for borehole monitoring through several Vertical Seismic Profiling (VSP) trials [*Mestayer et al.*, 2011; *Daley et al.*, 2013; *Frignet and Hartog*, 2014; *Mateeva et al.*, 2014]. Even though the signal quality retrieved from DAS measurements still, for the most part, lags behind the quality of geophone measurements, DAS provides the opportunity to have denser spatial sampling at a lower cost.

Several implementations of DAS for surface seismic have been executed that include passive and active measurements. On a larger scale, DAS has been used for earthquake observations by *Lindsey et al.* [2017] and for imaging geological structures by *Jousset et al.* [2018]. For near-surface velocity estimation, Multichannel Analysis of Surface Waves (MASW) with passive and active sources is carried out with DAS, as presented in *Cole et al.* [2018] as well as for site characterisation by *Spica et al.* [2020]. DAS also has been used to retrieve the reflection response at the surface using multiple shallow upholes [*Bakulin et al.*, 2017]. Using DAS via sensing with a straight fibre showed a directional sensitivity limitation as discussed in *Mateeva et al.* [2014]. This limitation manifests as a decreased sensitivity to broadside waves, i.e. waves perpendicular to the fibre. Helically wound fibres were introduced in *Den Boer et al.* [2012] to enhance the broadside sensitivity. The theoretical responses of the helically wound fibre is discussed in *Kuvshinov* [2016]. Attempts of implementing the helically wound fibres were presented in *Hornman* [2017] and *Urosevic et al.* [2018]. The idea of shaping a fibre into a helix has been extended to so-called nested helices in theoretical studies, with the aim to estimate the full strain tensor, in *Ning and Sava* [2018a] and *Innanen and Eaid* [2018].

Although the fibre can be shaped to one's wishes, an implicit assumption in the latter two theoretical approaches is that the fibre needs to be embedded in a material in order to be manufactured as a cable. So the embedding material needs to be part of the model and the embedding material will affect the behaviour of the fibre. Here we address this issue.

In our study, we adapted the sinusoidally shaped fibre concept by embedding it within a strip of polyurethane, in our case made of a type called Conathane®. We first provide an analytical description of the strain experienced by the embedded fibre and a numerical model to validate it. This is followed by a discussion of experiments conducted with a Brillouin Optical Frequency Domain Analysis (BOFDA) system examining the difference in sensitivity between the different sides of the

strip to strain. Finally, we aim to model the results and match them with the observed data, to see whether the behaviour of the fibre embedded in the strip is well described by the models.

2.2 Deforming a sinusoidally shaped fibre with a static load

An analytical model is derived for the strain experienced by a sinusoidally shaped fibre. Consider a sinusoid with a length denoted by l_0, embedded in a strip. A cross-section through the plane $y = 0$, in which the sinusoidal fibre is located, is shown in Figure 2.1a. In this model the parameters A and Λ are introduced that denote the amplitude and the length of one sinusoid, respectively. The position of the fibre can be expressed by

$$
\mathbf{f_0} = \begin{bmatrix} x \\ 0 \\ A\sin(2\pi\frac{x}{\Lambda}) \end{bmatrix}. \tag{2.2.1}
$$

Since we assume a 2D model, in which embedding material is homogenous, the deformation of the sinusoid in $y-$direction is zero and therefore we omit the vector notation in this analytical model. Consequently, the sinusoid can be expressed as $f_0(x) = A sin(2\pi\frac{x}{\Lambda})$. The general form of the arc length of a function $f(x)$ is expressed as

$$
l = \int_a^b \sqrt{1 + \left(\frac{df}{dx}\right)^2} \ dx. \tag{2.2.2}
$$

So for the function f_0, the arc length can be expressed as

$$
l_0 = \int_0^\Lambda \sqrt{1 + 4\pi^2\frac{A^2}{\Lambda^2}\cos^2\left(2\pi\frac{x}{\Lambda}\right)} \ dx. \tag{2.2.3}
$$

Three scenarios of deformation are considered here. The first one, which we call in-line deformation ε_{zz}, is due to a plane stress σ_{zz} acting in the z-direction, as indicated in Figure 2.1b. The second one is a broadside deformation ε_{yy}, where a plane stress σ_{yy} is applied in the y-direction, as indicated in Figure 2.1c. The third scenario is the along-strip case stretched in the x-direction.

■ 2.2.1 In-line deformation

Deforming the strip with a compressive stress σ_{zz} will result in a change in the shape of the embedded sinusoid (see Figure 2.1b). We assume that the stresses applied are low and within the linear elastic regime. Therefore, its relationship to the strain in the same direction, ε_{zz}, is

$$
\sigma_{zz} = E_c \, \varepsilon_{zz}, \tag{2.2.4}
$$

where E_c is Young's modulus of the embedding cable. We assume that the displacement change of the fibre in z-direction is proportional to ε_{zz} of the cable material, and in the x-direction by $\varepsilon_{xx} = -\nu_c\,\varepsilon_{zz}$, where ν_c is Poisson's ratio of the cable material. This deformation will cause A to decrease due to the negative ε_{zz} and Λ to increase. Following the assumption of plane strain and that the fibre is placed in the y_0-plane, the out-of-plane strain ε_{yy} is assumed to be zero. This will result in a change in the fibre shape as

$$f_d = (1 + \varepsilon_{zz})\, A \sin\left(2\pi \frac{x}{\Lambda(1 - \nu_c\varepsilon_{zz})}\right). \tag{2.2.5}$$

Therefore, the length of the deformed fibre is found by the following equation:

$$l_d = \int_0^{\Lambda(1-\nu_c\varepsilon_{zz})} \sqrt{1 + 4\pi^2 \frac{A^2(1 + \varepsilon_{zz})^2}{\Lambda^2(1 - \nu_c\varepsilon_{zz})^2} \cos^2\left(2\pi \frac{x}{\Lambda(1 - \nu_c\varepsilon_{zz})}\right)}\; dx. \tag{2.2.6}$$

■ 2.2.2 Broadside deformation

In this case, a plane stress of σ_{yy} is applied to the strip causing the deformation of the sinusoid in the x- and z-directions as shown in Figure 2.1c. For a compressive stress, the sample will be shortened in the y-direction, so $\varepsilon_{yy} < 0$, but will be lengthened in the other directions, due to Poisson's ratio of the material. This will result in a deformed fibre shape f_d, expressed as

$$f_d = (1 - \nu_c\varepsilon_{yy})\, A \sin\left(2\pi \frac{x}{\Lambda(1 - \nu_c\varepsilon_{yy})}\right). \tag{2.2.7}$$

Thus, the length of the deformed fibre due to a broadside load is found as

$$l_d = \int_0^{\Lambda(1-\nu_c\varepsilon_{yy})} \sqrt{1 + 4\pi^2 \frac{A^2}{\Lambda^2} \cos^2\left(2\pi \frac{x}{\Lambda(1 - \nu_c\varepsilon_{yy})}\right)}\; dx. \tag{2.2.8}$$

The arc length in equation 2.2.8 can be simplified by the substitution $x' = x/(1 - \nu_c\varepsilon_{yy})$, leading to:

$$l_d = (1 - \nu_c\varepsilon_{yy})\, l_0. \tag{2.2.9}$$

Since ε_{yy} is negative for compressive stress, an elongation in the x- and z-direction is expected. It is clear from equation 2.2.9 that the deformed length is independent of the geometrical parameters of the sinusoid and solely dependent on the mechanical properties of the material.

■ 2.2.3   Along-strip deformation

For this case, we consider a plane stress in the x-direction. For a tensile stress in the x-direction, i.e. $\varepsilon_{xx} > 0$ and the out-of-plane strain ε_{yy} is assumed to be zero. This will cause Λ to extend, whereas A will be shortened due to the Poisson's ratio of the material. This is expressed by

$$f_d = (1 - \nu_c \varepsilon_{xx}) \, A \sin \left(2\pi \frac{x}{\Lambda(1 + \varepsilon_{xx})} \right). \tag{2.2.10}$$

Therefore, the arc length of the deformed state is found by

$$l_d = \int_0^{\Lambda(1+\varepsilon_{xx})} \sqrt{1 + 4\pi^2 \frac{A^2(1 - \nu_c \varepsilon_{xx})^2}{\Lambda^2(1 + \varepsilon_{xx})^2} \cos^2 \left(2\pi \frac{x}{\Lambda(1 + \varepsilon_{xx})} \right)} \, dx. \tag{2.2.11}$$

Note that expressions 2.2.3, 2.2.6 and 2.2.11 are elliptical integrals of the second kind and are evaluated numerically.
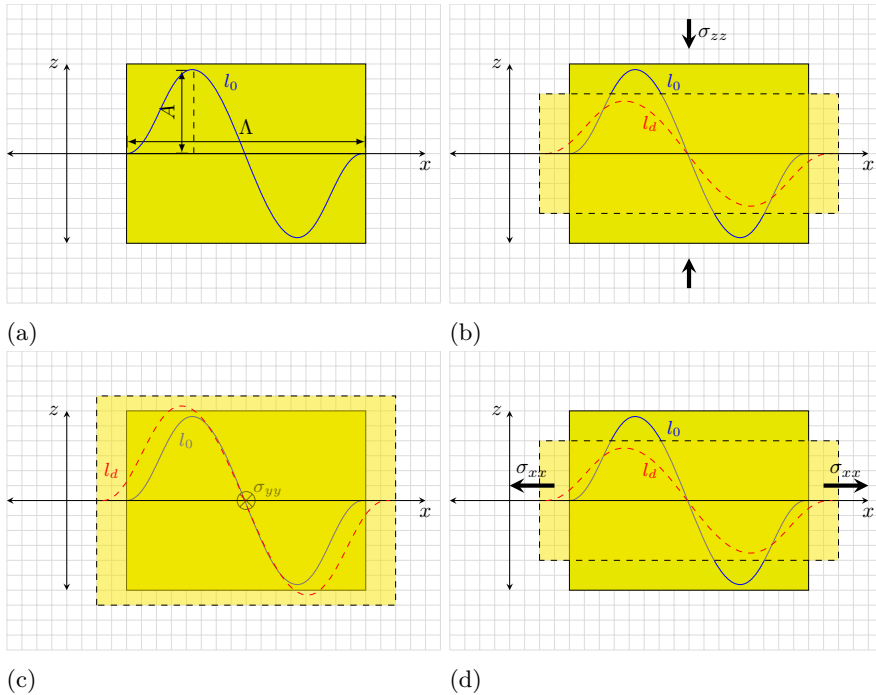

Figure 2.1: *Deformation of sinusoid embedded in a strip (a) before deformation, and after (b) in-line deformation and (c) broadside deformation and (d) along-strip deformation.*

■ 2.2.4   Validating analytical model with numerical model (3D)

A numerical model was developed, with the aim of validating the analytical model. Using COMSOL® Solid Mechanics module, a 3D model is constructed for the three loading cases previously described. Details of the numerical model are described in appendix A.

■ 2.2.5   Fibre strains and sensitivities

The strain of the traced fibre, i.e. ε_c, assumes that the fibre is perfectly following the embedding material. It can be described by the following expression:

$$\varepsilon_c = \left(\frac{l_d(\varepsilon_{xx}, \varepsilon_{yy}, \varepsilon_{zz})}{l_0} - 1 \right). \tag{2.2.12}$$

To quantify the difference in sensitivity of the three loading scenarios that are described previously, we evaluate ε_c normalised by the applied strain ε_{ii}, i.e. $\varepsilon_c/\varepsilon_{ii}$, versus the ratio of the geometrical parameters (e.g. A ranging from 1 to 12 cm and fixed Λ of 6 cm), A/Λ for Poisson's ratios (ν_c) of 0.1, 0.3 and 0.45 that is shown in Figure 2.2. Note that here we use the terms *normalised strain* and *sensitivity* interchangeably. We see that for both in-line and along-strip cases, the normalised strain is dependent on the ratio of A/Λ, unlike the broadside case which corresponds to the Poisson's ratio of the cable material. Also, we see that for the in-line case, the Poisson's ratio matters more at lower values of A/Λ. The normalised strain approaches the true applied strain (i.e. $\varepsilon_c/\varepsilon_{ii} \to -1$) as A increases. On the other hand, the effect of the geometrical parameters is more pronounced in the along-strip case, i.e. the strain is positive at lower A/Λ values and gets negative at higher A/Λ values.

As for our sample with embedded fibre $A = 2.4$ cm and $\Lambda = 6$ cm, and Poisson's ratio of $\nu_c = 0.45$, the In-line sensitivity $\varepsilon_c/\varepsilon_{zz} = 0.575$, that is higher than the broadside sensitivity of $\varepsilon_c/\varepsilon_{ii} = 0.45 = \nu_c$. As for the along-strip case, the sensitivity is predicted to be -0.025. For convenience, we will refer to the in-line sensitivity as S_{IL} and the along-strip sensitivity as S_{AS}.

■ 2.2.6   Fibre shaping and strain transfer

When fibre is coupled to an embedding material, there are some intermediate materials (coating layers) in between that absorb a portion of the strain, so only a partial amount of the strain is sensed by the embedded fibre [*Bastianini et al.*, 2019]. This is due to the difference in the mechanical properties between the host material, fibre coating and the optical fibre itself. Several studies looked at this strain transfer in embedded optical fibre sensors [*Pak*, 1992; *Yuan and Zhou*, 1998; *Li*, 2006; *Reinsch et al.*, 2017]. Strain transfer could also be affected by voids between the fibre and the embedding material caused as mentioned by *Claus et al.* [1989]. The aforementioned studies assume the longitudinal strain transfer between the embedding material and the fibre, where the angle between the fibre and principle stress direction in the embedding material (α) is zero. *Sun et al.* [2016] included the effect

of angle and thermal variation as well. In our study, we only consider the effect of angle variation since we have a sinusoidally shaped fibre with a varying angle (α) while neglecting the thermal variation. From *Sun et al.* [2016], the relationship between the actual measured strain ε_f in the sensing fibre unit and the strain ε_c in the deforming Conathane® material is

$$\xi(\alpha, x) = \frac{\varepsilon_f(x)}{\varepsilon_c(x)} = \cos^2 \alpha \left(1 - \frac{\cosh(\eta x)}{\cosh(\eta L)} \right). \tag{2.2.13}$$

where L corresponds to the length of the sensing unit (analogous to the spatial resolution), and η is the so-called shear-lag parameter. We can see that equation 2.2.13 can be described by two effects; the first is the dependency on the angle α, and the second is related to the mechanical and geometrical properties of the different layer as described by η. For our case, the 4-layer model consists of the fibre cladding, inner coating, outer coating and the embedding material of Conathane®. Then, the shear-lag parameter [*Li et al.*, 2009] can be calculated using by

$$\eta = \left[\frac{1}{2} \, r_f^2 \, E_f \left\{ \frac{1}{G_1} \ln \left(\frac{r_1}{r_f} \right) + \frac{1}{G_2} \ln \left(\frac{r_2}{r_1} \right) + \frac{1}{G_C} \left[\frac{r_C^2}{r_C^2 - r_2^2} \ln \left(\frac{r_C^2}{r_2^2} \right) - 0.5 \right] \right\} \right]^{-\frac{1}{2}}, \tag{2.2.14}$$

where r denotes the radius and G the shear modulus; the subscripts f, 1, 2 and C indicate the type of material, i.e., the fibre, inner coating, outer coating and Conathane®, respectively. The radius of the embedding material (r_C) is assumed to be much larger than the embedded fibre. This is because the thickness of the strip is much larger than the radius of the fibre.

The mechanical properties and the geometrical parameters are contained in Table 2.1. This shear lag parameter η here is based on *Li et al.* [2009] as cited in *Bastianini et al.* [2019]. We calculate the strain-transfer factor ξ for different angles. Figure 2.3 shows that the strain-transfer factor is highly dependent on the angle. The strain-transfer factor is close to 1 when the angle is small, and it gets smaller for higher angles. This is relevant to our sinusoidally shaped fibre that has variable angles. For our sinusoidally shaped fibre with $A = 2.4$ cm and $\Lambda = 6$ cm, the sinusoid will have an average angle of $52°$, which results in an average $\xi = \varepsilon_f / \varepsilon_c = 0.64$.
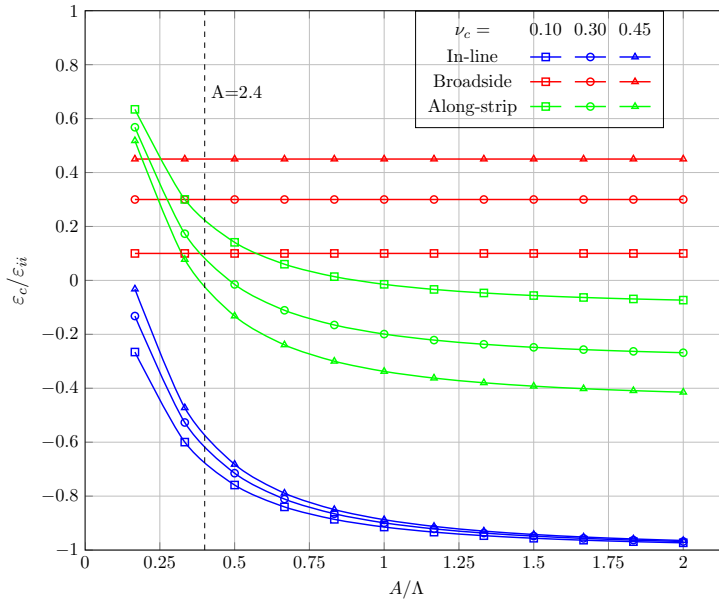
Figure 2.2: *Normalised fibre strain $\varepsilon_c/\varepsilon_{ii}$ vs. A/Λ (A ranges from 1 to 12 cm and $\Lambda = 6$ cm) for all loading scenarios for Poisson's ratios of 0.1, 0.3 and 0.45. The dashed line corresponds to $A = 2.4$ cm, where the inline sensitivity of 0.575, broadside sensitivity $\nu_c = 0.45$ and along-strip sensitivity of –0.025 for $\nu_c = 0.45$.*

Figure 2.3: *Strain transfer factor ξ ($=\varepsilon_f/\varepsilon_c$) for different fibre angles along a fibre length of 0.2 m. Note that this model assumes two fixed ends, which is not the case for our embedded sinusoid. The important thing here is to highlight the effect of the angle.*

Table 2.1: *Geometrical and mechanical properties of Conathane® and of optical fibre (at room temperature).*

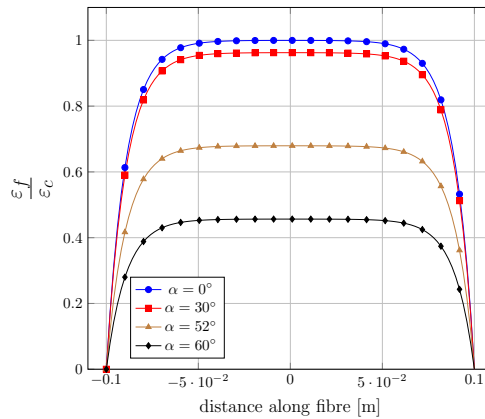| Layer	Outer radius [μm]	E-modulus [GPa]	Possion's ratio ν
Fibre clad (f)	40[†]	72[a]	0.17[a]
Inner coating (1)	150[*]	0.002[b]	0.49[*]
Outer coating (2)	200[†]	1[b]	0.49[*]
Conathane (c)	2000[**]	0.017 ± 0.005	0.45-0.48

[†] provided by the fibre manufacturer (FiberCore).
[a] *Giallorenzi et al.* [1982].
[b] *Michel et al.* [2015]. Values chosen within the range of values cited.
[*] Exact values are unknown, therefore here assumed.
[**] assumed to be 10 times the outer coating radius.

2.3　Static strain experiment with Brillouin Optical Frequency Domain Analysis (BOFDA)

■ 2.3.1　Principle of stimulated Brillouin scattering

Stimulated BOFDA makes use of the scattering caused by the interaction of incident light with vibrations in the molecules of the optical fibre. These vibrations are the result of an excited collection of molecules called acoustic phonons. This interaction is called Brillouin scattering and occurs in the 10-30 GHz range [*Hartog*, 2017]. This scattering process is not elastic because the energy of the incidence photon, and in turn its frequency, is altered (see Figure 1.3).

In our experiment, we used a system based on this principle, made by the company fibrisTerre, the type fTB 2505. It requires both ends of the fibre to be connected to the instrument, where a pump wave and a probe wave are injected simultaneously, by means of a sweep of frequencies. A fibre will resonate at a beat frequency in response to these waves. That beat frequency will result in propagating fluctuations of density. The interaction between the waves and this fluctuation will cause a frequency shift in the pump wave, called Brillouin frequency-shift f_B. This is what is measured by the instrument. Further details of the method can be found in *Nöther* [2010].

Stretching or lengthening the fibre will increase f_B, whereas shortening the fibre will decrease f_B relative to a reference measurement. The strain experienced by the fibre can be evaluated using the following expression, as given in the fTB2502 manual:

$$\varepsilon_f = \frac{\Delta f_B}{C_\varepsilon} = \frac{f_{B,m} - f_{B,r}}{C_\varepsilon} \tag{2.3.1}$$

where

ε_f fibre strain in $\mu\varepsilon$,

$f_{B,m}$ measured Brillouin frequency shift in MHz,

$f_{B,r}$ reference Brillouin frequency shift in MHz,

C_ε strain coefficient of fibre in MHz/$\mu\varepsilon$.

C_ε varies typically between 40 to 50 MHz/1000$\mu\varepsilon$ for different types of fibre, according to the fTB2502 manual. A value of 61 MHz/1000$\mu\varepsilon$ is also reported by *Nöther* [2010].

■ 2.3.2   The sample

In order to verify whether the model describes/explains the behaviour of a real sample, the company De Regt produced a sinusoidally shaped fibre embedded in a Conathane® strip. The fibre is bend-insensitive with core/cladding diameter of 6.2/80 μm and a dual-acrylate coating of 200 μm. The elastic properties of our optical fibre were not measured, typical values are contained in Table 2.1. The table shows the significant difference in elastic properties of fibre compared to the mechanical properties of Conathane®. The sample is 200 cm long, 6 cm wide and its thickness varies between 1.6 to 1.8 cm. This thickness variation could be attributed to the manual production process. The length of the fibre embedded within the Conathane® strip is about 4 m long with extra fibre at both ends for the terminations.

Since the material properties of Conathane® are not well known, a separate small experiment was performed on a cylindrical sample, that has a length of 85.0 mm and a radius of 19.5 mm, to determine Young's modulus E_c and Poisson's ratio ν_c. The strains to that cylindrical sample were of the order of 10 mε's. These are much higher than the strains applied to the sample with the sinusoidally shaped fibre which were in the order of 0.1 mε. The values obtained from this small experiment are included in Table 2.1. The Young's modulus and Poisson's ratio of Conathane® are measured through a uniaxial compressional test using MTS 815 system at a strain of 1%. Note that this system is made for rock mechanics applications, hence it is designed for much higher strain values and much stiffer materials. Assuming that the load is within the linear and elastic regime, measurements are applicable with some uncertainty.

■ 2.3.3   Set-up of experiment

A sketch of the set-up of the measurement is shown in Figure 2.4. Each of the fibres of the cable sample was coupled to a patch cord, which was fusion-spliced to a pigtail that connected to the BOFDA device. Photographs of the set-up are given in Figure 2.5.

To optimise the acquisition process, an initial measurement was taken to choose the frequency range of interest. The main parameters to optimise are the Brillouin Frequency Shift scan range and step as well as spatial resolution; a scan range of 10 to 11 GHz was chosen, with a step of 0.1 MHz (i.e. this is equivalent to steps of 2$\mu\varepsilon$ for $C_\varepsilon = 0.050$ MHz/$\mu\varepsilon$) for every 0.2 m, respectively. Figure 2.6 shows the reference f_B spectrum, annotated with the main sections of the fibre. Based on

this, the Brillouin-frequency scan range was limited to 10.2–10.4 GHz to reduce the frequency-sweeping time for the high-resolution measurement of 0.1 MHz to only include the fibre in the sample.
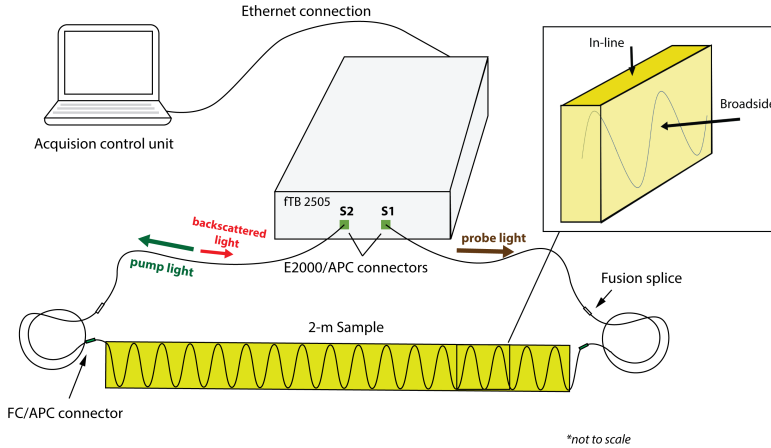

Figure 2.4: *Set-up of static strain experiment with BOFDA. Note that the loads were applied in in-line and broadside orientations as illustrated.*

■ 2.3.4   Observed frequency shift due to in-line (z), broadside (y) and along-strip (x) loads

To investigate the directional sensitivity of our sample, a range of loads was applied to the sample in in-line, broadside and along-strip orientations as illustrated in Figure 2.1. For the first two cases, the loads were applied via weights that were uniformly put on a 1-m section in the middle of the strip. However, for the along-strip loading, the strip was hung up and fixed on the ceiling from one end and loaded from the other. Photos of the loading orientations are shown in Figure 2.5. The loads were chosen such that they resulted in the same stress range, i.e. below 10000 Pa for all of the orientations. The stress σ is derived from these loads using $\sigma = mg/A_c$, where m is the mass, g the gravity constant $g = 9.81 \, \mathrm{m/s}^2$, and A_c the surface area of the cable to which the load was applied.

In Figure 2.7a and b, the results of in-line and broadside measurements are shown. We can see that the measured Brillouin frequency shift (f_B) for both orientations show opposite behaviour; that is, increasing stress in the in-line orientation caused a decrease in frequency shift as shown in Figure 2.7a, whereas increasing stresses in the broadside orientation causes an increase in frequency shift as shown in Figure 2.7b. In Figure 2.7c, the along-strip measurements are shown. Here, a decrease in f_B as stress increases is observed. This is consistent with what was expected.
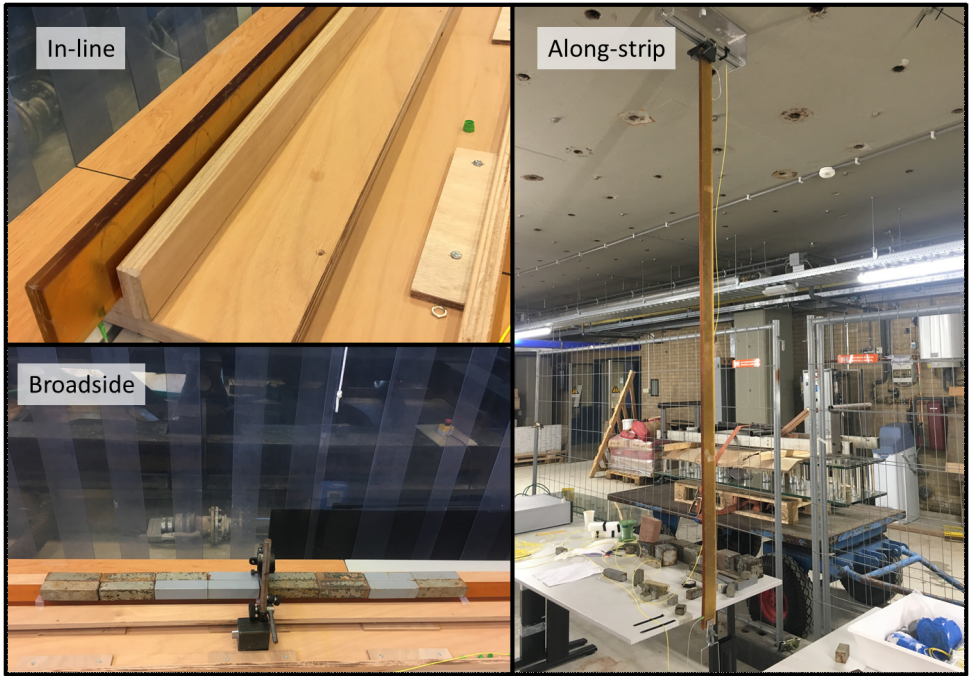
Figure 2.5: *Photos of In-line, Broadside and Along-strip loading cases of the Conathane® strip.*
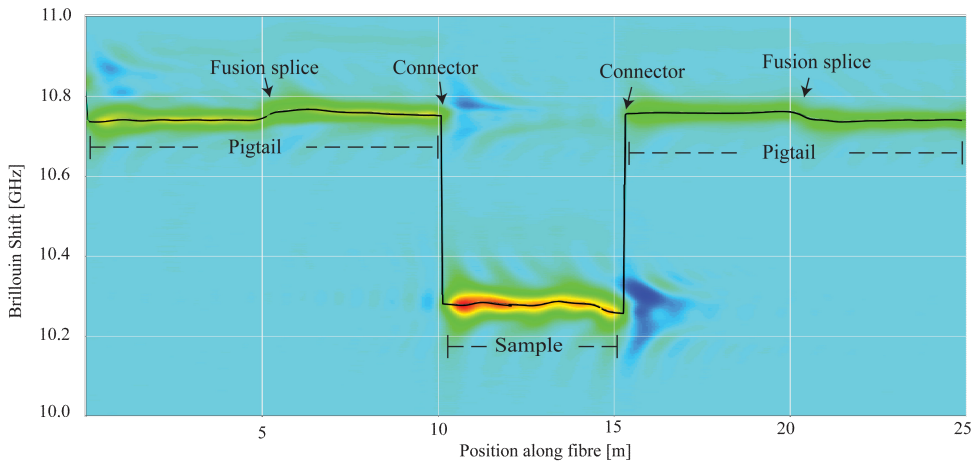

Figure 2.6: *Reference spectrum of Brillouin frequency shift (f_B). Note that the sample includes extra fibre at both ends for the terminations.*
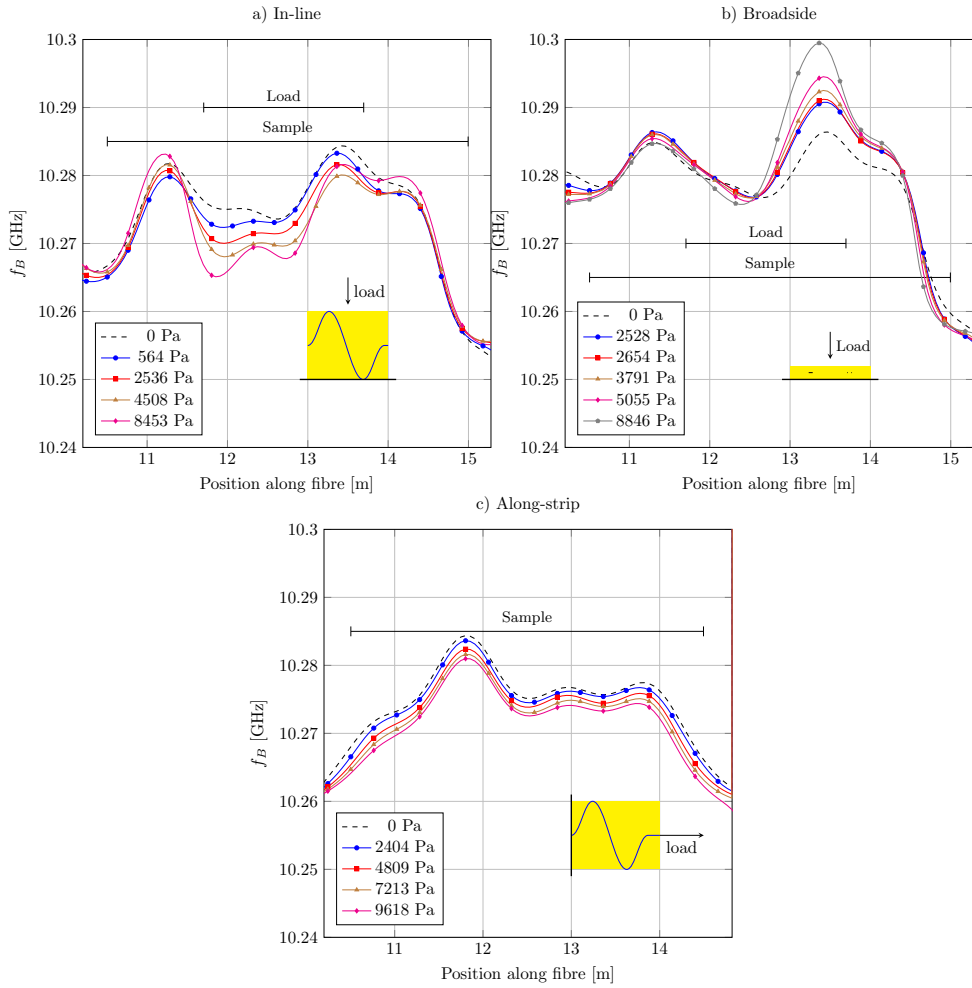
Figure 2.7: *Profiles of Brillouin frequency shift for (a) in-line, (b) broadside and (c) along-side loading.*

To quantify the sensitivity to strain, the difference in frequency shift f_B for each stress relative to a reference measurement (i.e. when no stress is applied) is shown in Figure 2.8a. The average value for each change in frequency shift (Δf_B) is determined and plotted against the absolute value of the applied strain, ε_{ii}. The applied strains are derived using $\varepsilon_{ii} = \sigma_{ii}/E_c$ for the average value of Young's modulus ($E_c = 17$ MPa). Note that the variations in Young's modulus (i.e. Table 2.1) are incorporated in the error bar for the horizontal axis by calculating the lower and upper bounds of the applied strains (Figure 2.8b).

As can already be seen in Figure 2.7, the change in Brillouin frequency shift is not constant along the profile, while the load was applied uniformly. Alongside with the limited spatial resolution, these variations could be caused by the difference in thickness along the strip or the non-uniform pre-straining of the fibre during the manufacturing process resulting in imperfectly distributed deformation. Also, the strain transfer is not uniform due to the varying angle of fibre with the principle direction of strain. As previously mentioned, fibre shaping affects the strain transfer between the embedding material and the optical fibre as modelled by *Sun et al.* [2016] and illustrated by our results as variations in the measured Δf_B profiles, especially in the in-line and broadside loading cases. It is also important to note that existing strain-transfer models assume a fibre sensor with fixed ends which is not directly applicable to our sample.

To accommodate these variations and the limited spatial resolution, an average $\overline{\Delta f_B}$ of the differences in the frequency-shift normalised by the strain coefficient C_ε is calculated over a window W corresponding to the load position (Figure 2.8). This should be equivalent to the fibre strain ε_f as described by equation 2.3.1. The strain coefficient C_ε used is 0.050 MHz/$\mu\varepsilon$. Note that C_ε was not measured for the embedded fibre, and typical corner values of 0.040 and 0.060 MHz/$\mu\varepsilon$ are used to evaluate the vertical error bars.
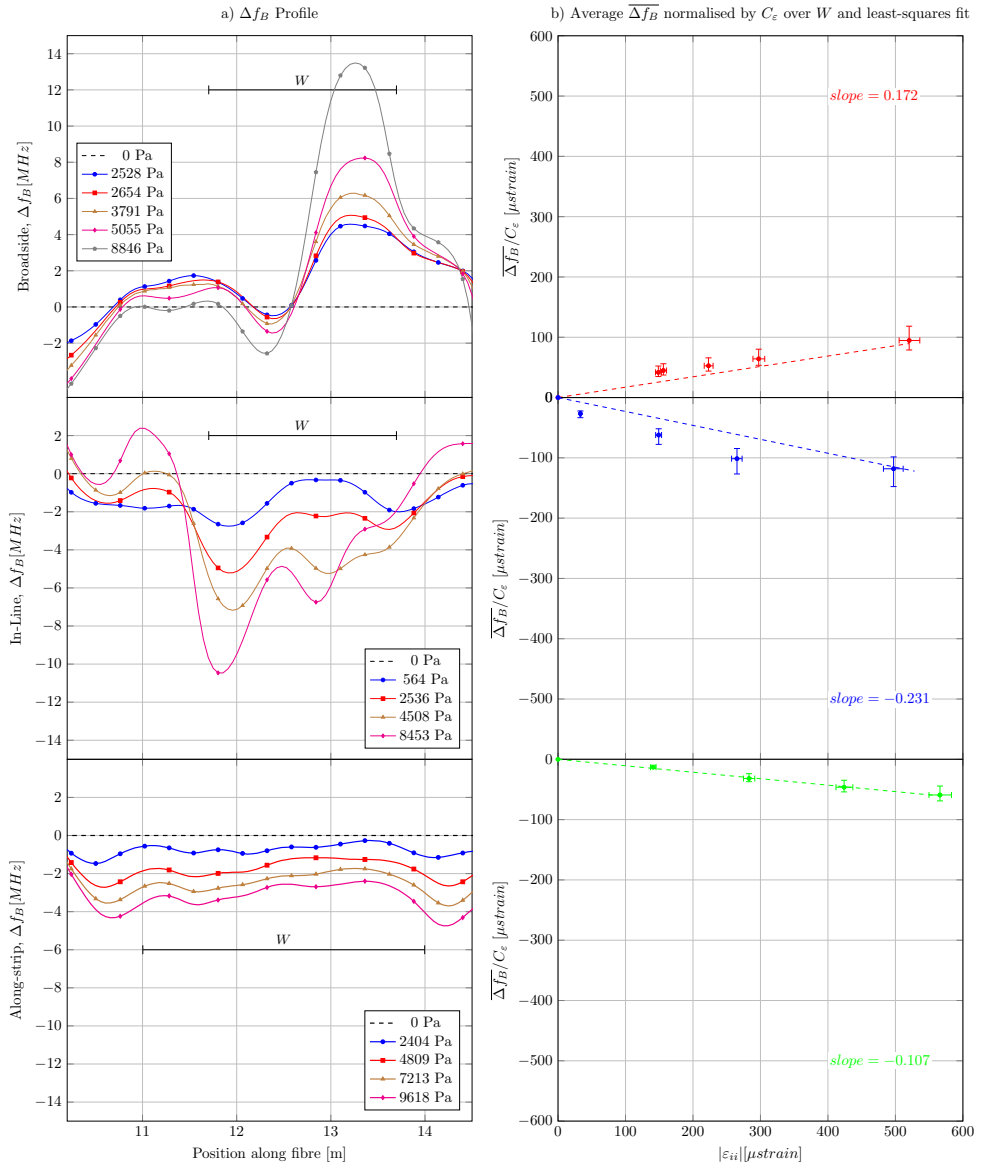
Figure 2.8: *Analysis of differences in Brillouin frequency shift. a) Differences in profiles compared to the reference (zero-load) case, with analysis window W indicated. b) $\overline{\Delta f_B}/C_\varepsilon$ in $\mu\varepsilon$ (dots) as a function of applied strain, where bar above Δf_B means average over window W. Dashed lines are least-squares linear fits with slopes, i.e., sensitivities, given; corrections for intercept afterwards applied to force the lines to go through the origin.*

2.4   Modelling versus experiments

Here we compare our measurements to our analytical and numerical models. The modelled fibre strain is calculated using equation 2.2.12. As previously mentioned, due to the varying angle of the fibre and the limited spatial resolution, we expect that our strain transfer to be variable across the sinusoidally shaped fibre. This is especially clear in the broadside and in-line cases where the load is in the middle. Therefore, an average strain transfer coefficient ξ is introduced to fit the measurements as previously described in equation 2.2.13.
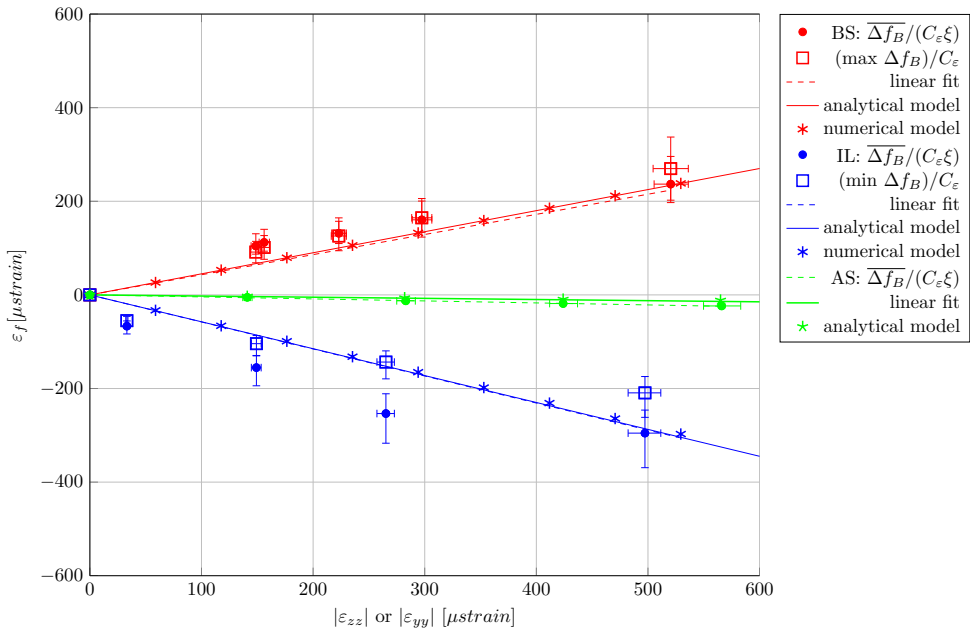

Figure 2.9: *Comparison between measured $(= \overline{\Delta f_B}/(C_\varepsilon \xi))$ and modelled ε_f for in-line and broadside orientations.*

Calculating an average strain transfer for one sinusoid where the average angle is $52°$ gave a value of 0.64. However, since our spatial resolution does not correspond exactly to one sinusoid, this value can vary. For instance, for an angle of $60°$, the average strain transfer coefficient is 0.4.

For the in-line and broadside orientation, the strain transfer coefficient ξ found to fit the measurements is 0.4. Using such a value, Figure 2.9 shows that a good agreement between the scaled mean value $(\overline{\Delta f_B}/(C_\varepsilon \xi))$ and the model is achieved. We could also see that we get a good fit if we analyse the maximum value of Δf_B in the broadside case and the minimum value of Δf_B in the in-line case. This supports the idea that for these two cases, where the loads were locally applied, the variation in the strain transfer is readily apparent. On the other hand, for the along-strip

case, the inverse of this factor, i.e. $\xi = 2.5$, is needed to fit the data. That is, the measured strains are higher than expected by the model.

Even though the exact value of C_ε is unknown, its impact on the variation of equivalent strain values is quite limited as illustrated by the small vertical error bars in Figure 2.9. To compare the sensitivities in the different orientations, the ratio of the slopes would provide a suitable measure. We find that between in-line and broadside orientation, the modelled ratio is 1.28 and the ratio based on the least-squares fits to the mean measurements is 1.34. The small variation between the two ratios could be related to the variations in the Δf_B measurements as discussed earlier.

2.5 Discussion

As it can be seen the model describes the behaviour we observe from the measurements with the Conathane® sample. Quantitatively, there are some issues:

- The broadside sensitivity is seen as mainly due to the Poisson effect of the embedding material, i.e., the strip/cable of Conathane®. What would be ideal for a unidirectional sensitivity is that the embedding material would have a Poisson ratio of zero which is very hard to achieve.

- For the Conathane®, a separate small experiment took place to determine Young's modulus and Poisson's ratio, but those were measured at relatively large strains, in the order of 10 mε rather than 0.1 mε. Determining Young's modulus and Poisson's ratio of Conathane® at lower strain values would give more accurate values.

- For the along-side case, the analytical and numerical models describe the measured strain qualitatively (i.e. shortening of the fibre). However, quantitatively the measured strain exceeds what is expected with a factor of 2.5. This is unlike what was found in the in-line and broadside cases, where the measured strain of the fibre is lower than the modelled strain. We attribute this to the fact that for the along-strip case, small variations in the mechanical properties of the embedding material and the geometrical parameters of the sinusoidally shaped fibre would have a significant impact on the sensitivity as it is illustrated by Figure 2.2. This could be the case for our sample.

■ Recommendation to obtain 3-component data from a system of 3 cables

Even though the sinusoidally shaped fibre would not allow a unidirectional measurement, a system of three cables consisting of a straight fibre and two sinusoidally shaped fibres (embedded in perpendicular planes) will allow determining the different components. We will call these fibres f_1 for the straight fibre, f_2 for the first sinusoidally shaped fibre embedded parallel to the $xy-$plane, and f_3 the second sinusoidally shaped fibre embedded parallel to the $xz-$plane (see Figure 2.10). When such a system of cables is embedded in the medium,

let $\vec{\varepsilon}$ be the strain vector to be determined, and $\vec{\varepsilon_f}$ the strain measurements from the different fibres.

Then, the measurements $\vec{\varepsilon_f}$ can be expressed in the components of $\vec{\varepsilon}$ by:

$$
\begin{bmatrix} \varepsilon_{f_1} \\ \varepsilon_{f_2} \\ \varepsilon_{f_3} \end{bmatrix} = \begin{bmatrix} 1 & -\nu_c & -\nu_c \\ -S_{AS} & S_{IL} & -\nu_c \\ -S_{AS} & -\nu_c & S_{IL} \end{bmatrix} \begin{bmatrix} \varepsilon_{xx} \\ \varepsilon_{yy} \\ \varepsilon_{zz} \end{bmatrix}, \tag{2.5.1}
$$

where ν_c is the Poisson's ratio of the cable material, and S_{IL} and S_{AS} are derived empirically from the modelling. S_{IL} can be derived from the in-line sensitivity case of the sinusoidally shaped fibre. S_{AS} is the along-side sensitivity of the sinusoidally shaped fibre. Both S_{IL} and S_{AS} are dependent on the geometry of the fibre, namely the amplitude of the sinusoid (A) and the wavelength (Λ) as well as the Poisson's ratio of the material. Expression 2.5.1 is can be written as: $\vec{\varepsilon_f} = \mathbf{S}\vec{\varepsilon}$,

where $\mathbf{S}$ is the sensitivity matrix. Since the determinant $\det \mathbf{S} (= S_{IL}^2 - 2S_{IL}S_{AS}\nu_c - 2S_{AS}\nu_c^2 - \nu_c^2) \neq 0$, $\mathbf{S}$ is invertible. Therefore, the strain vector $\vec{\varepsilon}$ can be retrieved from the measurements $\vec{\varepsilon_f}$ by

$$
\vec{\varepsilon} = \mathbf{S}^{-1}\vec{\varepsilon_f}. \tag{2.5.2}
$$

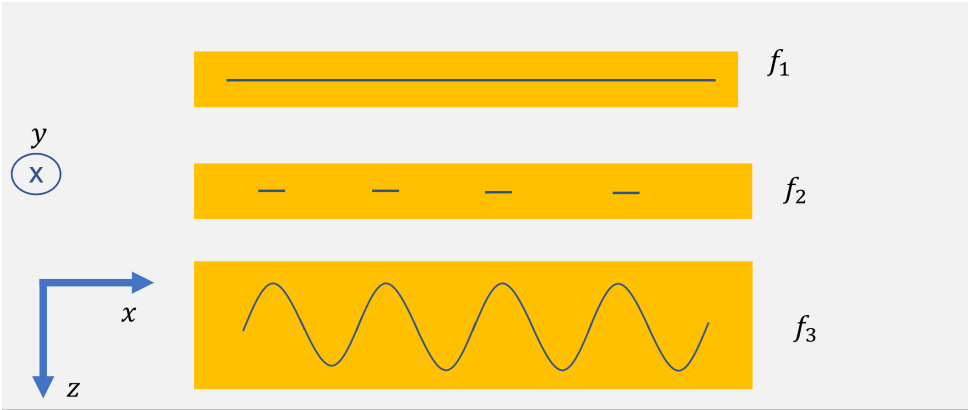This allows applications of multi-component measurements with such a configuration.

Figure 2.10: *Three cables embedded in a medium: f_1 is the straight fibre, f_2 sinusoidally shaped fibre in $xy-$plane and f_3 sinusoidally shaped fibre in $xz-$plane.*

2.6   Conclusion

The concept of a sinusoidally shaped fibre was adapted in this study to enhance the directional sensitivity. Analytical and numerical modelling and Brillouin-scattering-type experiments were carried out on a 2-m polyurethane (Conathane®) strip embedding the shaped fibre. To examine its sensitivity to in-line, broadside and along-strip deformations, loads were applied in these orientations, where an opposite behaviour was observed between in-line and broadside orientations: a negative strain with increasing in-line compressive stress and a positive strain with increasing compressive stress in broadside orientation, with a slight difference in the sensitivity in these two orientations. For along-strip orientation, the increasing tensile stress caused fibre shortening, so a negative strain.

Our developed model describes the observations quantitatively, but some uncertainties are limiting a quantitative estimation of the sensitivity. These uncertainties pertain to the strain coefficient C_ε of the fibre as well as low-strain measurements of the elastic properties of the embedding material E_c and ν_c. Still, the model highlights the importance of the Poisson's ratio in the broadside orientation and can be also used to optimise the sensitivity in the in-line orientation based on the amplitude A of sinusoidally shaped fibre and its wavelength Λ. Although polyurethane material (in our case Conathane®) is not directly suitable for unidirectional strain measurements using a single sinusoidal fibre, however, we suggest that the use of a combination of two sinusoidally shaped fibres and a straight fibre would allow that.

Acknowledgements

3

Improvements in directional strain sensing using low-Poisson-ratio structures: concepts, using physical and numerical modelling

Abstract   A multi-component strain sensor using a combination of sinusoidally shaped fibres proved to be challenging as shown in the previous chapter. The Poisson's ratio of the embedding material was observed to play a significant role in determining the sensor's directional strain sensitivity. Therefore, in this chapter, we examine a novel concept of embedding the optical fibre in a low-Poisson-ratio (Low-PR) meta-material. This examination includes the prototyping of the low-PR structures using 3D printing technology, static-strain laboratory experiments on a physical sample and some numerical-modelling experiments using COMSOL ™. From the physical experiments, we found that in-line to broadside sensitivity has a ratio of 1.63 which is an improvement compared to a value of 1.34 as found in the previous chapter. Using numerical modelling, we illustrate that further improvements are possible. Finally, we discuss the challenges with the implementation of such a concept.

3.1   Introduction

Due to the very nature of a DAS measurement, i.e. a sensing fibre elongated in a specific direction, it is considered a single-component measurement. It is maximally sensitive along the fibre's axial direction which means that the fibre is significantly less sensitive to broadside waves [*Mateeva et al.*, 2017]. A helically wound fibre/cable (HWF/HWC) was introduced to make the sensing omnidirectional, e.g. sensitive to broadside waves like vertically impinging P-wave reflections when the fibre is deployed horizontally, [*Kuvshinov*, 2016; *Hornman*, 2017; *Urosevic et al.*, 2018]. Other attempts include the use of different helical winding configurations as shown in *White et al.* [2022] and using shallow vertical boreholes to get a surface seismic image [*Bakulin et al.*, 2017]. As for multi-component DAS measurements, multi-component sensors are conceptualised from a purely theoretical perspective with the work of *Innanen* [2017]; *Ning and Sava* [2018a] but no experimental success has been shown yet with these approaches and the only early-stage implementation of a multi-component field experiment using DAS is reported by *Innanen et al.* [2018].

     As introduced in the previous chapter, our concept involves the use of a combination of three directionally sensitive cables to decouple a seismic wavefield into its three components. This includes two perpendicular sinusoidally shaped fibres and one straight one. Ideally, we want each of these fibres to be significantly more sensitive in a particular direction. However, as shown in the previous chapter, it turned out not to be straightforward to implement. This result was obtained by embedding a fibre in a homogeneous material where the fibre deformation was highly influenced by the Poisson's ratio of the embedding material. In that case, the fibre was only slightly more sensitive in one direction, i.e. in-line, compared to another direction, i.e. broadside. These directions are shown in Figure 3.1

     Here, a novel approach to enhance the directional sensitivity is introduced. This is done by adapting a meta-material that has some anisotropic features that allow us to control the directional sensitivity as desired. Ideally, this material should have a zero-Poission-ratio (zero-PR) in a certain direction, however, this is not attainable in practice as we will see later. Therefore, we will be referring to it as a low-Poisson-ratio meta-material instead for the rest of the chapter. In this chapter, we illustrate the concept of low-PR cable and the predicted improvements via this approach. This is followed by introducing the physical prototyping of the low-Poisson's ratio meta-material as well as conducting a physical experiment for such a prototype. Finally, a discussion on where the work is heading, based on numerical modelling, is included.

3.2   Concept of a directionally sensitive strain sensor

Based on what is shown in the previous chapter, it was observed that the deformation of a fibre is highly influenced by a cable's elastic properties as well as the geometrical parameters of the shape of the embedded fibre, in our case sinusoidally shaped. To obtain a directionally sensitive fibre-optic cable, the geometrical parameters of the fibre can be easily adapted, however, this is not the case for the

elastic properties of the embedding material. So, for this to work, we introduce anisotropy in the embedding material, such that the deformation of the fibre follows our desired behaviour. It was observed that the fibre is also significantly sensitive to the broadside direction, which is not suitable for a uni-directional sensor, so the aim here is to decrease the strain sensitivity in that broadside direction compared to the in-line direction.
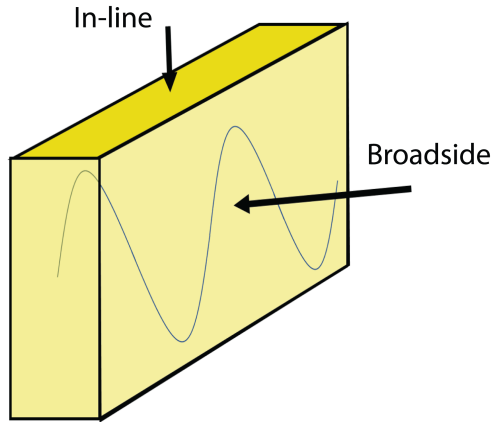

Figure 3.1: In-Line vs. Broadside Orientations.

Ideally, we want the fibre to not experience any deformation for the broadside direction, i.e. the Poisson's ratio should be zero in all directions. However, such material is complicated if not impossible to design, let alone manufacture. That is why we adopted a concept where the embedding material has a low-PR in one direction as illustrated in Figure 3.2. This low-PR material is a meta-material made of a special structural arrangement such that the deformation can be influenced as desired. In our desired case, if a load was applied to the cable causing a strain of ε_{yy}, the fibre will not be deformed in the z-direction as shown in Figure 3.2. However, the fibre will still be deformed in the x direction in response to that broadside load. In other words, the embedding material will have two Poisson's ratios, the first one is zero, i.e. $v_{c,yz} = 0$, and the second one is the Poisson's ratio of the material making up the structure. Although the fibre will still be deformed in the x-direction, its effect can be compensated for using a straight fibre.

■ **Improving the directional strain sensitivity**

To have an idea about the improvements in the in-line directional sensitivity compared to the broadside direction, we extend the analytical model, introduced previously in chapter 2, to accommodate for a low-Poisson's ratio material following the concept shown in Figure 3.2. Two improvements can be implemented; the first one changing the geometrical parameters of the sinusoid and the second one changing the Poisson's ratio of the (meta-)material.

Following the analytical model introduced in section 2.2, it can be extended to include a material with a Poisson's ratio of zero in the z-direction. The formulas to calculate the arc length of the undeformed fibre and the deformed one in the in-line direction are the same, whereas the arc length of the deformed fibre in the broadside direction has been adapted.
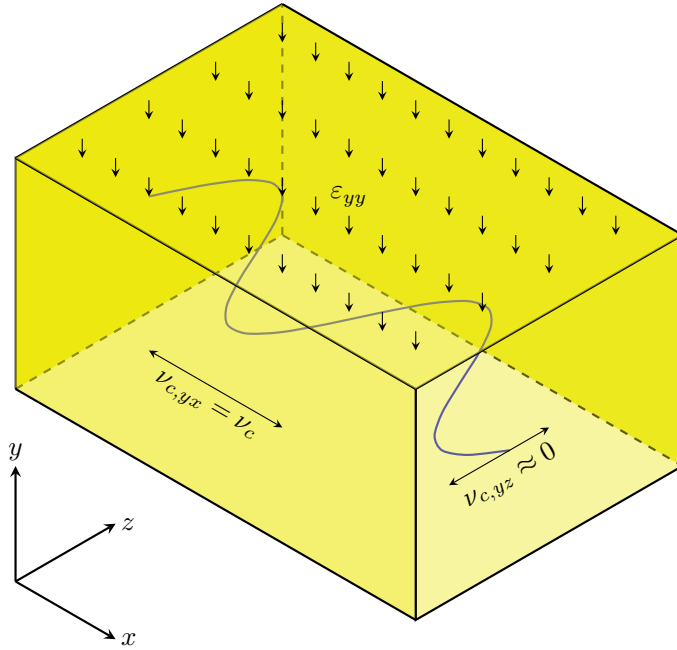

Figure 3.2: *Concept of sinusoidally shaped fibre embedded in cable with low-Poisson's ratio $\nu_{c,yz}$ in z-direction due to broadside strain (ε_{yy}).*

The lines in Figure 3.3 show the effect of changing the Poisson's ratio on the fibre sensitivity and how that can be influenced by changing the geometrical parameters. In Figure 3.3a, we see that the broadside sensitivity is significantly influenced by changing the Poisson's ratio of the material, i.e. lower sensitivity is found with lower Poisson's ratios. Conversely, the in-line sensitivity is influenced in the opposite fashion, i.e. the sensitivity is increased with lower Poisson's ratios but with smaller changes compared to the broadside case. On the other hand, Figure 3.3b shows the dominance of changing the amplitude of the sinusoid, i.e. $A = 4.8$ cm, in the sensitivity of the in-line direction. The changes in in-line sensitivity are negligible between the various Poisson's ratios with such change in amplitude of the sinusoid, unlike the quite significant decrease in sensitivity in the broadside direction. To summarise all this, the ratio between the in-line sensitivity (S_{IL}) to the broadside sensitivity (S_{BS}) for various Poisson's ratios is calculated and contained in Table 3.1.

Table 3.1: *Calculated ratios between in-line strain sensitivity S_{IL} to broadside strain sensitivity S_{BS} for various Poisson's ratios ν_c and amplitude A of the sinusoidally shaped fibre.*

ν_c	0.45	0.3	0.2
	$\lvert S_{\mathrm{IL}}/\ S_{\mathrm{BS}}\rvert$:		
$A = 2.4$	1.67	2.69	4.24
$A = 4.8$	3.11	4.68	7.05

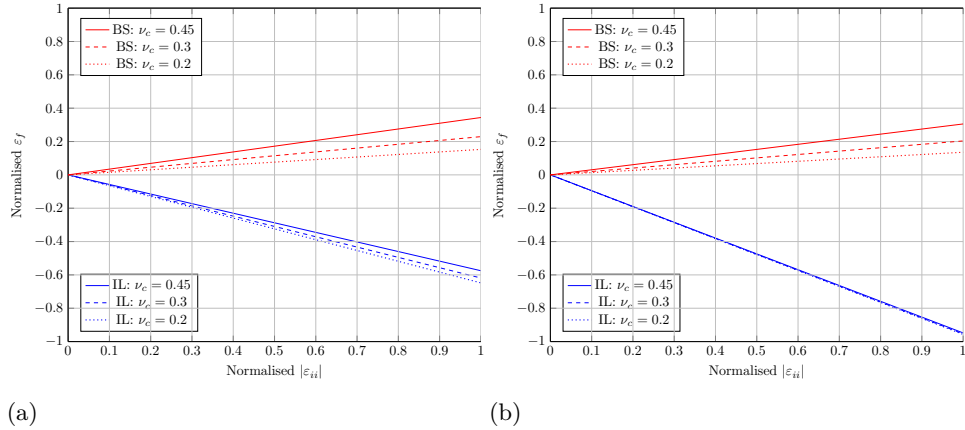(a)   (b)

Figure 3.3: *Fibre strain ε_f for broadside (BS) and in-line (IL) orientations, normalised by the maximum applied strain, as a function of in-line normalised applied strain for various Poisson's ratios with (a) $A = 2.4$ and $\Lambda = 6$ (in cm) and (b) $A = 4.8$ and $\Lambda = 6$ (in cm)*

3.3 Concept of embedding material with low-Poisson's ratio

■ Physical Modelling and Prototyping

In collaboration with Prof. dr. ir. S. van der Zwaag and Dr. Reza Hedayati from the Novel Aerospace Materials section at the TU Delft, the concept of low-Poisson's ratio embedding material is adopted. Here we use the approach from *Hedayati et al.* [2018], to construct a low-Poisson's ratio (low-PR) metamaterial as described in the previous section. The construction is based on combining two unit cells as shown in Figure 3.4; one is a hexagonal unit cell and the other is a re-entrant ("diabolo"-shaped) unit cell. The basic idea is that when compressed in the y-direction, the hexagonal unit cell will extend in the z-direction, whereas the re-entrant unit cell will compress in that direction. The total displacement will result in a movement of zero, i.e. a low-PR effect in the z-direction.
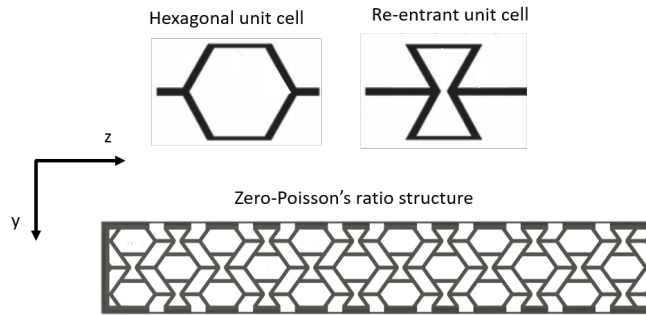
Figure 3.4: *low-Poisson's ratio structure using hexagonal and re-entrant ("diabolo"-shaped) unit cells.*

To make a physical prototype, firstly, a computer drawing of the profile of the 2D low-PR structure was made (using the software Fusion360 ™). This profile was extruded in the other direction to construct the 3D model. Secondly, in order to create a physical prototype of the structure, use was made of a 3D printing device. It is essential to have excellent 3D printing quality to represent the computer 3D model as closely as possible. The design of the structure has been through a number of stages as shown in Figure 3.5. This includes going from the initial stage Figure 3.5a to the final one 3.5d, where between these stages, the prototype has improved in printing quality significantly due to the use of a more accurate 3D printing technology, the design has been adapted to become bigger in size, allowing further improvement in the printing quality and adaptations in geometrical parameters of the embedded sinusoidally shaped fibre (Figures 3.5b and 3.5c). It was also observed that the sidewalls of the structures affect the stiffness in the in-line direction significantly, thus it was adapted to the one in Figure 3.5d.

3.4   Static-strain experiment with Brillouin Optical Time Domain Analysis (BOTDA)

■ Principle of stimulated Brillouin scattering

This method works by stimulating the fibre with a pulse wave and a continuous wave, injected via lasers at both ends of the fibre. The interaction between these waves and the glass fibre material will stimulate Brillouin scattering in the glass at a characteristic frequency, which is equivalent to a characteristic frequency shift between the two waves called the Brillouin frequency shift f_B, which is what is measured by a BOTDA interrogator [*Zhang and Wu*, 2007]. Further details on the principle are discussed in section 2.3 though in that section the device makes the analysis to derive the frequency shift in the frequency domain instead of in the time domain like is done here.
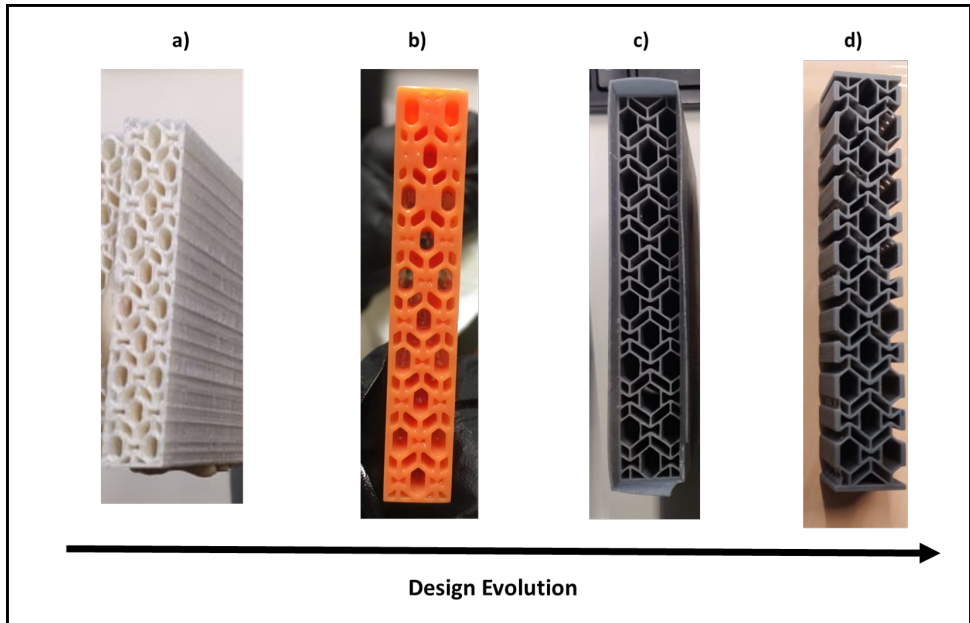
Figure 3.5: *Design evolution of 3D-printed low-PR samples. a) Stiff-material print (made of Polylactic acid); b) low-quality resin print; c) high-quality resin print; d) adapted design.*

■ The sample

In order to embed a sinusoidally shaped fibre within the structure, a full sample was constructed via two halves. Its length was 0.6 m. Due to limitations in the dimensions of the 3D printer, each half was constructed via six elements, each of which has dimensions as shown in Figure 3.6, and were glued to each other to make up one full half of the sample. The fibre was glued in a groove, printed in one half only. The other half without a groove was then glued on top of it. At both ends, the fibre was spliced to a 10-m pigtail with E2000/APC connectors as shown in Figure 3.7. The sample was made with a grey resin from the 3D printing company FormLab. Based on the datasheet, the material has a Young's modulus of 2.8 GPa and a Poisson's ratio of 0.35. No peer-reviewed articles were found to confirm these values.
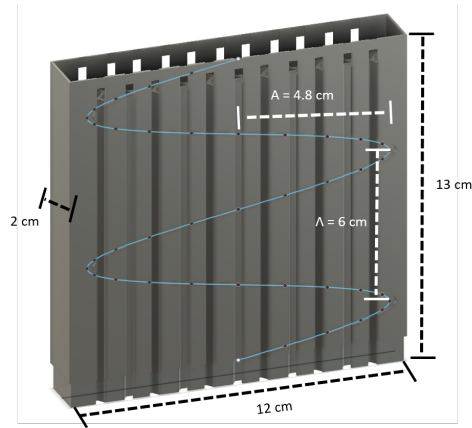
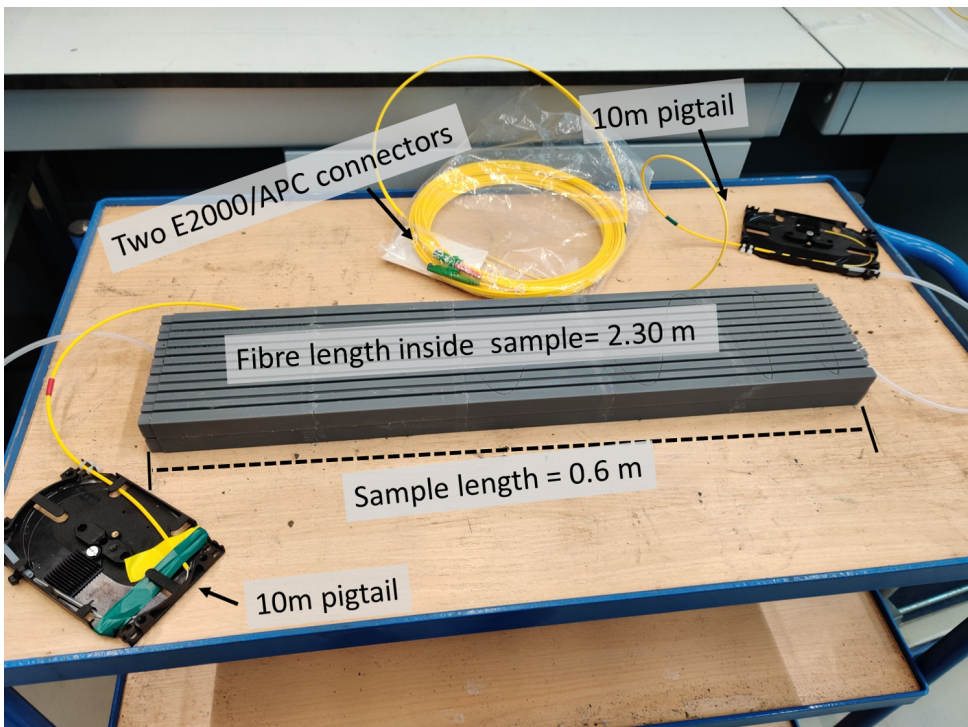**Figure 3.6:** *A single 3D printed element and its dimensions.*

Figure 3.7: *The whole sample and its connections to the BOTDA system.*

∎ Set-up of experiment

The sample was connected via mating sleeves to two pigtails that have an E2000/APC connector at one end and a FC/APC connector at the other end. These were directly connected to the BOTDA Neubrescope™ system, type NBX-6066, as shown in Figure 3.8. This system is controlled via software on a separate PC and allows tuning the parameters of the measurement, initiating and taking measurements, as well as storing and analysing the data. The main parameters to optimise are the scan range of the Brillouin Frequency Shift (f_B), the frequency resolution and the spatial resolution. In order to optimise the measurement time, we chose to scan between 10.14 to 10.3 GHz with a frequency resolution of 1 MHz. The spatial resolution used is 10 cm. The sample was loaded in two orientations in this experiment, namely in the in-line and broadside ones. The loadings in the in-line and broad-side directions were achieved by applying weights on top of the samples in respective orientations, as shown in Figure 3.8.
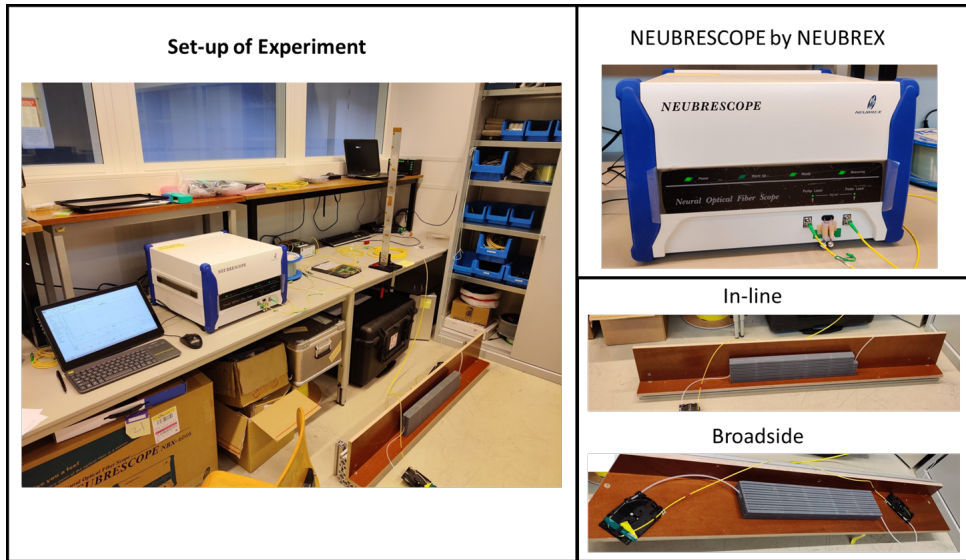
Figure 3.8: *Experimental set-up of the low-PR sample using BOTDA Neubrescope™ system.*

∎ Experimental results

To compare the directional sensitivity between the in-line and broadside directions, loads were uniformly applied on a 0.5-m section of the sample, which is equivalent to 2 m of fibre, within the same stress range of 0 to 7000 Pa as the homogeneous-embedding material (i.e. Chapter 2). The stress $\sigma_{(xx,yy,zz)}$ is derived from these loads using $\sigma = mg/A_c$, where m is the mass, g the gravity constant $g = 9.81\,\text{m/s}^2$,

and A_c the surface area of the sample to which the load was applied.

The difference in Brillouin frequency shift is calculated for the different loads by taking the difference of each measurement to a reference measurement, in our case the one where no weight is applied, as shown in Figure 3.9. The results showed opposite behaviour between the two orientations as expected, i.e. an increase in f_B for broadside orientation and a decrease in f_B for in-line orientation.

To calculate the difference in sensitivity, the average of the difference of frequency shift, that is normalised by the strain coefficient C_ε, i.e. $\overline{\Delta f_B}/C_\varepsilon$ is calculated for a C_ε of 50 MHz/1000 $\mu\varepsilon$ using the expression 2.3.1. Note that, even though C_ε is not known, it is sufficient to convert the values to fibre strains as the focus is on the ratio between the in-line and broadside sensitivities, not the absolute values themselves. The average of the fibre strain is calculated between the fibre position of 16.4 to 18.4 m, which is the position of the load, and plotted against the applied stress. We compare the sensitivity by taking the ratio between the in-line and broadside slopes against the applied stress, where it was obtained to be 1.63.

Although we see improvement in the sensitivity in favour of the in-line direction compared to the broadside direction, it is only a 20% improvement compared to what was obtained from the sinusoidally shaped fibre embedded in the homogenous material. That is not high enough to consider our concept to be a directional strain sensor. It is still unclear if the cause of such low sensitivity is that the fibre is not following the overall structure but instead, there is a contribution from the mechanical properties of the material that the structure is made of. Here, we have estimated the sensitivity ratio using the slopes against the applied stress, which is equivalent to what was done previously in Chapter 2 for the sinusoidally shaped fibre as a single Young modulus was used to convert the applied stress to strains. However, for the low-PR structure, the conversion to strain is not straightforward. This is due to the difference in stiffness that is dependent on the direction of loading in the case of the low-PR structure.

A full discussion of these results, including comparisons to modelling results, is given after the next section in which numerical modelling is discussed.

3.5 Numerical modelling

In order to understand the low-PR behaviour of the structures and allow us to further optimise the design of the low-PR sensing cable, modelling is necessary. The optimisation includes the placement of the sinusoidally shaped fibre in the structure as well as examining the effect of changing various parameters in the design. To those ends, a finite-element methodology was adopted, via the implementation in COMSOL Multiphysics®. With the software module Solid Mechanics, the mechanical behaviour of the cable can be modelled in 2D and 3D.
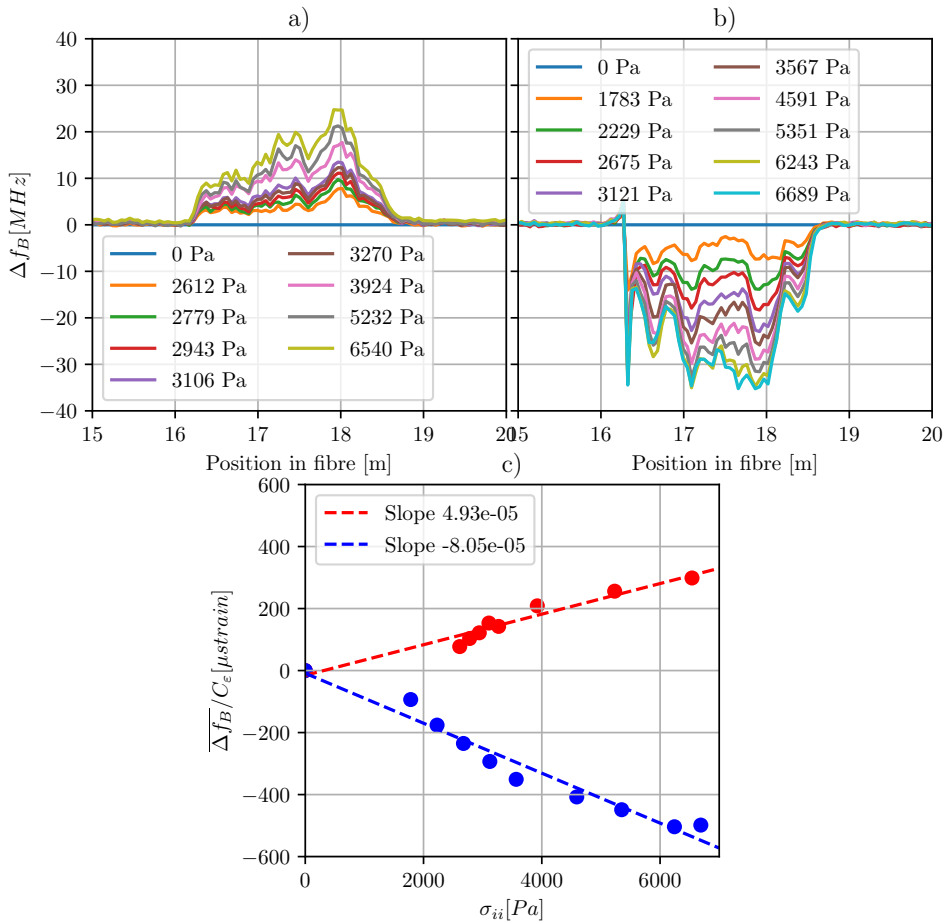
Figure 3.9: *Experimental results: differences in Brillouin Frequency Shift and their associated strains, compared to a reference (=zero) load for a) broadside and b) in-line loading. In c) and d), $\overline{\Delta f_B}/C_\varepsilon$ in $\mu\varepsilon$ (dots) as a function of applied stress is shown. A least-squares line fit is also calculated and shown, to estimate the stress sensitivity over fibre position between 16.4 to 18.4 m for broadside (c) and in-line (d) loads.*

■ The model for a low-Poisson ratio metamaterial

The model was constructed as a structure profile in the yz-plane and extruded into the x-direction. It has the same dimensions overall except for the sidewalls that have been removed here (see Figure 3.5d and Figure 3.10b). The model material is populated with elastic properties within the range of those of plastics, i.e., a Young's modulus of 3.2 GPa and a Poisson's ratio of 0.35. The dimensions of the sample are shown in Figure 3.10a: the length of the sample, i.e. extended in the x-direction,

is 120 mm, its width (in the z-direction) 120 mm, and its thickness 38 mm. As shown in Figure 3.10b, the internal walls of the structure have a thickness of 0.8 mm same as the physical 3D-printed sample. The fibre is embedded in the middle of the model as marked in red in Figure 3.10b. This assumes that the fibre is following the embedding material.

The boundary conditions for both loading cases are specified in Figures 3.10b and 3.10c. For the broadside direction, we have a boundary load on the top of the sample in the $(-x)$ direction with a fixed lower boundary, i.e. the displacement vector of the lower boundary of the sample is set to zero ($\mathbf{u} = \mathbf{0}$). The other boundaries are free ones. As for the in-line direction, one side is fixed and a boundary load is applied in $(-z)$ direction on the other side. The model has a mesh of free tetrahedrals with a minimum and maximum element size of 1.2 and 9.6 mm, respectively.

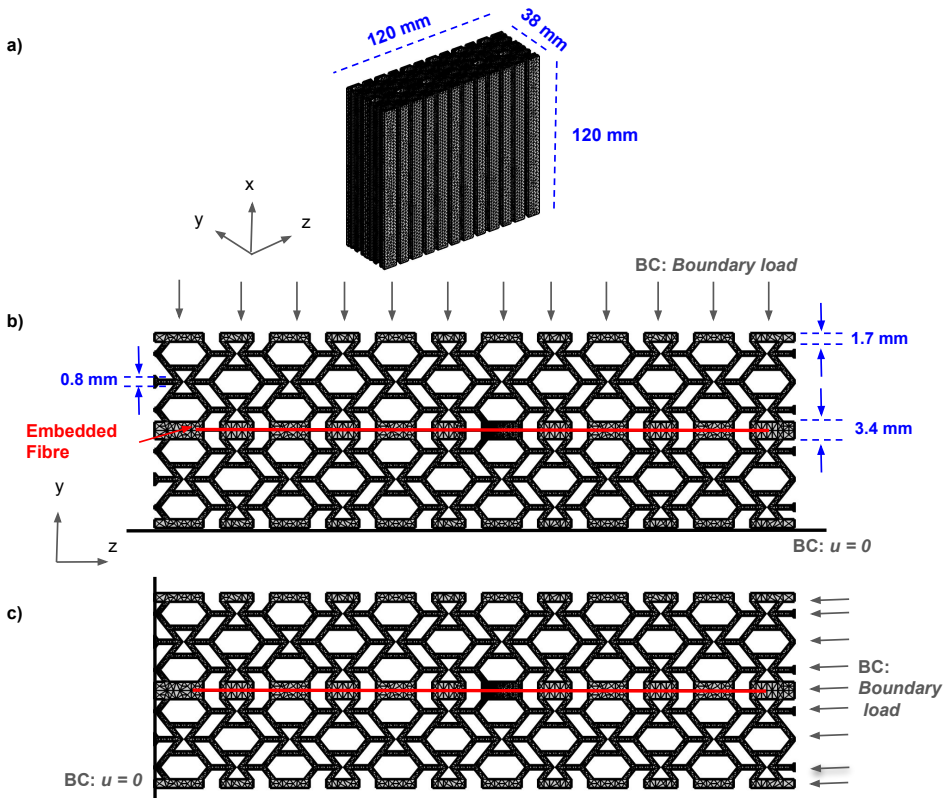**Figure 3.10:** *The 3D numerical model of a low-Poisson's structure with embedded sinusoidally shaped fibre with the dimensions (a) and the boundary conditions for broadside (b) and in-line (c) loading scenarios. BC stands for boundary condition.*

■ Modelling results

In this part, we look at the results from the loading experiments described in Figure 3.10 with a uniform load of 5000 N/m^2. Figure 3.11 shows the results of the finite-element modelling. The embedded sinusoidally shaped fibre is illustrated in grey on top of the figure. The obtained displacement components are shown in Figure 3.11a for broadside loading and Figure 3.11b for in-line loading.

Displacement profiles

When looking at the responses in the different directions due to the load in Figure 3.11a and 3.11b, they look quite different. The contribution of the $x-$displacement seems to be quite minimal for both loading scenarios. As for the $y-$component, we see significant differences in the behaviour in broadside vs. inline. For the broadside loading, the fibre is displaced by a constant amount (i.e. $\approx -1\,\mu m$) and varies slightly around it. This is due to the embedded fibre passing parts of the structure with varying stiffnesses. As for in-line loading, the $y-$displacement, the embedded sinusoidal has a maximum at the boundary load and decreases towards the fixed end. Looking at the $z-$direction, which should be the main contributor to the displacement experienced by the embedded fibre, we could see that in the broadside case, the displacement is significantly decreased but not *zero*. This means that such arrangement at the local level does not completely have a *low-Poisson* behaviour, yet. On the other hand, for the in-line loading, the fibre is shortened as expected and discussed in the previous chapter. The step-like appearance in the obtained displacement profiles is due to parts with the traced fibre not passing the embedding material.

Strain

The strain along the fibre is then calculated for both loading BS and IL similar approach in expression 2.2.12 from the previous chapter. The strain values are plotted in Figure 3.11c. We can see variations in the strain values along the extent of the sample. The average strains were calculated with an average value of $-11.53\,\mu strain$ and $2.86\,\mu strain$ for IL and BS, respectively. By looking at the ratio of the mean strain, we get $|S_{\text{IL}}/\,S_{\text{BS}}| = 4.2$, which is much larger than what we got from the physical (BOTDA) measurements (i.e. $|S_{\text{IL}}/\,S_{\text{BS}}| = 1.63$). This difference in sensitivity obtained from the physical experiment and numerical modelling might suggest the assumption of the fibre completely following the structure is too simple. Instead, other factors that we are not considering might be at play as we will discuss next.
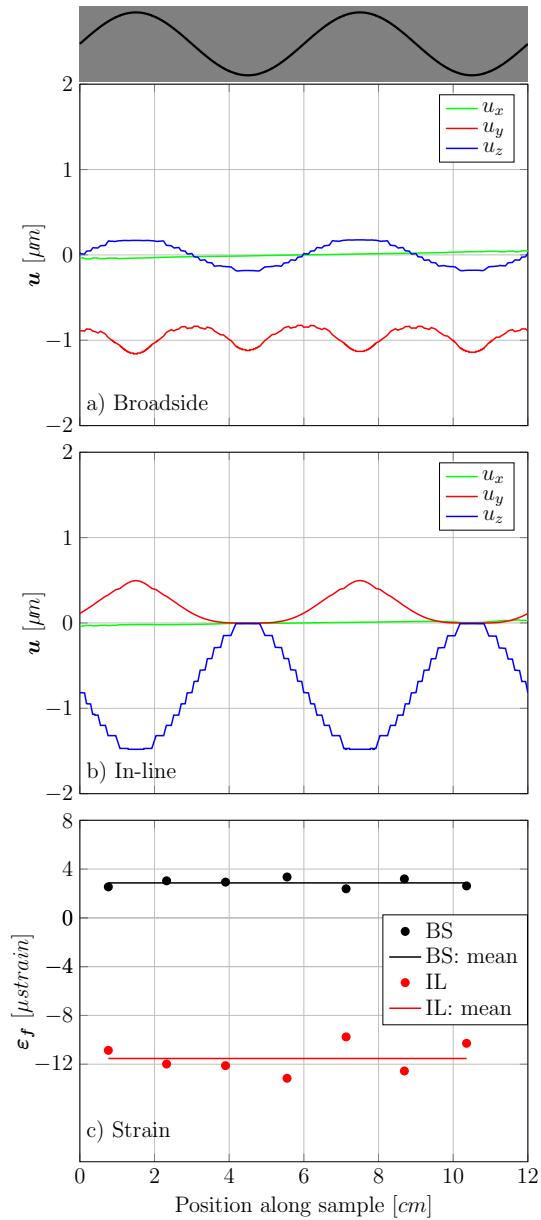
Figure 3.11: *Finite element modelling results show the displacements due to broadside (a) and in-line (b) loads and strain measured along the embedded fibre for both loading scenarios (c).*

3.6 Discussion

We investigated the concept of a directional strain sensor using an approach of embedding a sinusoidally shaped fibre in a low-PR structure. As the concept is still at an early stage and far from ready for DAS implementation, several issues remain. First of all, we looked at the static-strain response while dynamic-strain responses are the final aims for seismic applications. Also, the deformation of the fibre was examined with high spatial resolution while most currently available DAS interrogators do not provide centimetre-scale measurements. Another issue is that we need to know whether the overall fibre strain response follows the effective behaviour of the structure or whether other coupling mechanisms should be considered. Currently, in the numerical models, we are tracing the fibre along the structure, so therefore differences in the mechanical properties between the fibres and the low-Poission material are not considered. Another question is how the fibre should be optimally glued to the structure so it has a low-Poisson ratio behaviour in the broadside direction. Currently, it has been glued to the structure directly. We see that due to the way that the unit cells are arranged, the structure will have two different Young's moduli; one for the broadside direction and another for the in-line direction. This is also supported by *Hedayati et al.* [2018]. From our experience with the samples, it is easier to squeeze the structure in the broadside direction compared to the in-line direction, i.e. lower Young's modulus in the broadside direction. Then also, the Poisson's ratios will differ in the different directions. Physical measurements need to be performed to accurately obtain those.

So far, numerical modelling has shown that it is a useful tool to optimise the low-PR structure and the embedded fibre. Improvements in the design were introduced in the numerical model by removing the side walls to decrease the stiffness in the broadside direction as it turned out to have a significant effect on the parts of the fibre closer to the side walls. With this arrangement, we found improvement in the sensitivity ratio $|S_{\mathrm{IL}}/ S_{\mathrm{BS}}| = 4.2$. Improvements in the concept sensor could also include even further optimisation of the geometry of the low-PR structure as well as the fibre placement. For the latter, we currently trace a fibre passing along the structure which does not take into account the differences in the mechanical properties between the structure and the optical fibre.

3.7 Conclusion

In this chapter, we introduced a novel approach to decrease the broadside sensitivity of a sinusoidally shaped fibre embedded within a strip or cable of a low-Poisson's ratio meta-material. We modelled the improvements in sensitivity via the strain-sensitivity ratio $S_{\mathrm{IL}}/S_{\mathrm{BS}}$ that ranges from 1.7 to 7.1 depending on the Poisson's ratio of the matrix material making up the meta-material structure as well as the geometrical parameters of the sinusoidally shaped fibre. We discussed the construction of physical samples via 3D printing and the approach to constructing a cable. With a sample fabricated in such a way, the embedded fibre was connected to a BOTDA system and the directional sensitivity of the cable was examined for the

same range of stresses as the homogenous embedding material examined in the previous chapter. When comparing the in-line sensitivity to the broadside one via their stress-sensitivity ratio, a stress-sensitivity ratio of 1.63 was obtained, an improvement compared to the sensitivity ratio with a homogeneous-embedding material of 1.34.

4

Experiences with DAS using both straight and helically wound fibres

"Light brings us the news of the Universe."

William Bragg
The Universe of Light (1933)

Abstract   Distributed Acoustic Sensing (DAS) has been limited in its use for surface-seismic reflection measurements, due to the fibre's decreased broadside sensitivity when the fibre is deployed horizontally. Deploying the fibre in a helically wound fashion has the promise of being more sensitive to broadside waves (e.g. P-wave reflections) and less sensitive to surface waves than a straight fibre. We examine such claims and compare the responses of straight fibres (SF) and helically wound fibres (HWF) with different wrapping angles, using standard and engineered fibres. These fibres were buried in a 2 m deep trench in a farmland in the province of Groningen in the Netherlands, where we performed an active-source survey. We observe in our field data that using HWF has a destructive effect on the surface-wave amplitudes. Our data confirmed the effect of the wrapping angle on the polarity of the surface-wave arrival and the dampening effect of the helical winding, both behaving in quite a predictable fashion. Apart from the effect of the wrapping angle, the different design choices, e.g. cable filling and material type, did not show a significant effect on the amplitude of the signals. As for P-wave reflections, we observe that both engineered SF and HWF provide reflection images comparable to

those obtained from simultaneously deployed geophones at the surface despite the straight fibre's decreased broadside sensitivity. A polarity reversal and an amplitude difference between the SF and HWF fibres are observed. Finally, we show that the combined use of SF and HWF proved to be useful since SF showed better sensitivity in the shallower section and HWF in the deeper sections.

4.1 Introduction

Distributed Acoustic Sensing (DAS), sometimes called Distributed Vibration Sensing (DVS), has been widely adopted for a diverse number of applications. For borehole monitoring, DAS provides dense spatially sampled data. An equivalent dense spatial sampling using geophones will be very costly. One can install optical fibre for the whole length of the borehole and use it for continuous monitoring of either repetitive active-source seismic measurements (i.e. time-lapse seismic) or for passive monitoring, like for hydraulic fracturing [*Bakku*, 2015; *Karrenbach et al.*, 2019; *Becker et al.*, 2017]. A major benefit of using DAS over geophones in such settings is that it is not disruptive during the production process. As for active seismic, early adoptions of the technology were mostly in borehole seismic settings [*Mestayer et al.*, 2011; *Barberan et al.*, 2012; *Daley et al.*, 2013; *Mateeva et al.*, 2014; *Frignet and Hartog*, 2014]. The implementations of DAS in surface seismic have been limited mostly to the estimation of near-surface shear-wave velocities from surface-wave signals with either active or passive sources. Examples of the use of DAS with passive sources utilizing interferometric techniques for shear-wave velocity inversion are shown in *Dou et al.* [2017]; *Ajo-Franklin et al.* [2019b]; *Tribaldos et al.* [2021]. As for active-source implementations, examples include *Song et al.* [2018]; *Cole et al.* [2018].

For reflection seismic in surface deployment, field tests have been very limited due to the low sensitivity of the fibre to broadside waves [*Kuvshinov*, 2016]. An indirect approach for obtaining surface recordings of seismic data with DAS was implemented by *Bakulin et al.* [2017]; their approach involved obtaining reflection data by using multiple shallow upholes. A more direct way to obtain reflection data is to install helically wound fibres near the surface and in a horizontal borehole [*Hornman*, 2017; *Urosevic et al.*, 2018; *Spikes et al.*, 2019]. A more recent approach to enhance the broadside sensitivity is discussed in the work of *White et al.* [2022], where multiple fibre configurations and arrangements are used. For multi-component DAS measurements, theoretical models are proposed for the use of multi-helix configurations to retrieve the strain-tensor components [*Innanen*, 2017; *Ning and Sava*, 2018b].

In this chapter, we discuss a field experiment in which we examine the combined use of straight and helically wound fibre for land seismic measurements. Our focus is on the analysis of multi-mode information obtained from the combined use of straight and helically wound fibres as well as assessing the usefulness of their combined use for reflection seismic.

The chapter is structured as follows. In the introduction, we will describe the principles of DAS, how it relates to geophone data, and how it can be modelled. This is followed by describing the field experiment with the set-up and fibre configurations. The obtained results are shown and compared to each other, compared to geophone data and our interpretations are supported by modelling. Some open points are then discussed and finally the conclusions are given.

■ 4.1.1 Distributed Acoustic Sensing: what does it measure?

A DAS system consists of an interrogation unit, also called an interrogator, and an optical fibre, one of its ends being connected to the interrogator. It is based on the principle of Optical Time Domain Reflectometry (OTDR) where the sensing fibre is injected with a light pulse/signal. As the light propagates and is guided through the fibre, it encounters randomly distributed inhomogeneities infused in the fibre material and it is scattered via the Rayleigh-scattering mechanism, which is an elastic scattering process meaning that the frequency of the incident light and the scattered light is the same. Please refer to the section 1.2.3 for more information on scattering in optical fibres. Only back-scattered light is then captured by a photodetector in the interrogator and the phase information of the light is obtained (see Figure 1.5).

That relative change of distance, i.e. $\varepsilon_{xx} = (x + \delta x)/x$ due to the elastic deformation of the fibre, is proportional to the phase difference $\Delta\Phi$ of the back-scattered signal with the following relationship [*Lindsey et al.*, 2020]:

$$\Delta\Phi = \frac{4\pi n L_g \xi}{\lambda} \left(\frac{x + \delta x}{x} \right), \tag{4.1.1}$$

where n is the refractive index of the fibre material, L_g is the length over which the strain is determined, the so-called gauge length, ξ is a scalar factor accommodating the changes in the index of refraction due to stress and λ is the wavelength of the source. ξ values vary between 0.79 for pure silica [*Schroeder*, 1980] and 0.735 for GeO$_2$-doped fibres [*Bertholds and Dandliker*, 1988]. A typical value for n is 1.45 for a wavelength λ of 1550 nm [*Lindsey et al.*, 2020].

The majority of DAS systems extract the temporal change of the phase, i.e. $\partial_t (\Delta\Phi)$, and therefore the output of the DAS system will be the strain-rate instead of strain where $\partial_t (\varepsilon_{xx}) \propto \partial_t (\Delta\Phi)$. Several methods are used to retrieve $\Delta\Phi$, or its time-derivative; these include interferometric approaches using a single pulse [*Posey et al.*, 2000; *Masoudi and Newson*, 2017b; *Farhadiroushan*, 2010], a dual-pulse approach [*Dakin and Lamb*, 1990] and heterodyne approach [*Hartog and Kader*, 2012]. More recent advances in DAS include the use of a chirp pulse as a source to allow long-range measurements of as much as 171 km [*Waagaard et al.*, 2021].

Gauge length, noise floor and pulse repetition frequency

Several factors should be taken into consideration to measure the desirable seismic response. Here, we consider the most relevant factors that affect the DAS measurement. The first and most important one is the gauge length L_g. L_g is the length over which the strain ε_{xx} is calculated, as shown in equation 4.1.1. So, ε_{xx} is an average strain along L_g. Two factors determine a suitable gauge length [*Dean et al.*, 2017], namely sampling the seismic wavefield densely and having a sufficient S/N ratio. For DAS measurement, there is a trade-off between choosing a small gauge length to sample the wavefield densely and decreasing the S/N ratio. The choice is therefore a compromise. Another factor affecting the quality of the DAS measurement is the pulse repetition frequency (PRF) of the light source. To minimize

the noise/error coming from the phase-unwrapping process, hence decreasing the noise floor, the PRF should be as high as possible but up to a certain maximum PRF_{max} to avoid overlapping with subsequent pulses. The limit PRF_{max}, as shown in *Fernández-Ruiz et al.* [2019], can be expressed as

$$\text{PRF}_{max} = \frac{c}{2n_g L}, \tag{4.1.2}$$

where c is the speed of light in vacuum, n_g is the group refractive index, and L is the total length of the fibre in meters. The amount of self-noise in the system coming from the system components is another factor affecting the S/N ratio.

Sensitivity of straight and helically wound fibres

An intrinsic issue with DAS is that it is based on the elongation and contraction in the direction of the optical fibre. When a strain is applied at an angle θ to that fibre, a strain sensor shows a $\cos^2 \theta$-amplitude dependency, as shown by *Benioff* [1935]. So also in response to a P-wave propagating with angle θ to the fibre, such a dependency is present. This means that there is a decreased sensitivity to broadside waves. This is especially relevant in the context of surface seismic if the aim is to measure reflections; this decreased sensitivity may make it difficult to record them on horizontally surface-deployed optical fibre cables. This is unlike DAS in borehole applications like Vertical Seismic Profiling (VSP) where the reflected upgoing P-wavefield will have a propagation angle almost parallel to the fibre's axis (i.e. $\theta \to 0$).

To enhance the broadside sensitivity for surface-deployed cables, fibre shaping to a helix was introduced [*Den Boer et al.*, 2012; *Kuvshinov*, 2016; *Hornman*, 2017], commonly known as a helically wound fibre (HWF). An illustration of the HWF is shown in Figure 4.1a with two wrapping angles α of 60° and 30° which are used in this study. Theoretically, *Kuvshinov* [2016] shows how the wrapping angle α affects the response to P-waves, S-waves and surface waves. One outcome was that shaping the fibre into a helix will decrease its sensitivity to surface waves as well as enhance the fibre's sensitivity to broadside P-wave reflections.

Modelling helically wound fibre

To model the helically wound fibre response, we first start by explaining how DAS measurements are related to geophone responses (i.e. particle-velocity measurements). DAS measurements can be equivalently represented as an estimate of the strain rate, i.e. $\dot{\varepsilon}_{xx} = \partial_t (\partial_x u_x)$, where u_x is the displacement, or as the spatial derivative in x of the x-component of the particle-velocity, i.e. $\partial_x (\partial_t u_x) = \partial_x V_x$. We use the latter representation for our modelling. A 2D elastic finite-difference modelling program [*Thorbecke and Draganov*, 2011] will be used to estimate the velocity components and their spatial derivatives.

In the modelling, only the wrapping angle effect of the fibre is taken into account, and the mechanical properties of the fibre and the embedding cables are not included, thereby assuming the fibre and the embedding cable have the same properties as the surrounding soils/rocks. In order to calculate the response of a helically wound

fibre, we adapted the approach from *Baird* [2020] but used the spatial derivative of the velocity as the strain rate. So for a single helix with a wrapping angle of α, the measured response will be:

$$\dot{\varepsilon}_{HWF} = \partial_x V_x \sin^2 \alpha + 0.5\, \partial_y V_y \cos^2 \alpha + 0.5\, \partial_z V_z \cos^2 \alpha. \qquad (4.1.3)$$

As we are using a 2D elastic finite-difference scheme, expression 4.1.3 is adapted to be

$$\dot{\varepsilon}_{HWF} = \partial_x V_x \sin^2 \alpha + \partial_z V_z \cos^2 \alpha. \qquad (4.1.4)$$

We can see from this equation that for a straight fibre $\alpha = 90°$ and the measured strain will become the one of a straight fibre, i.e. $\dot{\varepsilon}_{SF} = \partial_x V_x$. We can combine the measurements of a straight and a helically wound fibre as:

$$\begin{pmatrix} \dot{\varepsilon}_{SF} \\ \dot{\varepsilon}_{HWF} \end{pmatrix} = \begin{pmatrix} 1 & 0 \\ \sin^2 \alpha & \cos^2 \alpha \end{pmatrix} \begin{pmatrix} \dot{\varepsilon}_{xx} \\ \dot{\varepsilon}_{zz} \end{pmatrix}. \qquad (4.1.5)$$

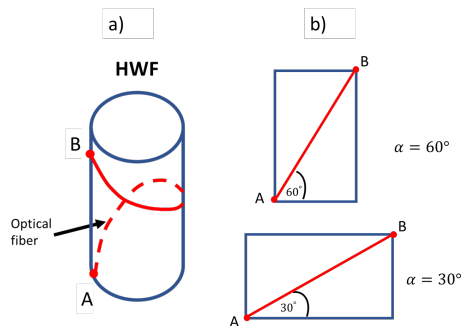In this study, we will be using this approach to compute the responses.

Figure 4.1: *Illustration of the HWF: a) A helical fibre wrapped between point A and B. b) Unwrapped fibre with two wrapping angles (i.e. $\alpha = 60°$ and $\alpha = 30°$). Adapted from Kuvshinov [2016].*

4.2   Field set-up

A field experiment was planned and carried out with the aim to see whether reflections could be recorded on surface-deployed optical-fibre cables, and also to see whether a combination of HWF and SF measurements would provide extra information, such as type of motion and type of waves. The field experiment took place on farmland in the province of Groningen, in the north of The Netherlands. A schematic showing the shooting line, geophone line and buried fibre cables is illustrated in Figure 4.2a. The different optical fibres are connected via fusion splicing into two long fibres, as will be described later on. The interrogators were located in

the farmer's shed and connected to the buried cables via a standard single-mode-fibre surface cable of 1 km. Figure 4.2b shows the fibre's connection box that is used to check and resolve issues related to connections of the fibres (e.g. bad splices) and tap testing.
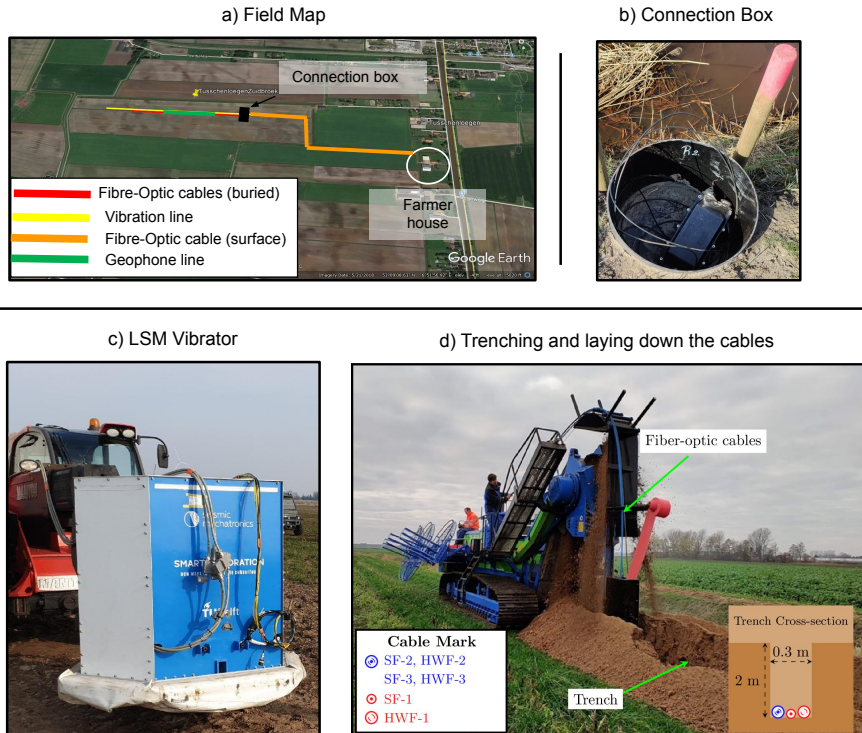

Figure 4.2: *Field experiment set-up and components: a) Field map with the position of fibre cables (surface and buried), geophone line and vibration line, i.e. shot positions (survey location: 53° 9'16.12"N, 6° 50'53.99"E), b) Connection box with terminations and splices of cables, c) Electrically driven seismic vibrator, based on Linear Motor Technology and d) Trenching and burying fibre-optic cables.*

The topsoil is mostly composed of clays, peat and some thin sand layers. A shallow borehole next to the buried cable was drilled and P-wave and S-wave logging tools were used to measure the compressional (V_p) and shear (V_s) velocities down to around 80 m depth. These logs are shown in Figure 4.3. It can be observed in the figure that the near-surface down to 80 m varies for the most part around 1600-1800 m/s for V_p and 300-400 m/s for V_s except the layer between 10-20 m where velocities drop to around 1500 m/s and 160 m/s for V_p and V_s, respectively. Simplified velocity models based on the logs are plotted as dashed lines in Figure 4.3, which will later be used for modelling synthetic seismograms.

The cables are intended for continuous-passive and active time-lapse measurements and were buried 2 m deep, most of the year being below the water table. The cables were laid down by a trenching machine, commonly used for laying out drainage pipes but in this case adapted for our cables, as shown in Figure 4.2d. At the time of trenching, we could see that around 2 m depth the soil was quite sandy compared to the clayey/peaty topsoil, which should give us good coupling. After the cables were laid down in the trench, they were directly covered with the extracted soil by the same machine and afterward well-compacted by a separate excavator.

The source used is an electrically driven seismic vibrator, based on the technology of linear synchronous motors [*Noorlandt et al.*, 2015]; it is shown in Figure 4.2c. As source sweep, an upsweep of 2-180 Hz with a duration of 12 s was used, with an (extra) listening time of 3 s. As for source position, we shot every 2 m for a 750 m shooting line (see Figure 4.2a). We opted for such a dense spatial source sampling with the aim to satisfy the spatial Nyquist sampling criterion in common-receiver gathers as well as to create a high-fold image. A number of 2 shots per position was used for vertical stacking.
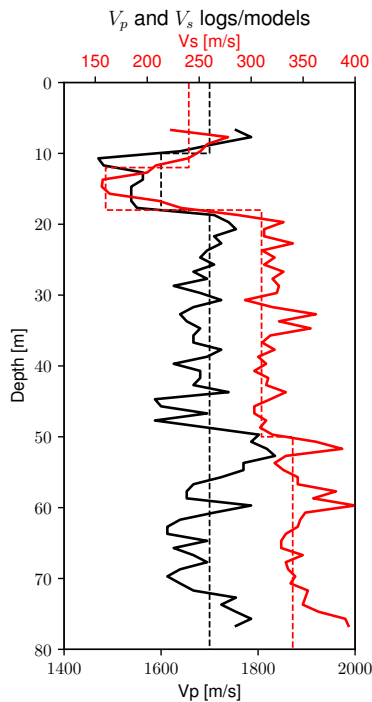

Figure 4.3: *P-wave and S-wave velocity logs (solid lines) of the near-surface and models (dashed lines) used for synthetics.*

Interrogator systems and fibre-optic cables

In this field experiment, we have used two DAS interrogators, namely FEBUS A1-R and iDAS^{TM} v3. We will denote the FEBUS A1-R system as DAS-Standard and the iDAS v3 system as DAS-Engineered for the rest of the chapter. DAS-Standard is connected to the conventional single-mode (SM) fibre and DAS-Engineered is connected to the engineered (i.e. Constellation^{TM}) fibre. It is important to note here that comparing the different DAS units is not the intent of this study, therefore, no direct comparison on the performance of the systems is presented. On DAS-Standard, the buried cables contain the following fibres (see Figure 4.4a): SF-1, HWF-1 (30°), SF-2 and HWF-2 (60°). SF-1 and HWF-1 are in separate cables, whereas SF-2 and HWF-2 are contained in the same cable. The order of fibres as shown in Figure 4.4a is chosen in a way to minimize optical reflections caused by splices between fibres with different core radii. As for DAS-Engineered, they are connected to Constellation^{TM} fibres SF-3 and HWF-3 (60°) (see Figure 4.4b). Note that fibres SF-2, HWF-2, SF-3, and HWF-3 are all contained in the same cable.

DAS-recording configuration

A DAS recording is a more elaborate process to configure than a geophone recording, as it depends on the length of the fibre as well as the amount of optical loss in the fibre. Each DAS unit was configured separately to have the desired data quality. Information about the acquisition parameters used for DAS is contained in Table 4.1. The most important parameter to note here is the gauge length L_g, which was chosen to be 2 m for both systems. Note that even though larger gauge lengths, e.g. 10 m, are expected to give a better signal-to-noise ratio [*Dean et al.*, 2017], our interest was to have proper (Nyquist) sampling of the surface waves to avoid spatial aliasing of the total-wavefield recordings.

Table 4.1: *DAS systems and fibre configurations. (PRF = Pulse Repetition Frequency)*

	DAS-Standard	**DAS-Engineered**
Gauge length [m]	2	2
Output spatial sampling [m]	1	1
Fibre type	Conventional SM	Engineered SM
Total length [m]	3300	2000
Trenched length [m]	2080	970
PRF [kHz]	10	16
Fibre segments	SF-1, HWF-1, SF-2, HWF-2	SF-3, HWF-3

a) Conventional Fiber

Non-reflective
End

Fusion-splice

HWF-1 (30°); 740 m

SF-1; 370 m

HWF-2 (60°); 520 m

SF-2; 450 m

Lead-in
Surface
Fiber
(1000m)

b) Engineered Fiber

DAS-Standard

HWF-3 (60°); 520 m

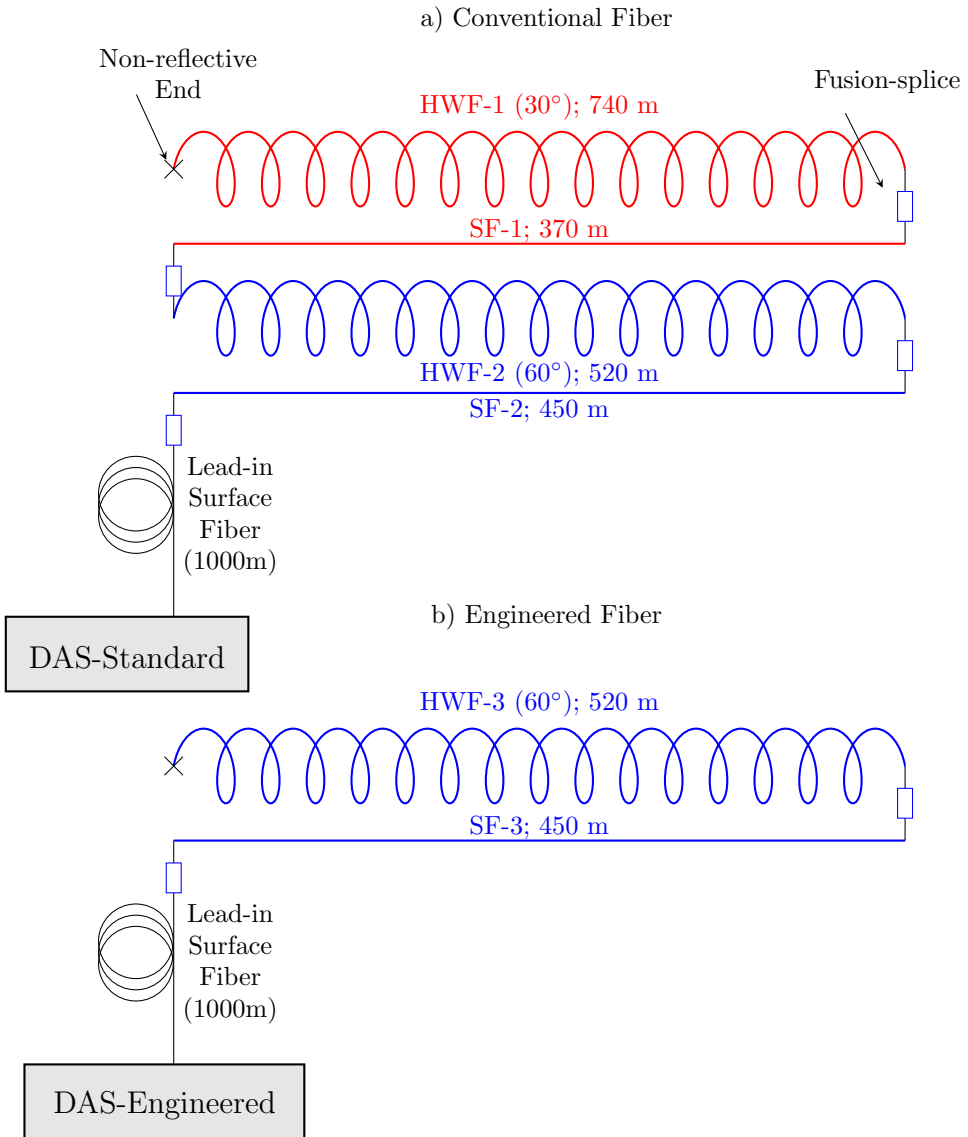SF-3; 450 m

Lead-in
Surface
Fiber
(1000m)

DAS-Engineered

Figure 4.4: *DAS systems and fibre configurations; a) DAS-Standard system connected to conventional fibres and b) DAS-Engineered system connected to engineered fibre.*

Multi-component geophones

A portion of the fibre-optic receiver line was also covered with surface-deployed three-component geophones over a length of 80 m with a spacing of 2 m. For our analysis, we used the horizontal in-line (H_1) the vertical (V_3) components of the geophones for our comparisons since the former is linked to the strain direction of the straight fibres and the combination of these two components to the signal measured by helically wound fibres. The symbols H_1 and V_3 are used to refer to the components of geophones to distinguish them from the synthetically modelled horizontal (V_x) and vertical (V_z) components of the velocity. While deploying the geophones, we made sure that they were correctly oriented and properly coupled to the ground.

4.3 Data processing

A raw measurement included the whole length of the fibre, so different fibre configurations were looped in one long stretch. The raw DAS-Standard and DAS-Engineered data are first down-sampled from 10 kHz and 16 kHz, corresponding to their PRF respectively, to a sampling frequency of 500 Hz. Then, the data are correlated with the ground force of the seismic vibrator estimated from several shots. An example of a single correlated shot record is shown in Figure 4.5. The beginning of the trench where the fibre gets buried is taken as position 0 m and the fibre before that position corresponds to the surface (extension) cable. The different cables are easily identifiable on the record, as marked by the different coloured rectangles below the seismograms, where the white-colour rectangles correspond to extra fibres used for connecting the different fibres via fusion splicing. Figure 4.5 also shows the spectral content of the shot record. Via red arrows, we mark some notable noise sources showing some common-frequency modes.

Before the survey took place, the fibres were checked with an OTDR device that shows the losses and possible faults along the line. Combining these measurements with the raw data themselves, we were able to separate the different parts of the cables into different data sets with minimal uncertainty in the positions. It is hard to exactly calibrate the distance along the fibre as the spatial resolution is limited by the spatial sampling as well as the gauge length of choice. With our data, the uncertainty in position is estimated at ± 1 m.

Next, processing took place for each data set and the steps are described in the following. We kept the processing quite minimal on purpose as we wanted to minimize processing artifacts. The whole processing flow is shown in Figure 4.6. The geometry is set, and vertical stacking is done via a diversity stack. Several noise-removal methods were applied to the data including a trapezoid bandpass filter with corner frequencies 30/40 and 100/120 Hz, FK filter and bottom muting to remove the ground roll as well as some random noise. The data are then sorted into CMP gathers and corrected for NMO with a constant velocity of 1700 m/s, which was determined via the vertical-component geophone data that showed clear P-wave reflections. Finally, a CMP stack is constructed using RMS-normalization of each trace before stacking.
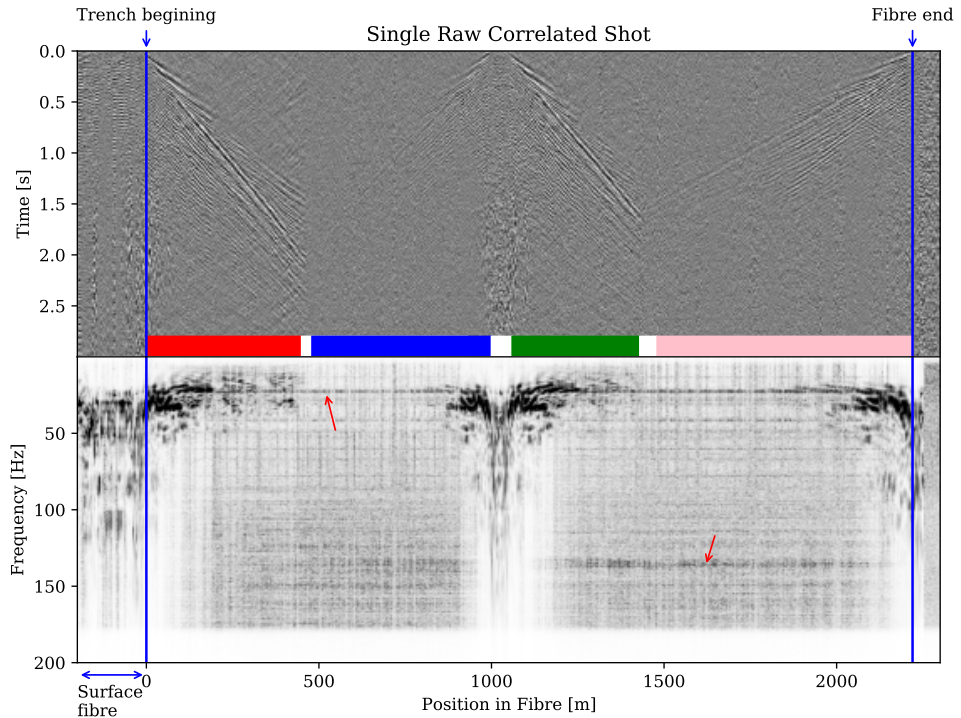
Figure 4.5: *Correlated single raw shot of DAS-Standard system in time-distance (top) and frequency-distance domain (bottom). Portions of fibre coloured in red, blue, green and pink correspond to fibres SF-2, HWF-2, SF-1 and HWF-1, respectively; white portions are splices.*

4.4   Results

In this section, we analyze the pre-stack data, via common-shot and common-receiver gathers, and post-stack data, via CMP stacks. In the pre-stack domain amplitude and polarity effects in the straight and helically wound fibres are studied, together with reflections observable in these pre-stack data. In the post-stack domain, the results of imaged reflections are discussed.
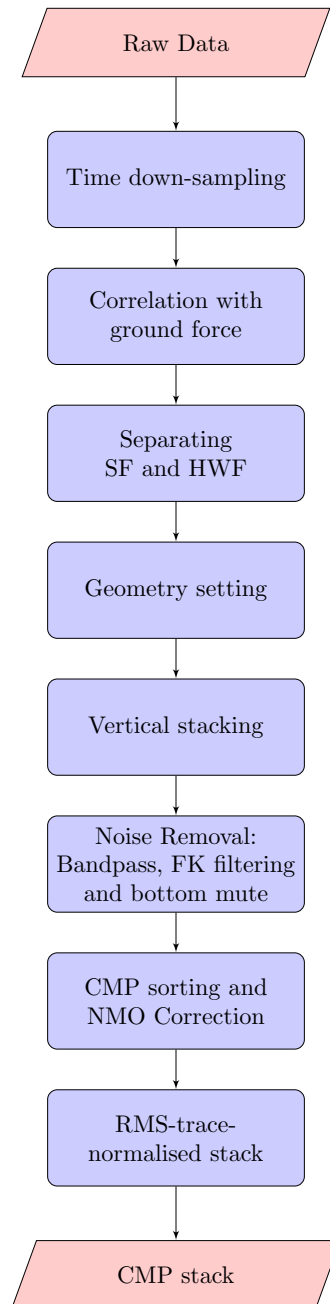
Figure 4.6: *Processing flow to produce a CMP stack.*

■ 4.4.1   Analysis of pre-stack data

Horizontal component of geophone vs. straight fibre DAS

Here we discuss the comparison in the surface-wave signal between the horizontal-component geophone (H_1) and the straight-fibre data using a common-receiver gather at 400 m and compared to synthetic shots. The synthetics are modelled using a vertical-force source shot at position 400 m with a 1.5D medium based on the velocity models shown in Figure 4.3. The density is assumed to be constant with a value of 2000 kg/m^3. The source wavelet is a Ricker wavelet with a dominant frequency of 8 Hz. All gathers are filtered with a trapezoid bandpass filter with corner frequencies of 2/4 and 8/10 Hz.

As shown in Figure 4.7a and 4.7b, we can see that the SF data is not sensitive to the direction of motion, unlike the horizontal geophones, where the polarity is reversed going from the negative to the positive offsets. This is expected based on the synthetic examples of the modelled V_x and $\partial_x V_x$ (see Figures 4.7c and d) which agree with recorded geophone and SF data, respectively.
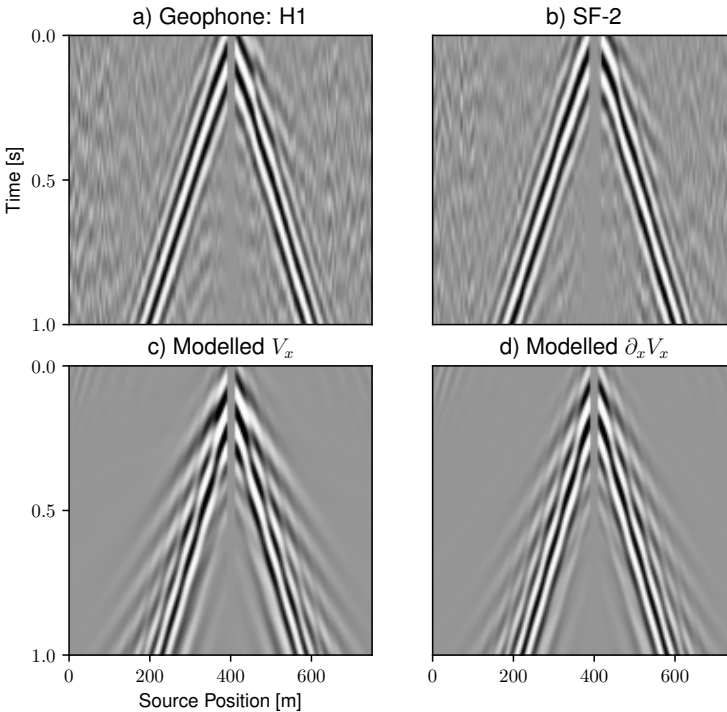

Figure 4.7: *Common-receiver gathers at 400 m; recorded geophone H_1 (a), recorded SF-2 (b), modelled V_x (c), modelled $\partial_x V_x$(d).*

Response to different fibre geometry

First, we consider the amplitude differences between the different cables for one receiver position, in this case, 400 m, for all shots. This is shown in Figure 4.8. When considering the RMS values at that receiver position: even with SF-1 being in a separate (steel-armored) cable and SF-2 being part of a cable that includes both straight and helically wound fibres, the difference in amplitude is minute. This indicates that the cable configuration and its material do not play a significant role in the case of straight fibre. When the properties of the cable are similar to the ones of the ground around it [*Kuvshinov*, 2016; *Baird*, 2020], this can be expected, but it can here be observed that the cable design also does not affect the results. On the other hand, when we compare the amplitudes between SFs and HWFs, the difference is significant as there is an increase of 10-12 dB in favour of the straight fibre as shown in Figure 4.8.
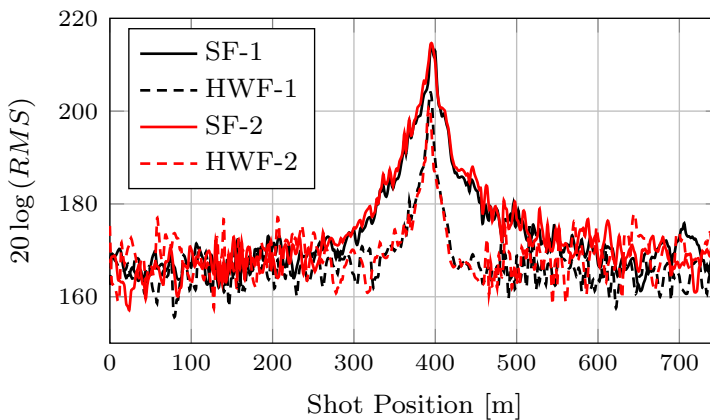

Figure 4.8: *RMS amplitudes of Common Receiver Gather at 400 m of four different fibre sections connected to the DAS-Standard system.*

When looking at the spectra for the different fibre configurations, as shown in Figure 4.9, it can be observed that the main differences between SF and HWF occur in the frequency band of some 2-55 Hz, being highlighted in that figure. For data from the area under consideration, this is typically the frequency band of the surface waves and S-waves. As *Baird* [2020] noted, an HWF configuration is destructive for S-waves, and therefore also for that component of the surface waves, and here, this is confirmed by our observations. The helical shape acts as a (damping) filter for the surface waves and S-waves. In the band above some 55 Hz, where the information is mainly of P-wave nature (e.g., reflections and head waves), the amplitudes are comparable between the SF and HWF, suggesting that both geometries preserve P-wave information, with a note that these amplitudes are *not* enhanced by the HWF configuration, although this would be expected for P-wave reflections.
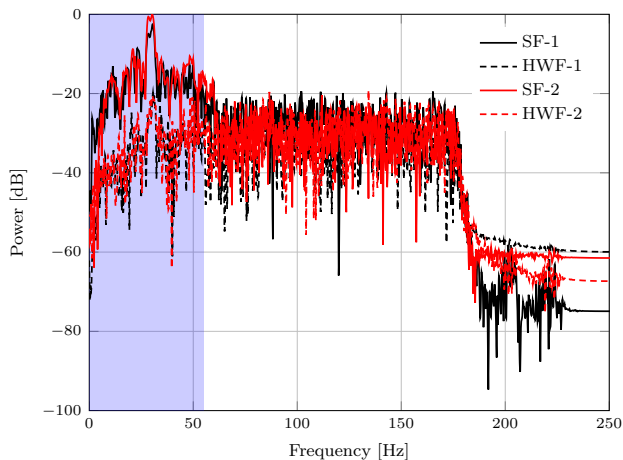
Figure 4.9: *Power spectra of portion inside the surface-wave cone of CRG at 400 m (shot positions: 328-336 m) for different fibre configurations. Band 2-55 Hz is highlighted to indicate the main differences between HWF and SF amplitudes.*

Another type of observation that can be made on the common-receiver gather is the change in phase that can be observed in the surface-wave cone. Figure 4.10 shows the same common-receiver gather (CRG) for the different fibres. We can see that the straight fibre SF-1 and SF-2 give comparable results, as expected. However, a change in the polarity of the main surface-wave event around 0.4 s can be observed in the HWF-1 and HWF-2 configurations. This can be attributed to the difference in the wrapping angle. We can see that for HWF-1 ($\alpha = 30°$), the polarity is flipped when compared to the straight-fibre signal but with lower amplitude, whereas the polarity is the same for the HWF-2 ($\alpha = 60°$) as marked by the red dashed line in Figure 4.10b.

To explain this difference in both amplitude and polarity between the SFs and HWFs, we model their response based on equation 4.1.5 with a simple model shown in Figure 4.3. The responses are shown in Figure 4.11a. Similarly to what was shown in the measured data, we can see an agreement in the changes in polarity and amplitude. The polarity of straight fibre (i.e. Figure 4.11b) is the same as HWF-2 ($\alpha = 60°$), and it is flipped in HWF-1 ($\alpha = 30°$) as observed in the measured data. This can be explained by equation 4.1.4 where a larger value of $\alpha = 60°$ will increase the contribution of $\partial_x V_x$, and will decrease the contribution of $\partial_z V_z$. Also, as shown in Figure 4.11c, we can see that there is a difference of some 8-10 dB between the straight and helically wound fibres which is close to the measured difference of 10-12 dB as shown in Figure 4.8. Therefore we attribute the difference in amplitude to the higher sensitivity of the straight fibre to the horizontal component and the lower sensitivity of the vertical component of the surface waves and possible S-waves.
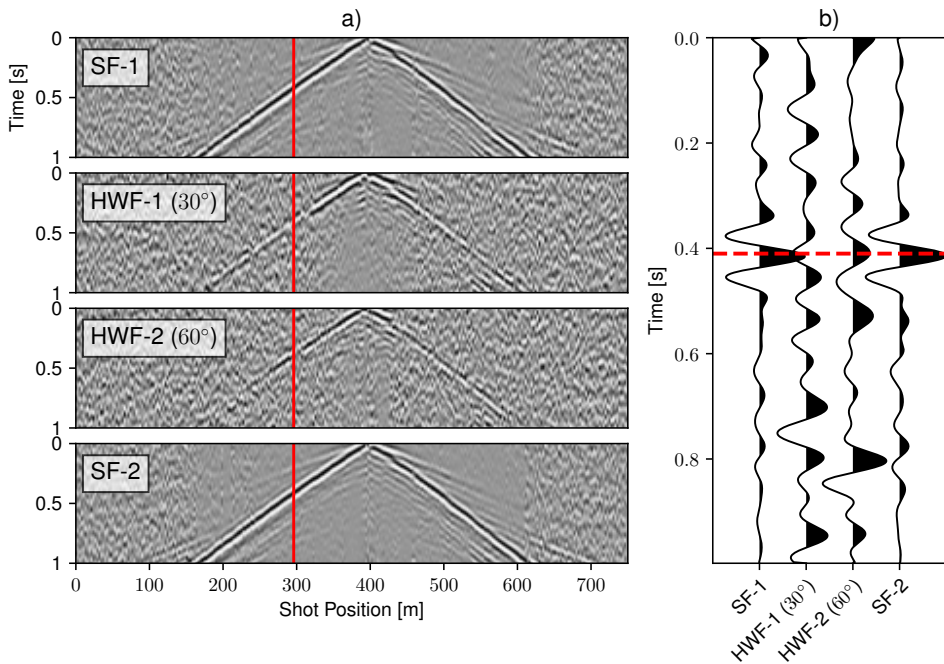
Figure 4.10: *a) Recorded common receiver gathers at 400 m of fibres: SF-1, HWF-1, HWF-2 and SF-2. b) Traces at shot position 298 m (marked by the red line in a) showing a comparison of signals from the same offset for the different fibre configurations.*

■ 4.4.2   Reflections in engineered-fibre recordings

Reflections in pre-stack data

Here we analyze the data collected by the DAS-Engineered unit connected to the engineered fibre since those data were the best for this purpose. Figures 4.12a and 4.12b show three common-shot gathers of each fibre type at source positions (Sx) 0 m, 10 m and 20 m. For display purposes, the gathers are RMS-normalized and displayed using the same colourmap range.

The first thing we can observe is that the amplitude is higher in SF-3 than in HWF-3. In Figure 4.12c, we look at the RMS values for the time before 0.1 s (marked by the red dashed line in Figures 4.12a and 4.12b). We see that SF-3 has a higher amplitude overall, as well as higher amplitude variation around the mean RMS value, compared to HWF-3. Despite SF-3 having a higher amplitude in the early noisy arrivals, we can see the reflections (between the yellow dashed line) more clearly in the SF-3 data. Another observation in the HWF data is the horizontal events/stripes across the whole records that might be attributed to interrogator noise as the signal level picked by HWF is considerably lower than SF.
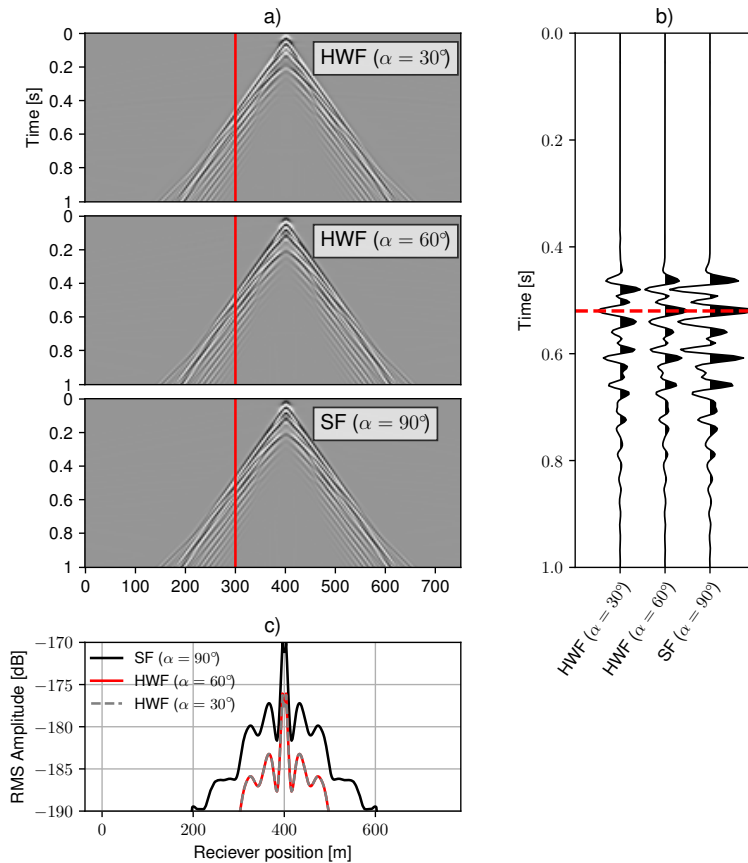
Figure 4.11: *a) Modeled surface-wave responses of straight and helically wound fibres with angles and their respective RMS amplitude (c). b) Traces at receiver 300 m (highlighted by the red line in a) showing a comparison between the signals of fibres with different wrapping angles.*
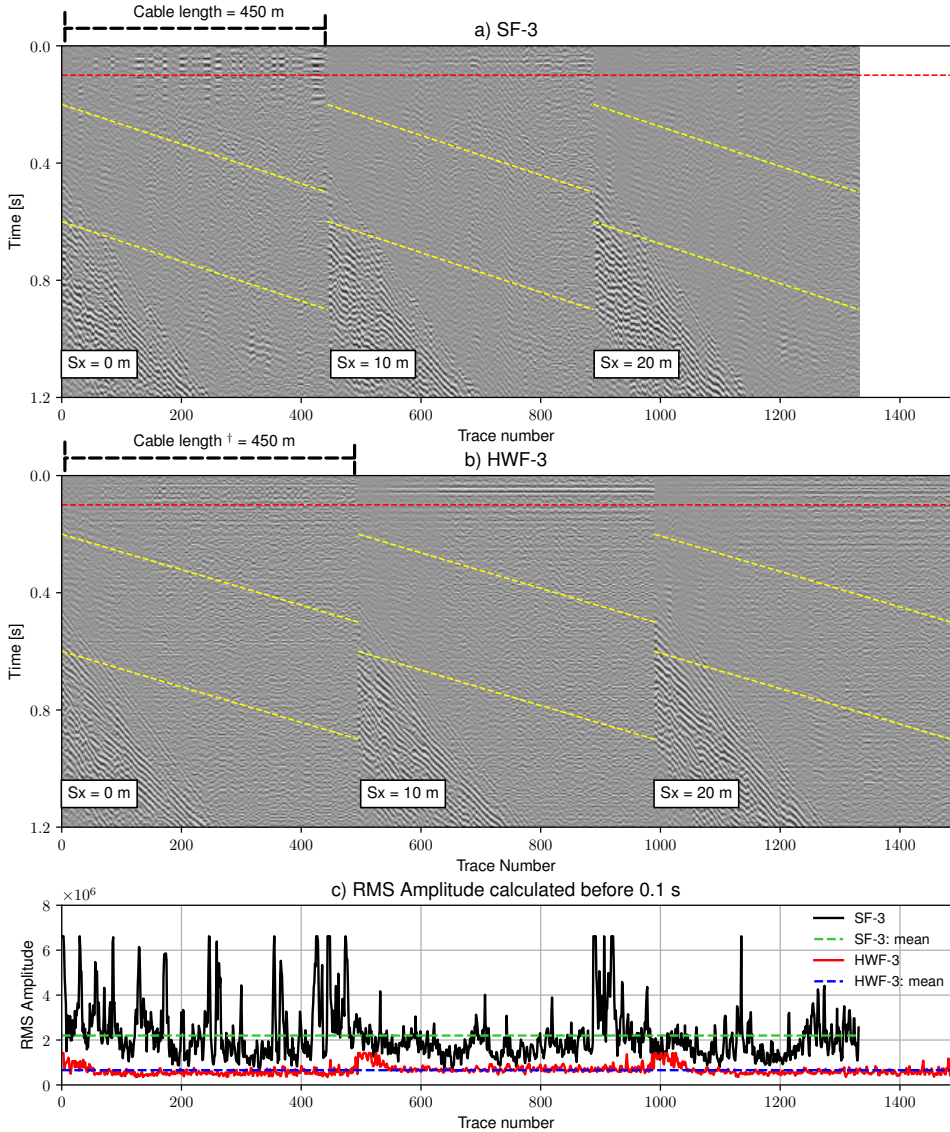
Figure 4.12: *Common-shot gathers at positions 0, 10 and 20 m for SF-3 (a) and HWF-3(b), and c) RMS amplitude calculated before 0.1 s.* [†] *Cable length $\neq$ fibre length.*

Now we look at the reflections in a common-receiver gather where the reflections seem to be more coherent. Figures 4.13a and 4.13b show a CRG at 173 m for the straight and helically wound fibre, respectively. As for reflections, we can see three major reflection packages highlighted by the red, yellow and green boxes. When considering the shallow reflections as highlighted by the red box: they are better discernible in the SF-3 than in the HWF-3 data. This is somewhat strange since it was expected that a straight fibre should be less sensitive to a broadside reflection than the helically wound fibre following *Kuvshinov* [2016]. The model described therein does not seem to match with what we observe in the field data.

When following one reflection tracked by the red dashed line in Figures 4.13a and 4.13b, we can see via Figure 4.13c that the absolute amplitude in SF-3 is roughly twice as high as the one in HWF-3. However, we also can see that deeper events as highlighted by the yellow box, are better discernible in HWF-3 despite the lower amplitude. Lastly, the events highlighted by the green box can be seen equally well in both fibre configurations, though we see some differences in the time domain and the frequency content that is shown by sharper events in HWF-3 compared to SF-3. Due to the steeper shape of the latter move-out indicating a lower RMS velocity, we interpret this event as a P-S reflection. Again, also these findings do not seem to be completely in agreement with the model of *Kuvshinov* [2016], where the model showed that the normalized strains should be higher in HWF for broadside reflections compared to SF for all propagation angles, but we see that we get higher amplitudes for SF in our measurements.

Modelling SF and HWF response to reflection

To model the reflections, we have adapted the near-surface velocity model in Figure 4.3 but added a reflector at 270 m, where the V_p and V_s below it are 2500 m/s and 1200 m/s, respectively. The source used for modelling the synthetics is a vertical force and the source wavelet is a Ricker wavelet with a dominant frequency of 20 Hz. The shots for the straight and helically wound fibre are modelled using eq. 4.1.5 and are shown in Figure 4.14a and 4.14b. We can see that the shot for the SF configuration shows a lower sensitivity to reflections as it mainly contains the horizontal component of the strain-rate tensor.

To analyze this further, we look at the reflections separately as shown in Figure 4.14a and 4.14b, and calculate the RMS amplitude for every trace at each offset, where windows of 40 ms around the reflection are highlighted by the dashed lines in the figures. We can see that the HWF ($\alpha = 60°$) shows a higher RMS amplitude for the reflection. We can see that for smaller offsets, where the reflected wave is almost vertical, the difference in amplitude is much larger, and for longer offsets, the differences get smaller (see Figure 4.14c).

This modelling exercise agrees with the model discussed by *Kuvshinov* [2016] in terms of HWF having a higher sensitivity to broadside waves, in this case, reflections. However, it is safe to say that this model does not explain the difference in RMS amplitude between SF and HWF observed for the reflections in the measured DAS data (see Figure 4.13).
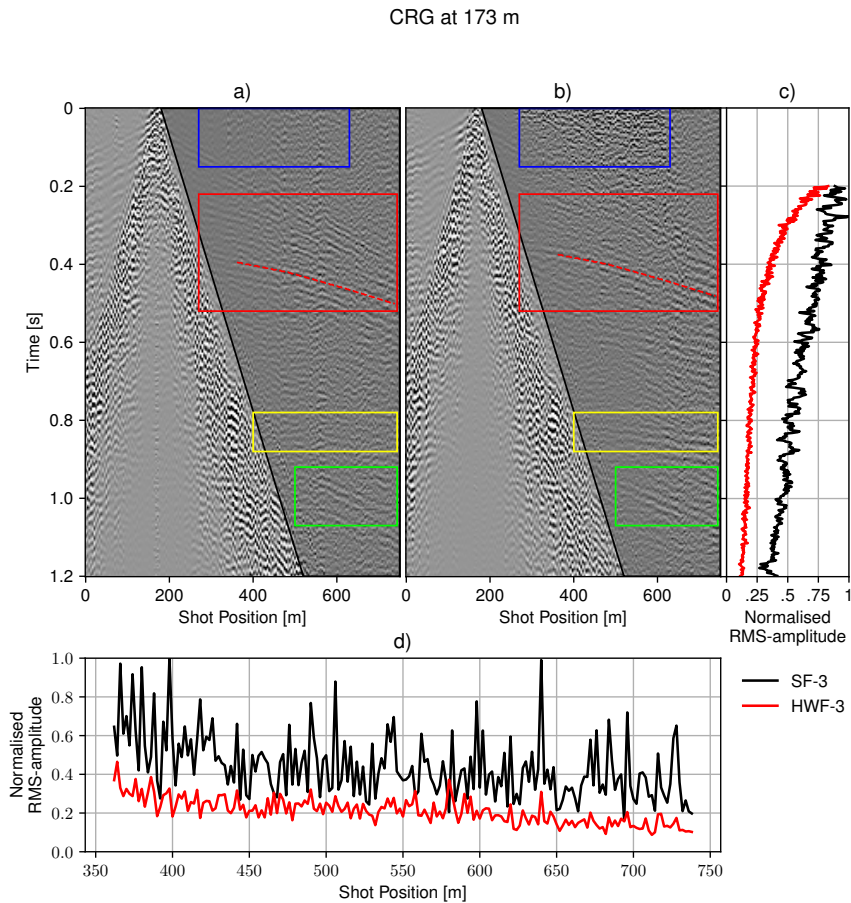
CRG at 173 m

Figure 4.13: *CRG at 173 m of a) SF-3 and b) HWF-3 and c) show normalized RMS ampli-tude as a function of time, calculated outside the surface-wave cone, as highlighted by the dark grey polygon. d) RMS values calculated along the reflection traced by the dashed red line within a 20 ms window. Normalized RMS-amplitude for SF-3 and HWF-3 calculated as: RMS(SF-3)/max(RMS(|SF-3|)) and RMS(HWF-3)/max(RMS(|SF-3|)), respectively.*

Reflections in CMP stack

We not only analyzed common-receiver gathers for the reflectivity information but also CMP stacks since they would show the quality of images that can be expected. With stacking of NMO-corrected CMP gathers the signal-to-noise ratio is improved substantially, especially because of the relatively high fold due to the small source and receiver spacings. Here we present the CMP stacks derived from the SF-3 and HWF-3 data since they gave the best-quality results.
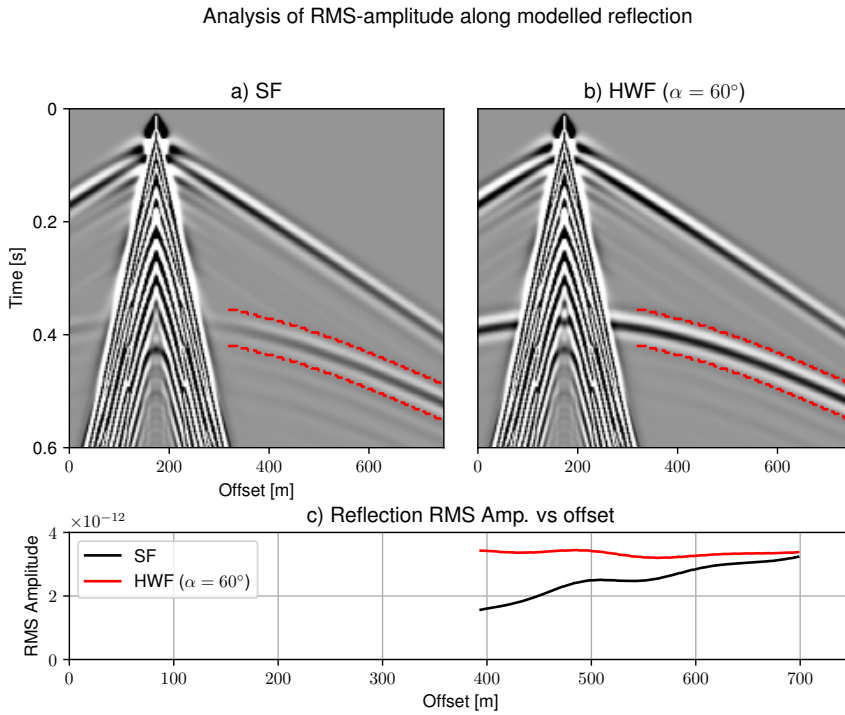
Analysis of RMS-amplitude along modelled reflection

Figure 4.14: *Modeled reflection responses and their RMS amplitudes: shots for SF (a) and HWF with wrapping angle of* $60°$ *(b). Dashed red lines highlight analysis windows of 40 ms to calculate RMS-amplitudes as a function of offset for the reflection in (c).*

First, we consider the images produced by SF-3 and HWF-3 as shown in Figure 4.15 using the whole fibre length as aperture. Again, it was expected that HWF-3 would produce the highest-quality result due to the broadside sensitivity, but this was not the case. For the shallow part, as highlighted by the red box, we can even see that SF-3 provides better continuity in the main reflection marked by the red arrow. Still, deeper events, as marked by the yellow arrow, are discernible in the HWF-3 result, unlike in the SF-3 one.

Another way to compare the stacks is to look at the differences using correlation. Traces of CMP numbers 165 to 580 from each stack are windowed, tapered and cross-correlated with each other. Then an average cross-correlation is calculated that is shown in Figure 4.15c. We can see that we have a minimum around $t = 0$ indicating that the stacks are out of phase, so they have opposite polarities as also shown in the waveforms in Figure 4.15d between 0.34 and 0.38 s.
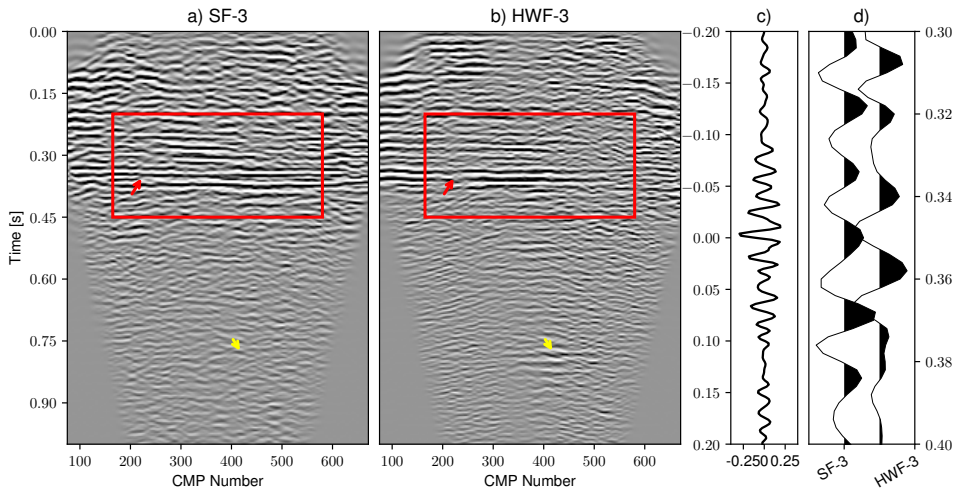
Figure 4.15: *CMP-stack comparison between a) SF-3 and b) HWF-3. c) Correlation function between SF-3 and HWF-3. The correlation trace in (c) is calculated from the tapered window of 0.2-0.45 seconds over the CMP range of 165-580. Traces of SF-3 and HWF-3 at CMP-325 (d)*

Second, we examine the continuity and presence of reflections in the SF-3 data using a comparable fold of coverage as the geophone data. Here only a portion of the fibre is used to create the stack since the same section as the geophone line was taken for comparisons. Next to that, the DAS-receiver line was decimated spatially to the same receiver spacing as for the 3C-geophone line. As for the HWF-3 stack using the same decimated receiver line, the results did not show the reflections, unlike with what we saw with the full-fold data shown in Figure 4.15. This comparison between SF-3 and geophone data is shown in Figures 4.16. Looking at the reference images obtained from the in-line horizontal and vertical components, V_3 give a significantly better reflection image (see Figures 4.16a and b), as expected since most of the reflected energy is nearly vertical. The horizontal geophones gave a worse reflection image since it is mainly sensitive to large(r) propagation angles of reflection. The V_3 image is taken as the reference image.

To compare the geophone data with our DAS measurements, we calculate the horizontal spatial derivatives of the horizontal-component geophone data (H_1) and vertical-component geophone data V_3 for every position using the expression:

$$\partial_x G = \frac{\Delta G}{\Delta x_G} = \frac{G_{i+1} - G_i}{\Delta x_G}. \tag{4.4.1}$$

where G stands for geophone, the index i for the spatial position, and it is noted that for our case Δx_G is equal to the gauge length L_g, i.e., 2 m.

The derived strain-rate responses are shown in Figures 4.16c and 4.16d next to the SF-3 shown in Figure 4.16e. We can see that despite the decreased broadside

sensitivity of SF-3, a reflection image can be obtained even though it is not as good as the one from the vertical geophones. For example, if we look at the reflection at 0.34 s, we can see that the reflection is flatter and more continuous in the $\partial_x V_3$ than in the SF-3. However, the same reflection is better retrieved by the SF-3 than by the horizontal in-line (H_1) geophone data in terms of its continuity. Also, shallow reflections are better shown in SF-3 data compared to the H_1 data, even though both are supposed to be mainly sensitive to the horizontal component.
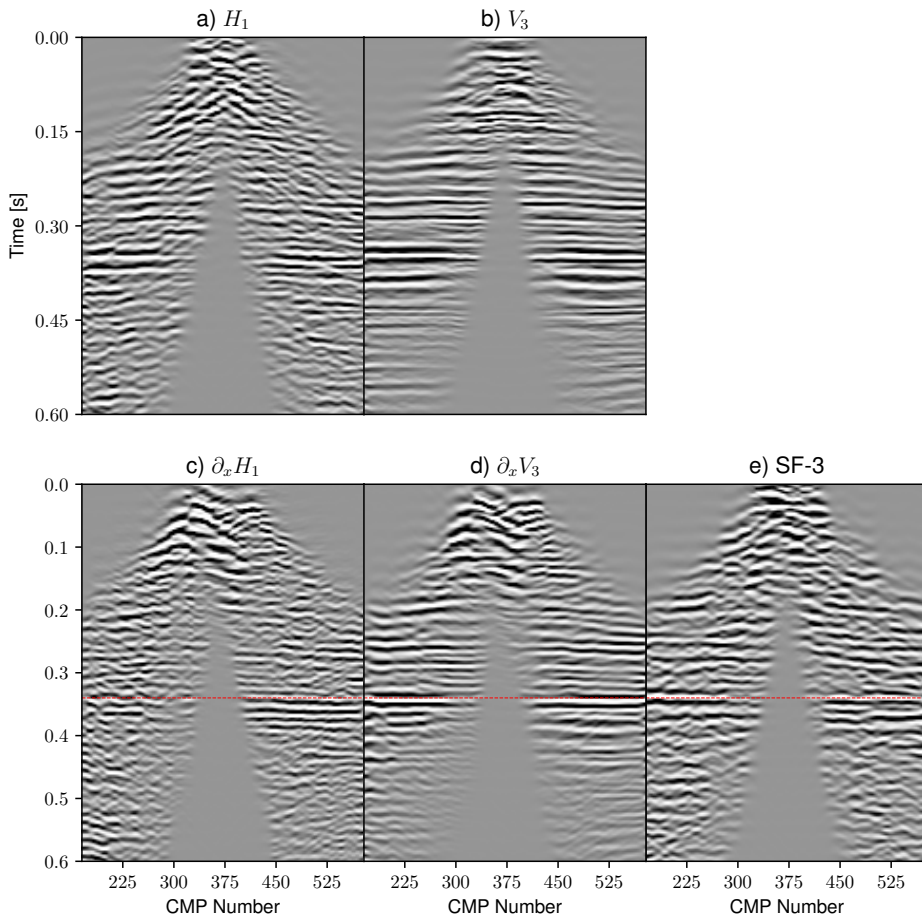

Figure 4.16: *CMP-stack sections for a) Geophone H_1, b) Geophone V_3, c) (strain-rate) $\partial_x H_1$, d) (strain-rate) $\partial_x V_3$, and e) SF-3. All images are RMS-normalized and displayed using the same colourmap limits.*

4.5   Discussion

Although we have shown via our field data that reflections are better discernible in SF than HWF data in the shallow part, DAS measurements are still lacking coherency compared to the geophone data. The reflectivity in this area is pretty good, also since the water table is very near the surface, which helped in detecting reflections. Good-quality systems like the iDAS-v3 system together with the engineered fibre are definitely needed but systems with a better signal-to-noise ratio would be even better.

Our data show that higher amplitudes are observed in the straight fibre. For surface waves, this is expected and can be modelled as we have shown. However, for P-wave reflections, the models of *Kuvshinov* [2016] and *Baird* [2020] are not in agreement with our measurements, where we saw that higher amplitudes in SF are observed in the reflection signal. We do not have a definite answer on why it is the case, however, we suspect that this might be related to the coupling of the fibre cable to the surrounding soil. The surrounding soil is very muddy and clayey with a low shear velocity of around 240-300 m/s and a P-wave velocity of around 1500-1600 m/s. Assuming this order of magnitude, our Poission's ratio is quite high (> 0.45). This is good news for SF as it transfers the strain into the horizontal fibre but at the same time negatively affects the HWF signal since for an impinging broadside wave, i.e. a reflection, the HWF is both shortened in the vertical direction and lengthened in the horizontal direction, decreasing its overall sensitivity. Although it is not exactly the same setting, a similar observation has been recently discussed by *Hendi et al.* [2023], where they modelled different scenarios of surrounding rocks and cementing conditions. They show that a helically wound fibre embedded in a soft formation/cement would give a decreased strain sensitivity compared to a hard formation/cement.

Another issue is that we used helically wound fibres but it was already suggested by *Den Boer et al.* [2012] that sinusoidally shaped fibres could be used to enhance directivity in a certain broadside direction even more, but this still poses challenges [*Al Hasani et al.*, 2020]. At the time of our field experiment, we were not able to have sinusoidally shaped fibres available for the measurements.

Furthermore, our results show that the combined use of helically wound and straight fibre could provide useful insight into the wavefield components. For reflection imaging, we saw that SF-3 showed better reflection continuity than HWF-3, while for deeper intervals, reflections are (better) discernible in the HWF-3 section. This observation could be exploited in a smart combination of these two data sets.

4.6   Conclusions

In this chapter, we examined the combined use of straight and helically wound fibres for land surface experiments. We conducted a field experiment in the Groningen area in The Netherlands and showed the behaviour of straight and helically wound fibres with different wrapping angles. We analyzed a typical common-receiver gather on its amplitude and some of its phase behaviour. We observed higher amplitudes

for surface-wave arrivals in straight-fibre data, in the typical frequency band of those waves, indicating and confirming that the HWF configuration is destructive to surface- and S-wave motion. It was also observed that the geometry of the cable design, such as cables with a separate (straight or helically wound) fibre or in an integrated fashion (with both straight and helically wound fibres in one cable) had little effect on the amplitude behaviour. We also confirmed, via analyzing our field data and a modelling exercise, that the wrapping angle can be such that the surface-wave arrival flips in its polarity. And also that helical winding dampens that signal as would be expected from modelling.

We saw on the field data that for reflection imaging of the engineered fibre data, the straight-fibre and the helically wound fibre data gave similar results. The pre-stack straight-fibre data showed reflection amplitudes of some factor 2 higher than the ones from the helically wound fibre, something that was not expected based on the theoretical models currently in use. In the CMP-stacked data, the straight-fibre section showed more coherent and continuous reflections in the shallow part, despite its decreased broadside sensitivity, while for the deeper reflected events, the helically wound fibre showed slightly better results but still with lower amplitudes. It was also found that the stacked SF and HWF data showed opposite polarities for the main reflections. Still, overall, the reflection images were comparable, in terms of capturing the main reflection events but with lower quality, to the one obtained from the horizontal derivative of the vertical-component geophone data.

5

Effects of gauge length and fibre geometry on active- and passive-source DAS data

Abstract   The dense spatial sampling that Distributed Acoustic Sensing (DAS) provides is an attractive prospect for broader adaptation for retrieving surface waves and its use for near-surface velocity imaging. Acquisition choices play a vital role in that. We examine two main factors here, namely the gauge length L_g and choice of fibre geometry (i.e. straight (SF) and helically wound fibres (HWF)) for active- and passive-source DAS data. Several observations are made including that longer L_g favour longer wavelengths and give higher signal amplitudes but introduce notches affecting shorter wavelengths. This in turn has an effect on higher modal information and sensitivity and resolution for shallower velocity variations. Also, we see more emphasis on the decreased sensitivity of HWF to surface waves – as also previously shown in the chapter 4 –, and we also show how we can go around that by use of longer L_g. Finally, using the passive data, we show more data examples of the decreased sensitivity of HWF to earthquakes using an induced earthquake record, and ambient noise sources using retrieved surface waves with interferometry.

5.1   Introduction

Induced earthquakes are affecting areas in the Groningen province due to the gas production activities that have been carried out for years in the area [*van Thienen-Visser and Breunese*, 2015]. In many parts of the area, the near-surface is composed of unconsolidated peat and clay, leading to amplifying the surface waves [*van Ginkel et al.*, 2019]. That in turn causes damage to houses and infrastructure. Therefore, understanding the near-surface properties is of prime interest. Conventional point sensors, e.g. geophones and accelerometers, provide accurate measurements of the ground motion, but they are usually deployed sparsely, making their use for local velocity imaging limited. Distributed Acoustic Sensing (DAS) could potentially be the answer for that as it is capable of providing spatially dense data [*Daley et al.*, 2013; *Hartog*, 2017; *Hornman*, 2017].

Having adequate spatial sampling is especially critical in recording surface waves that satisfy the Nyquist criterion, which in turn allows accurate local velocity imaging that is conventionally done using Multi-channel Analysis of Surface Wave (MASW) [*Park et al.*, 1999a, 2007]. Examples of its DAS implementations are presented by *Dou et al.* [2017]; *Cole et al.* [2018]; *Lancelle et al.* [2021]; *Vantassel et al.* [2022a]. As shown in *Dean et al.* [2017], along with the gauge length being one of the most important parameters in determining the signal-to-noise ratio of the data, it should be also suitable to record the wavelength of interest. Also, shaping the fibre into a helix will affect its sensitivity to the different types of waves [*Kuvshinov*, 2016; *Hornman*, 2017].

In this chapter, we examine the effect of the gauge length on the retrieval of surface waves from an active source using straight and helically wound fibres and how different wrapping angles would affect the measured response. After that, we will look at passive data acquired using straight and helically wound fibres. The active-source data used in this chapter are from the DAS data collected in Groningen utilising a combination of different configurations of the optical fibre including straight and helically wound fibres with different wrapping angles. More on the acquisition of these data can be found in chapter 4. As for the passive data, they are described separately later in the chapter.

5.2   Effects of gauge length on active-source DAS data

For near-surface seismic characterisation, a commonly used method is Multi-channel Analysis of Surface Wave (MASW) [*Park et al.*, 1999a, 2007], or Multi-Offset Phase Analysis (MOPA, *Dalkhani et al.* [2023]). These methods make use of the dispersion of Rayleigh or Love wave types to invert for the shear-wave velocity of the near-surface. Rayleigh waves roll in an elliptical retrograde fashion with a particle motion consisting of a horizontal component in the propagation direction of the surface wave and a vertical component. Love waves, on the other hand, contain one component in the horizontal plane, perpendicular to the propagation direction of the wave. In practice, to pick up Rayleigh-type surface waves, the vertical motion is commonly measured, via vertical geophones along with a vertical source. However, optical

fibres are mostly sensitive to axial motion meaning that if an optical fibre is deployed horizontally, it mostly senses the horizontal component of the Rayleigh-type surface wave.

What is gauge length?

A gauge length is a sensing unit. It is an integration length over which strain or strain rate is estimated. It is one of the most critical parameters in acquiring DAS measurements as the choice of its value should take into account velocity and frequency range of interest [*Dean et al.*, 2017]. Here we examine the effect of gauge length on the recording of surface waves which has closely similar effects as using arrays in standard seismic measurements. That is when a gauge length is used, the frequency-wavenumber response will show notches associated with the array length. Generally speaking, a longer gauge length gives a higher signal-to-noise ratio but has less lateral resolution; optimising this depends on the wavelengths of interest.

The channel spacing and gauge length

In seismic acquisition, the sensor spacing is a significant factor affecting the measured response. An undersampling of the wavefield will result in an aliased response. Therefore, having adequate sampling is crucial (see Figure 5.1). With conventional point sensors in land seismic settings, dense spatial sampling of the wavefield can be financially and practically challenging as it requires the deployment of single sensors at small distances. Therefore groups of sensors are often used to sample the reflected field sufficiently, where the group then also acts as a digital anti-alias filter of some of the noise, being mainly surface waves in land data [*Vermeer*, 1990]. Similar effects of the use of point-sensor groups apply to DAS but with slight differences as DAS fibres are continuous ("distributed") measurements along the gauge length and each channel is overlapping with the other, unlike the point-sensor groups that are partially overlapping or not overlapping at all. As the channel spacing is much smaller than the gauge length in DAS, its effect is not really an issue, and therefore ignored, i.e., it is kept fixed. Therefore, only the influence of the gauge length is investigated here in this chapter.

Wavenumber response of continuous gauge-length versus discrete point measurements

As DAS is a distributed measurement by nature, we can think of its effect as a summation of strain-rate measurements along the space domain. This mathematically can be described as the Fourier transform of a rectangular pulse of length L_g:

$$A(k_x) = \frac{1}{L_g} \frac{\sin(\pi k_x L_g)}{\pi k_x} = \mathrm{sinc}(\pi k_x L_g), \tag{5.2.1}$$

where k_x is the spatial frequency (horizontal wavenumber) and L_g is the gauge length. The expression 5.2.1 is adapted from *Dean et al.* [2017] but here the amplitude is normalised by L_g for the comparisons we want to make. To a certain extent, this closely resembles the effect of an array of point sensors where a group of traces

is added without changing the spatial sampling. This will act like a moving-average filter in space. The moving average has the following wavenumber response:

$$A(k_x) = \frac{1}{M} \frac{\sin(\pi M k_x \Delta x)}{\sin(\pi k_x \Delta x)}, \tag{5.2.2}$$

where Δx is the sampling distance between the points and M is the number of points used for the moving average. Figure 5.2 shows the wavenumber response for a gauge length of 2 and 10 m, as well as for a moving average corresponding to distances of 2 and 10 m. We can see that the response will have a low-wavenumber bias with both, as well as notches in the wavenumber domain. These notches happen every $k_x = n/L_g$ or $k_x = n/(m\Delta x)$, where n and m are integer numbers. We see that the two responses closely resemble each other with a slight deviation at higher wavenumber values. In our modelling, we will be using spatial moving averaging to simulate longer gauge lengths to compare the synthetic responses with the measured DAS data.
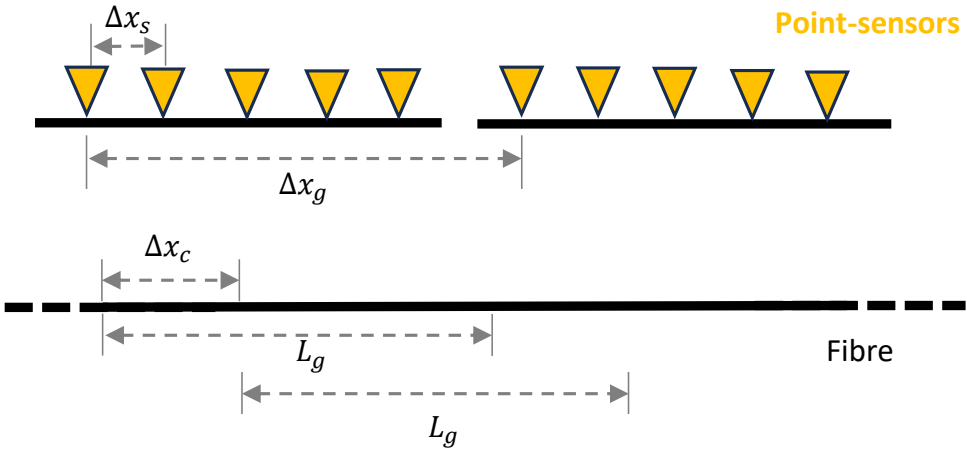
Figure 5.1: *Illustration of the gauge length Lg and channel spacing Δx_c for continuous/distributed measurements, and equivalent group spacing Δx_g and sensor spacing Δx_s for point measurements (like geophones).*
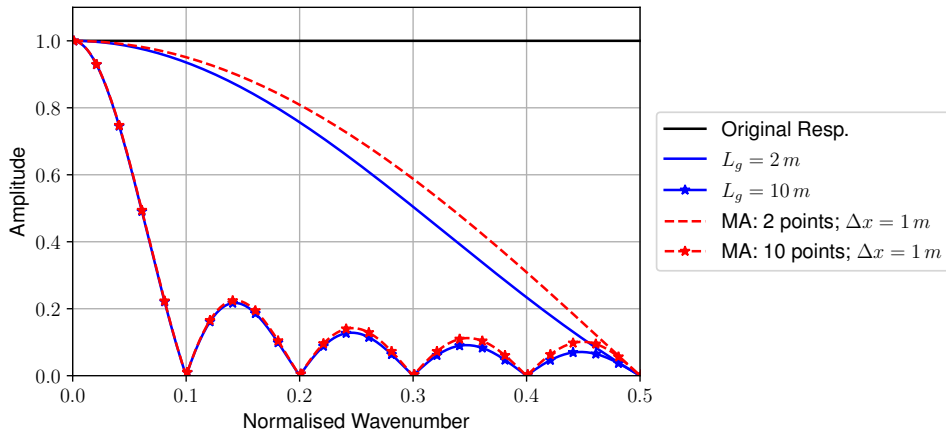
Figure 5.2: *Gauge length vs. moving average (MA) wavenumber response*

■ 5.2.1 Effect of gauge length on linear events

To examine the effect of gauge length on surface waves, we will look at the response with linear events in simple homogeneous models. A bandlimited wavelet with a wide frequency band ramping up from 0.01 to 10 Hz at the low end, and ramping down from 55 to 90 Hz at the high end; this is shown in Figure 5.3. These slopes are chosen to minimise ringing in the source time function. In order to examine the effect on events with different velocities, the source is injected in a homogeneous medium with $V_s = 240$ m/s and another medium with $V_s = 800$ m/s: both shots that are summed. The synthetic data are generated with finite-difference code [*Thorbecke and Draganov*, 2011] and are initially spatially sampled by receivers at 0.5 m. For every position, we simulate the different gauge lengths by calculating the mean of the traces corresponding to the gauge length of choice. So for a gauge length of 10 m for example, the mean of 20 finite-difference 0.5-m traces are taken. The channel spacing is kept fixed at 0.5 m for all the shots.

Figure 5.4 shows the synthetic records with the two events using different gauge lengths, namely, 2 m, 10 m and 20 m. We can see that longer gauge lengths affect slower events more significantly than faster ones. We see this in the time-space domain as distortion in the waveform, where it gets stretched in time. In the frequency-wavenumber (f, k_x) domain, we can see also these distortions as notches that are frequency-independent. We can see that these notches show up earlier, the higher the gauge length is. These predicted notches every $k_x = n/L_g$ are plotted in red in Figures 5.4g and 5.4h.
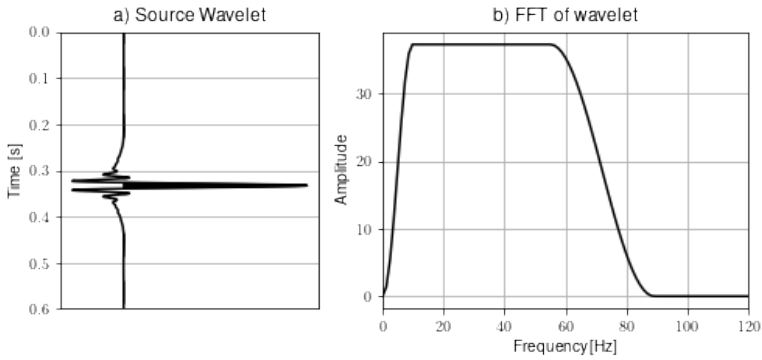
Figure 5.3: *Source wavelet (a) and its amplitude spectrum (b)*
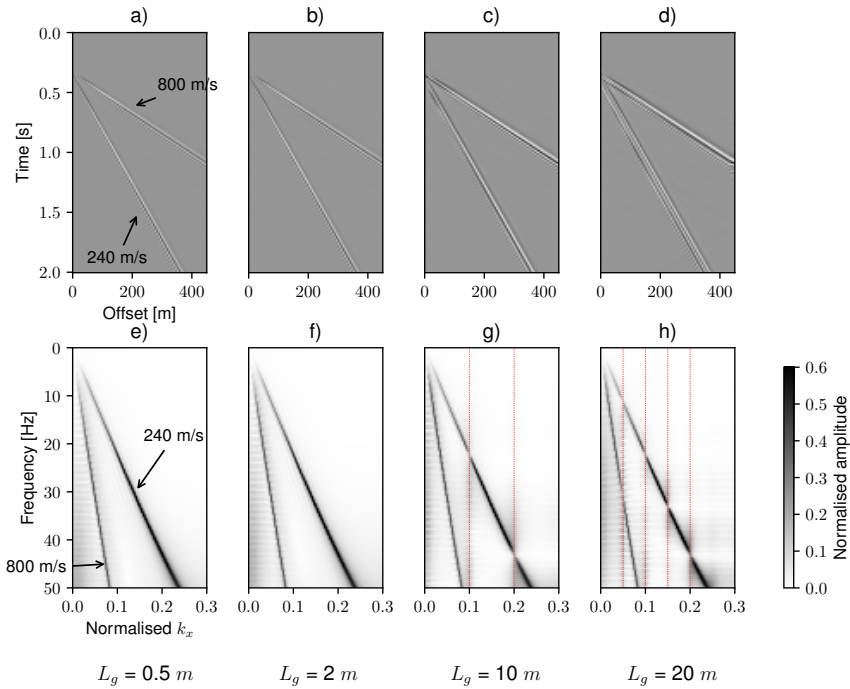

Figure 5.4: *Time-distance (top) and frequency-wavenumber (bottom) plots of two events of 240 and 800 m/s, for different gauge lengths. The channel spacing is kept at 0.5 m for all the synthetic shots. The red dotted lines in g and h panels indicate the theoretical positions of the notches at every n/L_g.*

Field-data examples of gauge-length effect on linear events

Here we show data examples from the field experiment discussed in chapter 4 of the fibres connected to a Febus A1-R interrogator. Four fibres were connected, namely two straight fibres and two helically wound fibres with wrapping angles of 30° and 60°. Only one straight fibre is discussed here as we saw no significant differences between the two in the responses. The shots were recorded at source position 144 m. We acquired the data in the raw format of the Febus A1-R interrogator which allows the processing of the raw data to strain-rate with different gauge lengths.

First, we consider the straight-fibre data. Figure 5.5 shows shots with different gauge lengths for the straight fibre, namely 2, 10 and 20 m at source position 144 m. On all shots, a low-pass filter is applied with a corner frequency of 55 Hz. We can see that longer gauge lengths favour low-wavenumber events, i.e., gentle slopes (see Figures 5.5e, 5.5f and 5.5g). We can see that a faster packet of waves is therefore enhanced with a gauge length of 20 m compared to the one of 2 m. On the other hand, for slower surface waves, distortions are present in the record and manifest as extensions in time (Figure 5.5d). We see that it significantly affects the data at higher frequencies more than the data at low frequencies, as shown in Figure 5.5h.

Next, we consider the helically wound fibre with a wrapping angle of 30°. As shown previously (see Chapter 4), the use of helically wound fibre significantly suppresses some surface-wave energy. In this cable, the ratio of fibre length to cable length is 2, in accordance with a wrapping angle of 30°. This would have implications on the surface wave sensed by the cable and becomes observable in the (f, k_x) spectra for different gauge lengths. For a gauge length of 2 m corresponding to 1 m of cable, we see that the surface-wave energy is twice as much compared to what is recorded by the straight fibre (see Figure 5.6). As can be seen, increasing the gauge length to 10 m, so 5 m of cable, therefore enhances the surface-wave energy.

Finally, we consider the helically wound fibre with a wrapping angle of 60°. For a helically wound fibre with such a wrapping angle, the fibre-to-cable length ratio is 1.15. Also here, the fibre shaping into a helix decreases the sensitivity to surface waves. Figures 5.7a, 5.7b and 5.7c show shots with $L_g = 2$, 10 and 20 m, respectively. We see that increasing the gauge length from 2 to 10 m will make the surface wave more visible, however, when it is increased to 20 m, the slow surface wave linear events are distorted (see Figure 5.7c), despite having higher S/N ratio for individual traces (see Figure 5.7d). So we can conclude that although it may be attractive to use large gauge lengths because of a high signal-to-noise ratio, it distorts the response when the gauge length is roughly larger than half the wave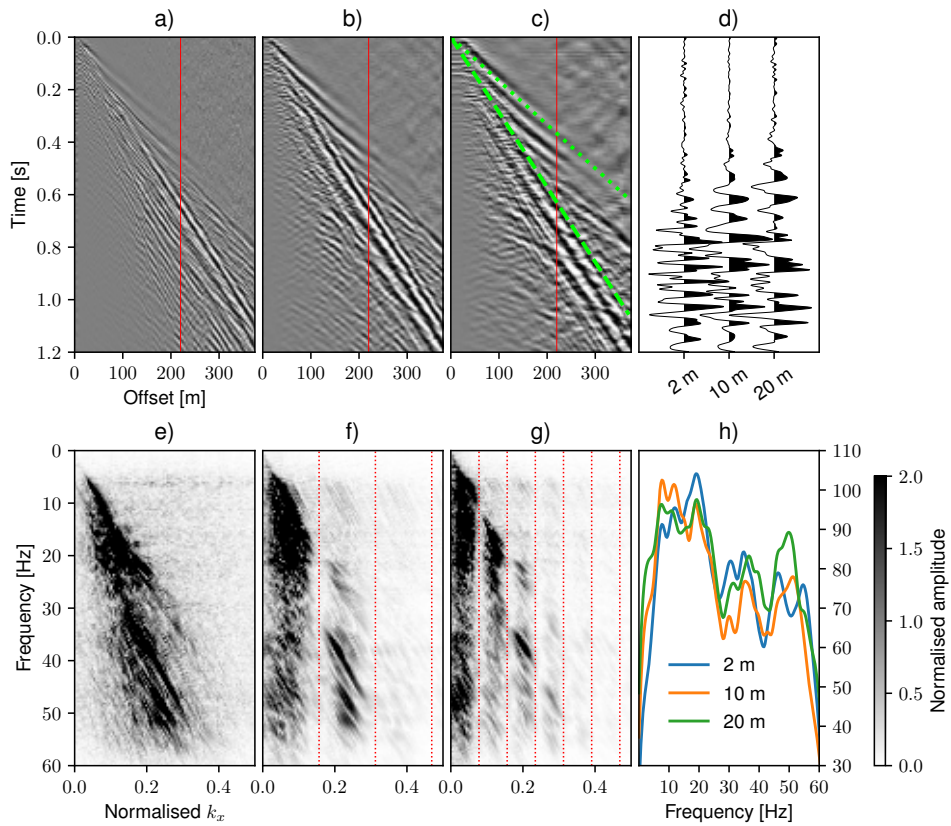length involved (spatial Nyquist sampling). So based on our field data, we can conclude that although it may be attractive to use large gauge lengths because of a high signal-to-noise ratio, it distorts the response when the gauge length is roughly larger than half the wavelength involved (spatial Nyquist sampling).

Figure 5.5: *SF field data with gauge lengths 2 m (a), 10 m (b) and 20 m (c), and their respective $|(f, k_x)|$ spectra, 2 m (e), 10 m (f), 20 m (g). Traces at offset 220 m from different gauge lengths (d) and their amplitude spectra in dB scale (h). The red dotted lines in the f and g panels indicate the theoretical positions of the notches at every n/L_g. The green lines in panel c correspond to velocities 350 m/s (dashed) and 600 m/s (dotted).*

■ 5.2.2 Dispersion characteristics estimated from different gauge lengths and fibre geometries

A common method used to estimate the near-surface shear velocity is the Multi-channel analysis of surface wave (MASW) [*Park et al.*, 1999a]. It makes use of the dispersive nature of surface waves. The method involves using the transformation of multi-channel data into the phase-velocity vs. frequency domain [*Park et al.*, 2005], where the different modes of Rayleigh or Love waves can be picked. Several methods are then used to invert the dispersion curves into shear-velocity vs. depth profiles that use the fundamental mode only [*Xia et al.*, 1999a], or methods that use higher modes too [*Xia et al.*, 2003; *Song and Gu*, 2007; *Maraschini and Foti*, 2010].
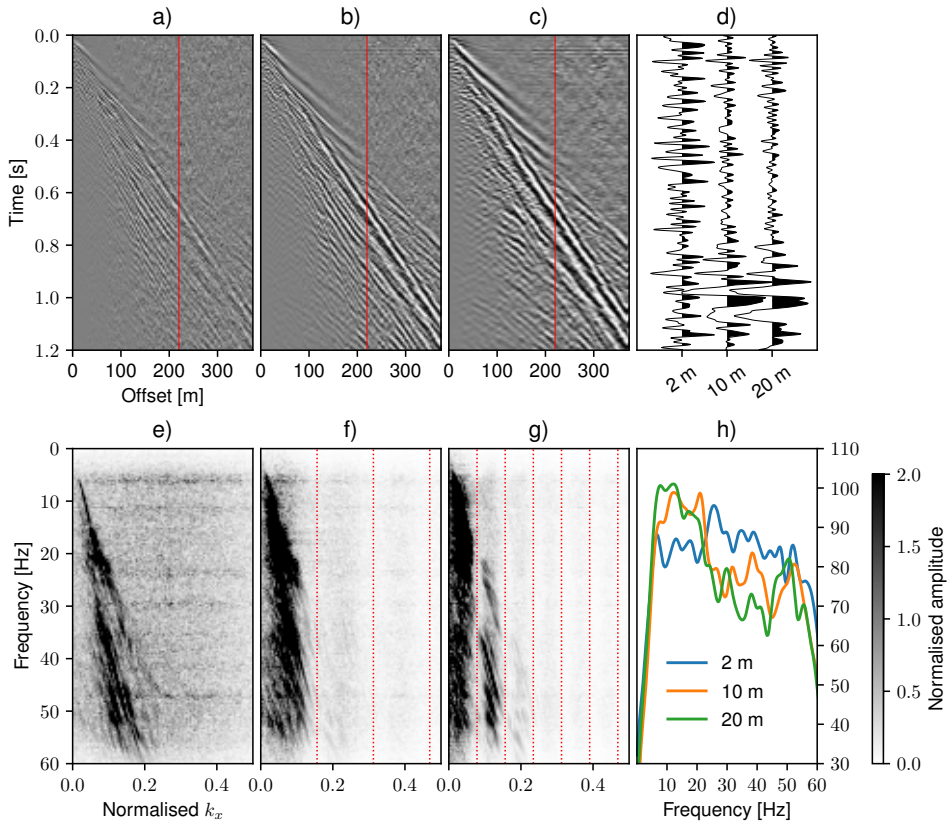
Figure 5.6: *HWF ($\alpha = 30°$) field data with gauge lengths 2 m (a), 10 m (b) and 20 m (c), and their respective (f, k_x) spectra, 2 m (e), 10 m (f), 20 m (g). Traces at offset 220 m from different gauge lengths (d) and their amplitude spectra in dB scale (h). The red dotted lines in the f and g panels indicate the theoretical positions of the notches at every n/L_g.*

The pickable range of dispersion curves determines its sensitivity to depth: greater depths are obtained with a dispersion curve that can be picked at the low-frequency/long-wavelength end, while for the shallow parts, the presence of higher frequencies/short-wavelengths enhances the details in the inverted shear-velocity vs. depth profile [*Olafsdottir et al.*, 2018]. As we are using DAS, the choice of gauge length has a significant impact on the retrieved dispersion image and the dispersion curve(s) that can be picked, and hence its sensitivity. Therefore, we will be looking at the dispersion images obtained with the modelled and measured DAS data. We also will be looking at the dispersion images obtained from different fibre configurations, namely straight and helically wound fibres.
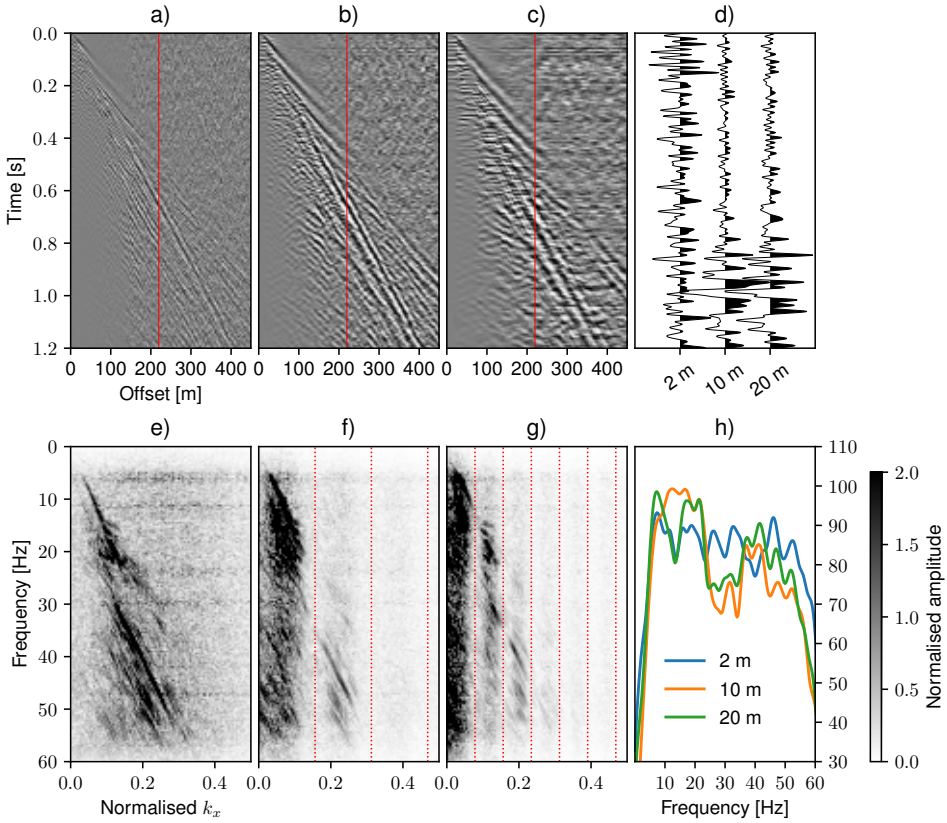
Figure 5.7: *HWF ($\alpha = 60°$) field data with gauge lengths 2 m (a), 10 m (b) and 20 m (c), and their respective $|(f, k_x)|$ spectra, 2 m (e), 10 m (f), 20 m (g). Traces at offset 220 m from different gauge lengths (d) and their amplitude spectra in dB scale (h). The red dotted lines in f and g panels indicate the theoretical positions of the notches at every n/L_g.*

Dispersion characteristics for different gauge lengths

In order to see the effect of gauge length on the dispersion characteristics of the Rayleigh-type surface wave, let us first consider a modelled response. Dispersion images of phase velocities estimated from the synthetic seismograms (e.g. Figures 5.4a to 5.4d) for different gauge lengths are shown in Figure 5.8. The curves for fixed wavelengths are plotted on top of the dispersion images. Focusing on the fundamental mode, we can see in the dispersion images that there are two events corresponding to the fast and slow events. We also can see that longer gauge lengths will enhance the dispersion at lower frequencies, i.e. longer wavelengths. We also see that the notches in the wavenumber domain will show here as notches for specific wavelengths. We see this for the dispersion image for $L_g = 10$ m, where we see

the notch affecting the dispersion curve of the fast event once and twice for the slow event. We can also see that for even a longer wavelength, i.e. 20 m, multiple notches affect the dispersion curve for the slow event. This makes it hard to pick the fundamental mode and it could be mixed with higher modes in practice.
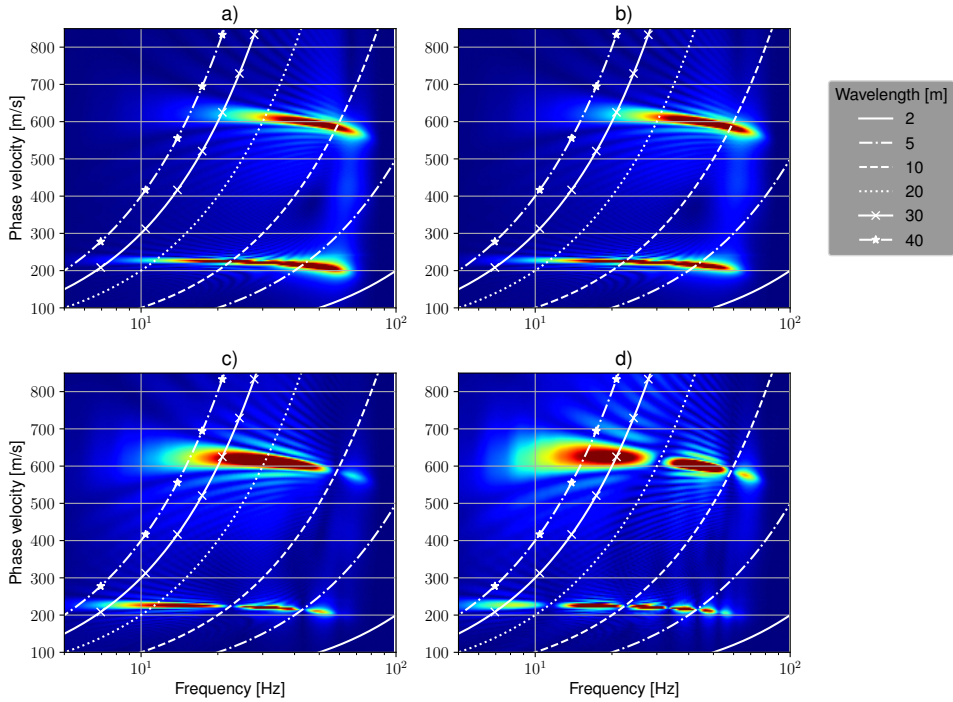

Figure 5.8: *Dispersion images estimated from straight fibre synthetic seismograms with different gauge lengths: a) Dispersion image using data with an original sampling of 0.5 m, b) $L_g = 2$ m, c) $L_g = 10$ m and d) $L_g = 20$ m.*

Next, we discuss the measured response of the straight fibre in the field data. Dispersion images are calculated from the shots with different gauge lengths (see Figure 5.5). Going from a gauge length of 0.5 m to 2 m, the fundamental mode does not seem to be affected, except at low frequencies/long wavelengths where the dispersion is slightly better with $L_g = 2$ m compared to $L_g = 0.5$ m. Some of the higher modes are affected by the use of a 2 m gauge length.

For $L_g = 10$ m, we can see in the fundamental mode that only frequencies up to 15 Hz are retrieved compared to $L_g = 2$ m, where the dispersion is retrieved at about 20 Hz. As for $L_g = 20$ m, the phase velocity of the fundamental mode is underestimated. Furthermore, it appears that higher modes are showing up with

a gauge length of 20 m (Figure 5.9d), which might be related to the increased coherency of events corresponding to velocities between 350 and 600 m/s as shown in Figure 5.5c.

Finally, we discuss the measured response of the helically wound fibre ($\alpha = 30°$). This is shown in Figure 5.10. We can see that using a short gauge length, e.g. $L_g = 2$ m, would limit the recovered amplitude of the fundamental mode. We see that the fundamental mode misses the low-frequencies/long wavelengths of the surface wave. We also see that higher modes are well shown with such short wavelengths. Increasing the gauge length, i.e. 10 m and 20 m, would enhance the fundamental mode at the lower frequency end.
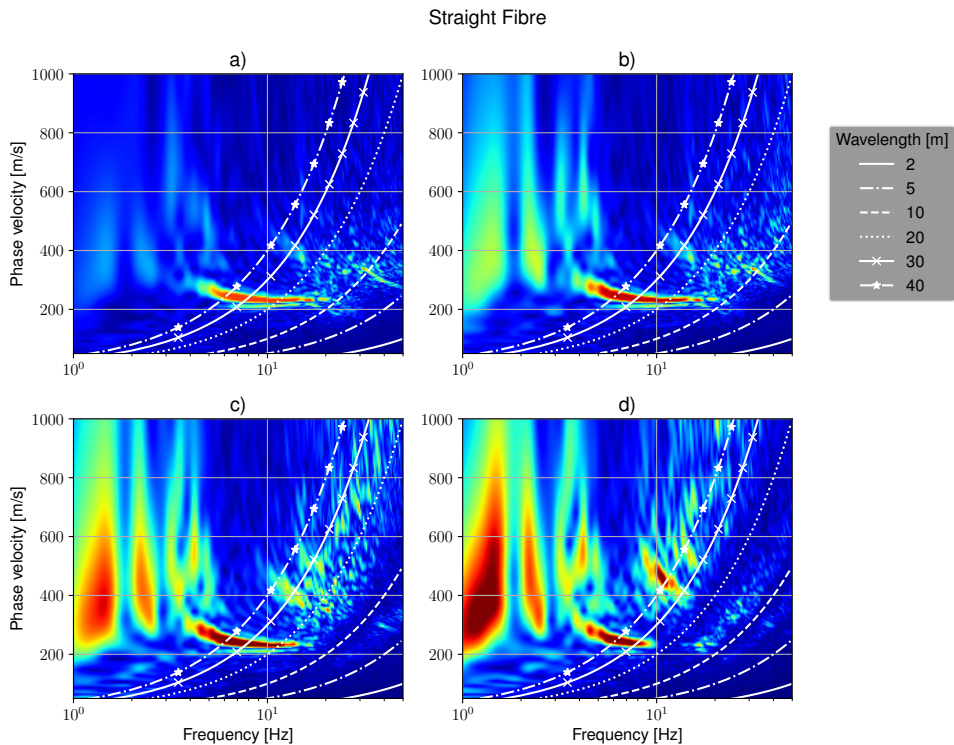
Figure 5.9: *SF dispersion images estimated from the field data with different gauge lengths: a) Dispersion image using data with $L_g = 2$ m, b) $L_g = 5$ m, c) $L_g = 10$ m and d) $L_g = 20$ m.*
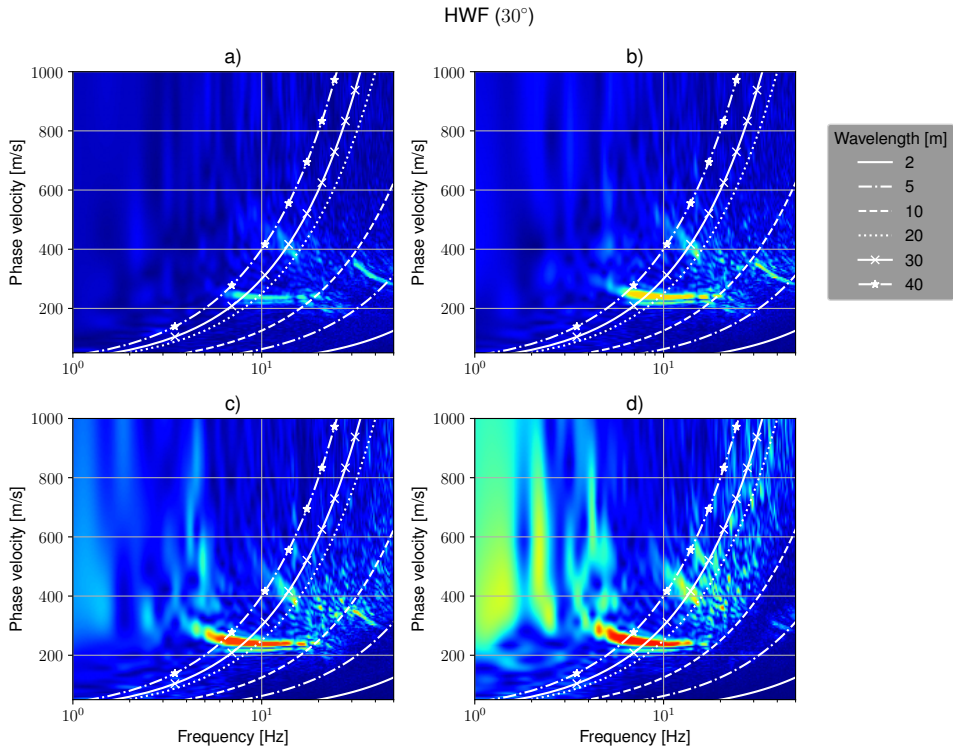
Figure 5.10: *HWF ($\alpha = 30°$) dispersion images estimated from the field data with different gauge lengths: a) Dispersion image using data with $L_g = 2$ m, b) $L_g = 5$ m, c) $L_g = 10$ m and d) $L_g = 20$ m.*

5.3 Passive data: effect of fibre geometry

In this section, the effect of the fibre geometry on retrieving information from passive data is studied. First, we will look at the retrieved response from an earthquake event recorded by our fibres. This is followed by an analysis of noise recordings by looking at their spectral content. Finally, we look at the retrieved responses for SF and HWF data using parts of these noise measurements.

■ 5.3.1 Induced Earthquake in Groningen

We have recorded the event shown in Figure 5.11 corresponding to an earthquake event on December 18th 2021 that is as interpreted by KNMI as an induced event [*KNMI*, 2022]. The magnitude of this event is estimated to be 1.3 from a depth of 3 km. We could see that the surface wave arrivals (arrivals after 70 s in Figure 5.11a) associated with the event have been clearly picked up by the straight fibres (SFs). On the other hand, though we see some arrivals in HWF, it is very difficult to interpret

the earthquake arrivals in those portions. This is expected as HWF has lower sensitivity to surface waves as also shown in *Baird* [2020]. Figure 5.11b contains a comparison between borehole seismometers at a nearby station (Zuidbroek G514) and traces from SF and HWF data. All traces are RMS-normalised. We see in the figure that surface-wave events (highlighted in red) are present in the SF data with decreased amplitude. This could be attributed to several factors including the lower sensitivity of DAS compared to borehole seismometers as well as the noisy environment of the near-surface where the fibres are buried. As for body-wave arrivals (highlighted by green), they seem to be below our detectable range along all fibres.
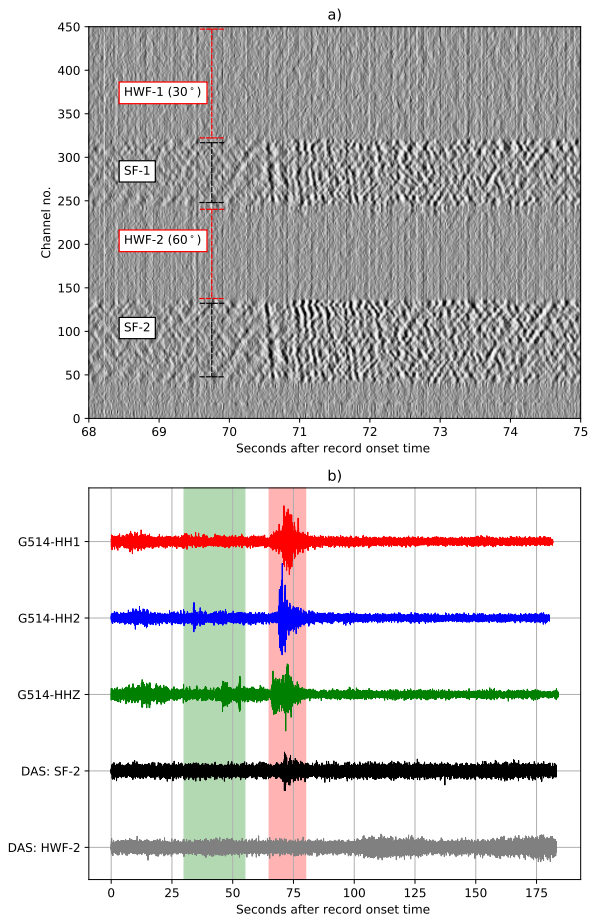
Figure 5.11: *Earthquake recording in Zuidbroek, Groningen; date: 18-12-2021, magnitude: 1.3 [KNMI, 2022]: a) DAS Earthquake Recording(record onset time: 02:32:22 UTC) and b) Zuidbroek G514 seismometers vs. DAS (record onset time: 02:32:24 UTC).*

■ 5.3.2   Noise recordings and surface-wave retrieval with interferometry

Passive data were collected over the weekend between March 26 and 29, 2021. They were recorded with an iDAS™-v3 system connected to a cable containing both straight and helically wound engineered fibres. The helically wound fibre has a wrapping angle of 60°. Since both fibres are engineered ones, they are expected to give stronger signals than standard fibres. The data have a sampling frequency of 1 kHz, a gauge length of 2 m and a spatial sampling of 1 m. However, for our analysis, the data were decimated in time and space to 4 m spacing for practical purposes. In our area, many coherent-noise sources are present that could be used for correlation.

Figure 5.12 shows the power spectral density of the continuous 3-day measurements over the weekend between March 26 and 29 in 2021 for the SF and HWF data. The first thing to observe is the presence of a frequency of some 30 Hz signal (see Figure 5.12a and Figure 5.12b). This is probably noise nearby the interrogator unit evidenced by its presence at all times and in the whole stretch of fibre, including the connection cable at the surface. Another thing to observe is that the SF picks up significantly more energy than HWF, comparing Figure 5.12a with Figure 5.12b. In the SF data, we can see that they are dominated by energy at frequencies below 10 Hz. Furthermore, during the day, i.e. from 06h to 17h, we can see the presence of higher-frequency sources, i.e. up to 25 Hz. Figures 5.12c and 5.12d show the sum of power spectral densities (PSDs) up to 25 Hz estimated from the SF and HWF data, respectively. We can see some periodicity in the noise source picked by SF. Looking at a zoomed part highlighted by blue in Figure 5.12c, we see that these events are repeated consistently every 30 minutes (see Figure 5.12e) We attribute these events to passing trains nearby the buried fibres since they were passing some 300 m away from the fibre lines. The train timetable was checked to confirm this [*Reisplanner*, 2023]. Comparatively, only a few noise sources are picked up by the HWF.

Seismic interferometry using SF and HWF

Seismic interferometry is a method of generating seismic responses by means of cross-correlation of measurements at different receiver locations [*Campillo and Paul*, 2003; *Shapiro and Campillo*, 2004; *Curtis et al.*, 2006; *Wapenaar et al.*, 2010]. It is a methodology to estimate the Green's function between two receivers where one of them is considered as a virtual source. For the sake of simplicity, we will consider a 1D case, where the ambient noise source and both receivers are in the same plane. Following the illustration shown in Figure 5.13a, assuming a homogeneous medium with a velocity of V, a plane wave source (i.e. considered to be the ambient noise source) is located at x_s, and two receivers at positions x_A and x_B. The Green's function representation at x_B as if the source is at x_A is obtained with the cross-correlation of the responses in the time domain as follows:

$$G(x_B, x_A, t) = G(x_B, x_S, t) * G(x_A, x_S, -t), \qquad (5.3.1)$$

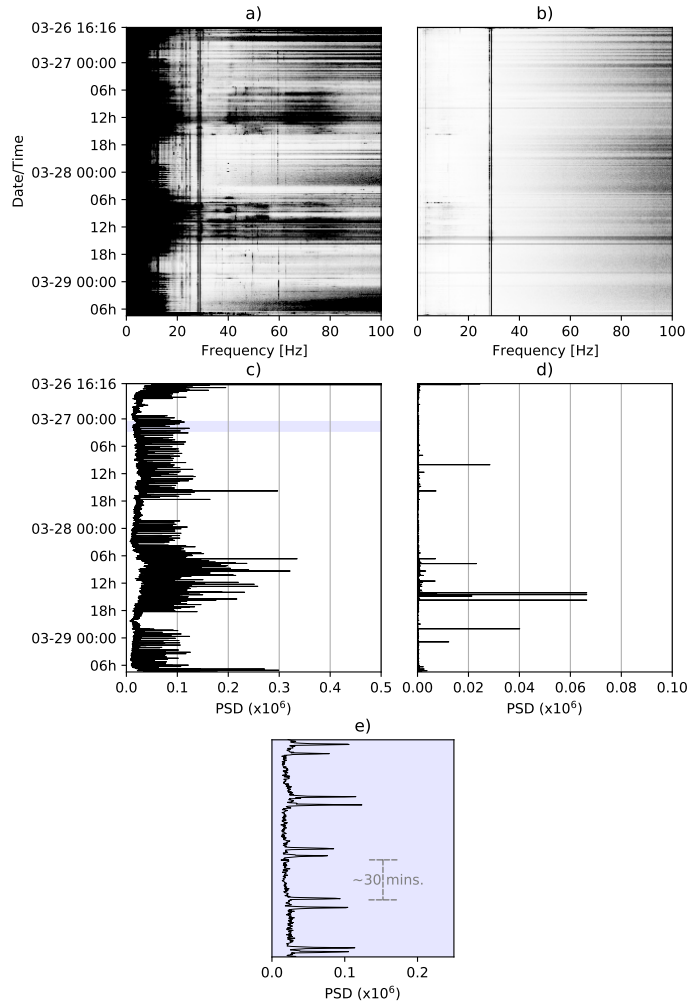where the asterisk denotes convolution and the $-t$ corresponds to time reversal.

Figure 5.12: *Power Spectral Densities (PSDs) of SF data (a) and HWF data (b). PSD summation up to 25 Hz for SF data (c) and HWF data (d) and zoomed view of PSD summation of SF data (e).*

As shown in *Wapenaar et al.* [2010], the traveltimes from the source at x_S and the receivers at x_A and x_B are expressed by $t_B = (x_B - x_S)/V$ and $t_A = (x_A - x_S)/V$, respectively. We can see that only the distance between x_A and x_B and the medium velocity V matter to time the arrival, as the travel time to x_A is shared by the two receivers, and therefore will cancel out in the cross-correlation. So for a response measured in the scenario shown in Figure 5.13a, the arrival in the Green's function at x_B for a virtual source at x_A is shown in the positive times as $t_B - t_A$ is also positive (see Figure 5.13b) and it is negative when looking at the Green's function at x_A from a virtual source at x_B (see Figure 5.13c). Seismic interferometry can be used to obtain several types of waves, such as surface waves and reflections, amongst them. An example of retrieving reflections is shown by *Draganov et al.* [2009]. Here we shall use this method mainly to retrieve surface waves.
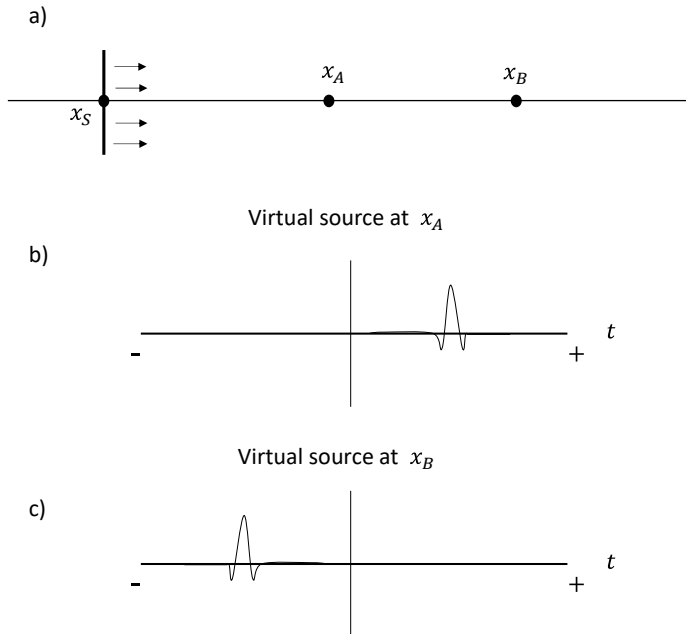

Figure 5.13: *Illustration of 1D interferometry: a) shows a plane wave source at x_S, and receivers at x_A and x_B. b) Cross-correlation function at x_B for a virtual source at x_A. c) Cross-correlation function at x_A for a virtual source at x_B.*

Passive surface-wave data: processing

Here we examine the use of some basic conditions and stacking methods to retrieve the surface wave with interferometry for SF and HWF data. These include the use of 1-bit normalisation of the data versus using the raw data directly. Furthermore, we examine the use of more advanced stacking methods like phase-weight stacking (PWS) compared to mean stacking. As *Bensen et al.* [2007] claim, it minimises the noise in the retrieved surface-wave signal. Only 1 hour of noise measurement is considered with a correlation length of 3 seconds to create virtual shots. For display purposes, the resultant virtual shots were filtered with a band-pass filter with corner frequencies of 2 and 25 Hz. Figures 5.14a to 5.14d show the results for SF and Figures 5.14e to 5.14h for HWF.

Looking at the results from SF vs. HWF in general, we can see that surface waves are better retrieved in SF than in HWF. For SF data, phase-weighted stacking seems to shorten the coda (see, e.g., beyond 2 s in Figures 5.14a and 5.14b). For HWF data, however, despite the shorter coda, we lose the coherency in retrieved surface waves (see, e.g., the dimming at the larger offsets in Figures 5.14e and 5.14f). As for the 1-bit normalisation, we could see significant improvement in the virtual shots, especially for HWF channel positions less than 100m. We also see a spurious "event" at the zero-lag time in the HWF data that is not present in the SF data.

Furthermore, comparing the dispersion behaviour of the stacks will give us an indication of which method is better for our application. Figure 5.15 shows two dispersion images of the SF data derived from cross-correlation functions using 1-hour ambient noise with mean stacking (i.e. Figure 5.15a) and PWS (i.e. Figure 5.15b). We see that using mean stacking, the fundamental mode lacks frequencies higher than 4 Hz. Unlike for PWS where the band 4 to 6 Hz is well recovered. Also, we see that the low-frequency part is not recovered correctly in the dispersion image of the mean stack (i.e. Figure 5.15a) compared to the phase-weighted stack (i.e. Figure 5.15a).

Correlation and dispersion results of 15 hours ambient noise records

We correlated 15 hours of data to retrieve the surface wave for SF and HWF, as shown in Figure 5.16. Clearly, the one retrieved from HWF is not as good as the one from SF. This is attributed to the decreased sensitivity to surface waves as previously mentioned (see Chapter 4). The surface-wave estimate from the HWF is improved with the use of 15 hours of ambient noise (i.e. Figure 5.16b) vs. 1 hour (i.e. Figure 5.14h). Looking at the frequency content of the data, we see in the amplitude spectra of the SF vs. HWF (see Figure 5.16c) that the data are dominated by energy below 8 Hz for both fibres with higher amplitudes for SF than for HWF. As for amplitudes for frequencies higher than 8 Hz (marked by a grey dashed line in Figure 5.16c), they steadily decrease with higher frequencies in SF, which is not the case for HWF where the amplitude seems to almost plateau.
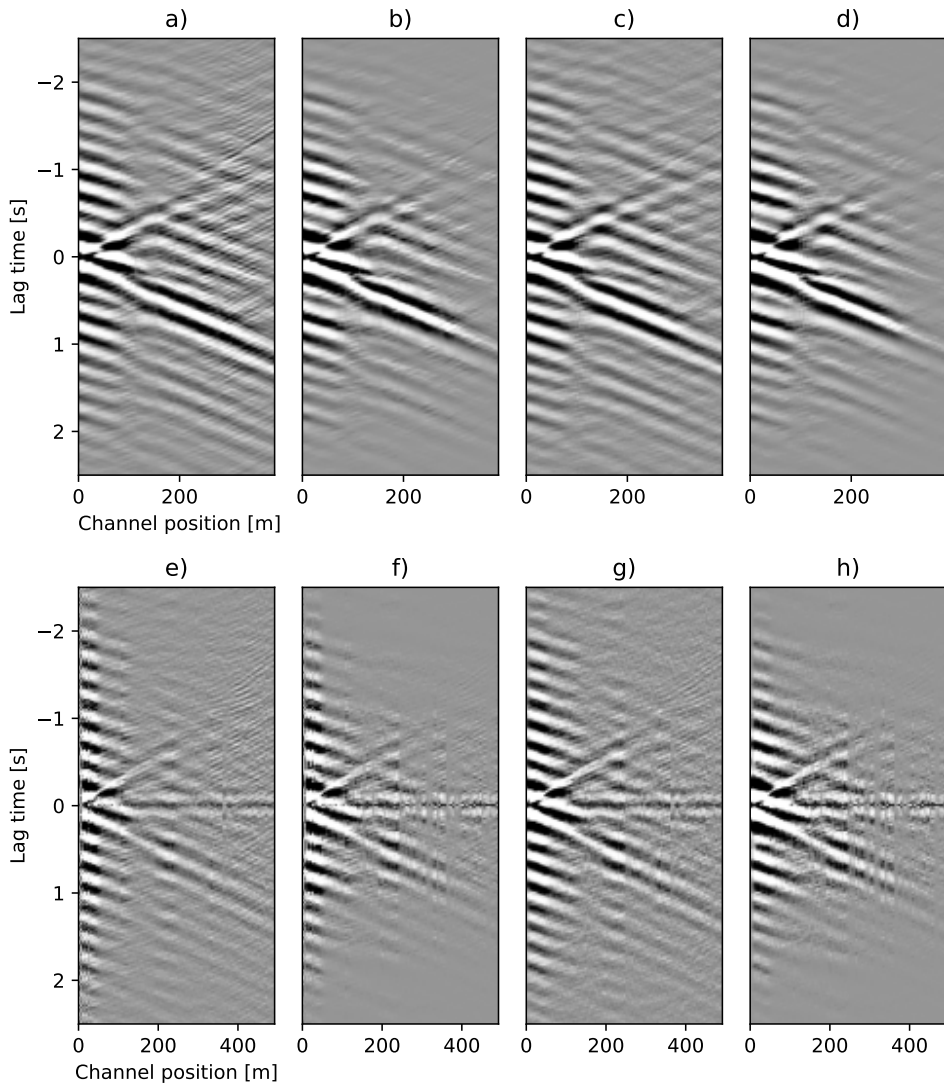
Figure 5.14: *Virtual shots with interferometry using different data normalisation and stacking methods. The top row shows SF data with the following: Raw data + Mean stacking (a), Raw data + PWS (b), 1-bit norm. data + Mean stacking (c), 1-bit norm. data + PWS (d). The bottom row contains the HWF data: Raw data + Mean stacking (e), Raw data + PWS (f), 1-bit norm. data + Mean stacking (g), 1-bit norm. data + PWS (h). PWS = Phase-weighted stacking*
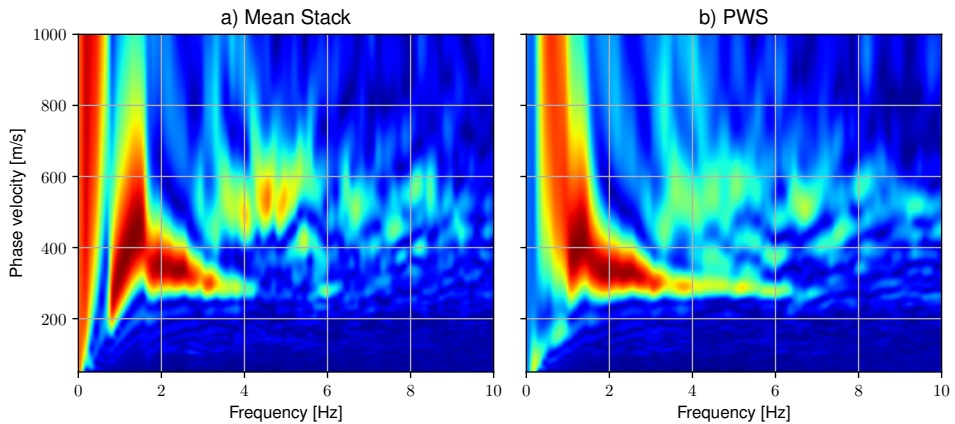
Figure 5.15: *Resultant dispersion images of the SF data from mean stacking (a) and phase-weight stacking (b).*

5.4   Discussion

Throughout this chapter, the focus was on assessing the use of SF and HWF data on the retrieval of surface waves, specifically on the influence of gauge lengths and fibre configurations. Using the passive data (i.e. virtual shots estimated with interferometry), we showed better surface-wave retrieval with the SF data compared to HWF data. However, for higher frequencies (i.e. > 8 Hz), we see that the amplitudes are relatively lower for SF relative to HWF. This could be seen as preferential for P-wave arrivals (i.e. P-wave first arrivals and reflections). It is also the case while examining induced earthquake event records in Groningen, where the P-wave arrival was not picked up by the HWF despite the alleged increase in broadside sensitivity [*Kuvshinov*, 2016; *Hornman*, 2017]. This might be due to the high noise level near the surface where the fibres are deployed.

We looked into several aspects of the retrieved surface wave including the responses in the space-time domain and wavenumber-frequency domain, and the consequences for the dispersion images, although in this chapter the next steps of picking the dispersion curves and inverting them to a shear-wave section are not discussed; this was seen as not being part of the focus of this chapter. These next steps are shown in appendix B and published by *Dalkhani et al.* [2023], where the SF data with a gauge length of 2 m is used for inverting for the near-surface S-wave velocity with MOPA.
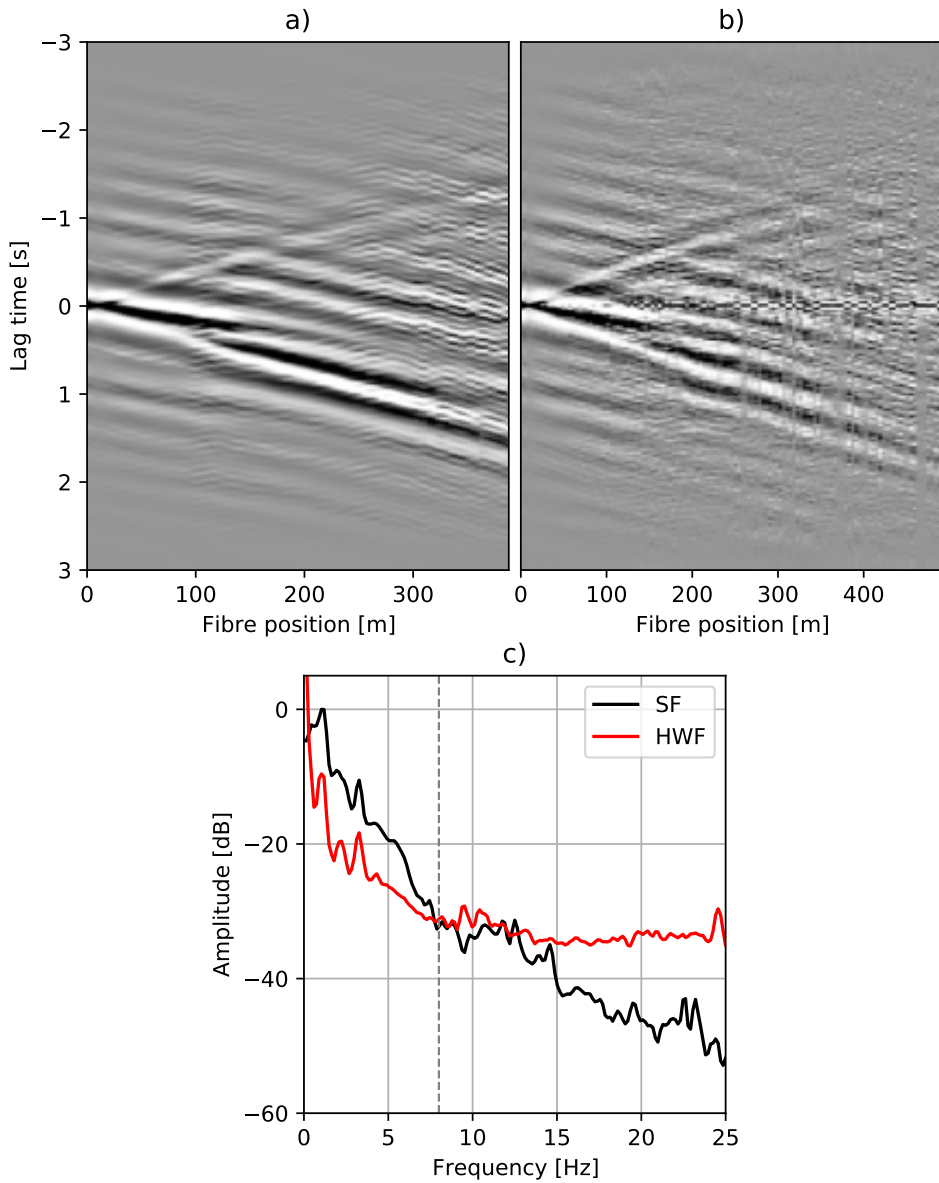
Figure 5.16: *Surface wave estimation with crosscorrelation using ambient noise records of 15 hours: virtual shot using SF data (a) and HWF data (b) and their amplitude spectra estimated from the whole shot (c).*

5.5   Conclusions

In this chapter, we discussed two major points on the retrieval of surface-wave using DAS including the effect of the gauge length and the fibre configurations. First, we started by describing the effect of gauge length and how it resembles to a certain extent the effect of array forming, i.e. a moving average in space. Using active-source measurements, we analysed the effect of gauge length on the linear surface-wave events via synthetic modelling and field data by looking at them in the time-space domain. As was suggested by modelling (refer to chapter 4), helically wound fibres suppress surface waves, and this was corroborated by our active-source DAS field data which makes it not the best choice for the retrieval of surface waves.

After that, the dispersion behaviour of these surface-wave events for different gauge lengths and different fibre configurations is examined. We saw the gauge length of choice depends on the type of fibre. For a straight fibre, a 2 m gauge length has given us a dispersion curve covering a wide range of wavelengths. So it is reasoned that if the signal-to-noise ratio allows, a short gauge length, sampling the wavefield sufficiently, is needed to obtain continuous reliable dispersion curves for obtaining shear-wave velocity profiles. So for DAS data acquisition, the choice of gauge length should be done with that in mind which is especially important for DAS interrogators that require choosing the gauge length prior to acquisition. Therefore, having prior knowledge about the expected velocity range in the area of interest as well as the frequency of the source will help in choosing the suitable gauge length. It is safe to say that DAS interrogators with the option of choosing the gauge length post-acquisition would provide great benefit, especially with the possibility of using multiple gauge lengths on the same dataset.

Following the active source examples, we analysed the passive data recordings. We showed an earthquake recording with DAS that has only been picked by straight fibres so also here it is corroborated that HWF suppresses surface waves. This is followed by looking at the ambient noise sources. We saw significant differences in the spectral content recorded by the SF compared to HWF, where repetitive events like a train passing every 30 minutes were recorded in SF but were not picked up by HWF. We then experimented with interferometry and showed we had recorded coherent surface wave events in both SF and HWF with better S/N ratios in favour of the SF. We showed that with such noisy data, specific processing steps will have a significant impact on the retrieved surface wave, especially the phase-weighted stacking which gave better results than linear stacking. Finally, we saw that even though the amplitudes are higher for SF in the retrieved surface waves (frequencies below 8 Hz), it seems to decrease significantly for higher frequencies, whereas HWF shows almost a constant sensitivity for higher frequencies.

6

Conclusions and recommendations

This chapter collects the main outcomes presented in the four main chapters of this thesis. In addition, it provides recommendations and an outlook for future research and developments.

6.1 Conclusions

DAS is still an emerging technology with great potential for further improvements. Its versatility is the main drive behind widespread adoption in a wide range of sensing applications. In seismic monitoring, the most attractive aspect of DAS is the dense spatial sampling it provides compared to conventional point sensors. However, DAS is still lacking in its use of horizontal deployment for surface-seismic reflection and multi-component measurements. The reason behind that is coming from the very nature of how an optical fibre behaves: it contracts and elongates as a function of time. It is, therefore, an intrinsic feature of an optical fibre that it has maximum strain sensitivity along its axial direction. The decreased broadside sensitivity is a major hurdle for surface-seismic and multi-component measurements. Therefore, in this thesis, several solutions are examined to tackle that by looking at several geometrical configurations of the fibre using both static and dynamic strain sensing methods.

In this thesis, I started with giving some background information on optical fibre sensing as it gives a wider understanding of topics relevant to the methods used in this thesis that includes: a brief idea on the physics of light propagation in an optical fibre, the scattering phenomena that are exploited for distributed acoustic sensing, some literature on the main challenges of DAS, such as the decreased broadside sensitivity, and finally citing the use of DAS in geophysical applications.

In Chapter 2, I examined the directional strain sensitivity using sinusoidally shaped fibres embedding in a homogeneous material. An analytical model was presented to describe the directional strain sensitivity of such a fibre configuration along with a finite-element model to validate it, and vice-versa. Loading experiments were

conducted on a sinusoidally shaped fibre embedding in a polyurethane-type material called Conathane®. The experiment was carried out using a static-strain device based on frequency-domain Brillouin sensing (BOFDA). The directional strain sensitivity was examined using three loading scenarios. The two main ones are called in-line and broadside cases. For the same compressive stress range, it was shown that, as expected by the analytical and numerical modelling, the fibre will be shorter for the in-line case, whereas it will get longer for the broadside case. The difference in sensitivity between the cases is small. Ideally, I wanted the in-line sensitivity to be as high as possible. Therefore, the undesired broadside sensitivity is relatively high. This is attributed to the high Poisson's ratio used in the embedding material.

Chapter 3 followed up on the point of the effect of Poisson's ratio of the embedding material. In this chapter, it was shown that, ideally, a zero-Poisson's ratio embedding material could provide a directional strain sensor. Therefore, a novel concept of low-Poisson ratio meta-material is adopted where I examined embedding the fibre in such a meta-material. The approach I followed was to produce a physical prototype using 3D printing technology as well as examine it using finite-element modelling. After several design and printing technology alternations, I made a small prototype. The fibre was manually glued to the material. Using a similar experimental approach as used in chapter 2, the loading cases of in-line and broadside are examined. I saw an improvement in the in-line sensitivity of the fibre. However, it is not as high as expected by the modelling. I saw that a wider adaptation of this geometry for DAS is quite challenging.

In Chapter 4, more common approaches are examined via a field experiment namely the combined use of straight and helically wound fibres (e.g. standard and engineered fibres) including different wrapping angles. The field experiment was conducted using a DAS interrogator linked up to a loop of different optical fibres buried in a 2 m deep trench on a farmland in the province of Groningen in the north of the Netherlands. The amplitude and phase information obtained from these fibre configurations were examined in pre-stack and post-stack domains. In the pre-stack domain, common-receiver gathers showed the effect of the wrapping angle of HWF on the amplitude and polarity and followed the predictions from synthetic modelling. In the post-stack domain, the engineered fibres showed comparable results to the one obtained from surface-geophone measurements where the main reflections are observable but with a lower S/N ratio. Surprisingly, the straight fibre showed a higher amplitude reflection image compared to the helically wound fibre, despite the theoretically predicted decreased sensitivity of the former. It appears that this might be linked to the coupling between the fibre cable and the surrounding soil, possibly due to the soil having a low Poisson's ratio. Finally, it was shown that combining straight and helically wound fibres is useful as each fibre configuration showed different sensitivity to reflections from different levels of the subsurface.

The last chapter 5 focused on the retrieval of surface waves using DAS. Two major points are considered, namely, the gauge length and the fibre geometry. The same active-source dataset as in chapter 4 was used and some passive continuous noise and an earthquake were used for our surface-wave analysis. Using the active-source data, I saw that the gauge length plays an essential role in the retrieval of the

surface wave as it causes distortions of the waveforms sensed with a straight fibre when a long wavelength (i.e. relative to the wavelength of the surface wave) is used. In the (frequency, horizontal-wavenumber)–domain, this manifests as notches in the horizontal-wavenumber direction, so frequency-independent. It is a different story for helically wound fibres, as longer gauge lengths might be necessary to retrieve the surface wave properly. This is due to the theoretically predicted decreased sensitivity of HWF to surface waves. I showed this decreased sensitivity on field data via the passive-source surface waves estimated via interferometry as well as via the induced earthquake recorded using the different fibres. An application of DAS using the SF data for shear-wave velocity inversion is presented in appendix B.

The use of different fibre configurations seems to be a frontier worth exploring. Using both theoretical and experimental approaches, I showed that the concept of a sinusoidally shaped fibre embedded in both homogeneous materials (i.e. Conathane®strip in Chapter 2) and the low-Poisson's ratio structure (i.e. Chapter 3) is showing some promise. Qualitatively, it is shown via analytical and numerical modelling as well as physical experiments that the in-line direction is more sensitive than the broadside sensitivity with flipped polarity. Several issues related to the quantitative misfit between theory and practice have been also discussed. With the field experiments, I showed that the combined use of different fibre configurations is beneficial both for reflection seismic (i.e. Chapter 4) as well as surface-wave analysis from active and passive data (i.e. Chapter 5). Different sensitivity to the wavefield is shown by the amplitude and polarity differences between the straight and the helically wound fibres with different wrapping angles (i.e. Chapter 4) and the effect of gauge length is considered for these different fibre geometries in Chapter 5.

6.2 Recommendations and future outlook

Although steps have been made forward in this thesis, several issues have not been resolved via the work done. Further investigations are needed to improve directional strain sensing for DAS application, if at all possible via similar shapings of the fibre. The following points are the main aspects that could be further investigated.

■ 6.2.1 On the concept of a sinusoidally shaped fibre

As I have shown in chapters 2 and 3, I see a potential for a directional strain sensor. This is illustrated by the difference in the behaviour of the fibre for the two main loading cases of in-line and broadside stress directions, where the fibre is shorter for the former and longer for the latter. It is also shown that the fibre is more sensitive in the in-line direction as expected from the theoretical models. Guided by the analytical and numerical modelling, I see that there is still room for improvements by a further increase in the in-line directions and a decrease in the broadside direction relative to what has been obtained experimentally.

The main assumption that needs examination is the one that the fibre is completely following the embedding material behaviour. Although the measurements described the modelling qualitatively, in a quantitative sense I see a significant mis-

fit. It is not clear what the cause of this misfit is. I saw in chapter 2 that it could be explained by a strain-transfer coefficient. However, for an anisotropic meta-material as used in chapter 3, the misfit is much higher and not well explained. I propose a further examination of the coupling between the fibre and embedding meta-material by building an analytical or numerical model that includes the mechanical properties of the fibre instead of only tracing a fibre as used in this thesis.

Another clear aspect is the adaptation of the concept of sinusoidally shaped fibre embedded in a low-Possion's ratio material for DAS. To do that, longer prototypes are required as most DAS uses a minimum gauge length of 1 m. Making such long samples would require remarkable work in developing a manufacturing method that significantly decreases the cost of making such samples. This engineering challenge can be resolved partly by further researching a way of simplifying the structure of similar behaviour. This could include an alternative low-Poisson's ratio configuration as well as optimising the placement of fibre within the structure with numerical modelling.

■ 6.2.2   On the combined use of straight and helically wound fibres

Using both straight and helically wound fibre provided extra information about the direction of the strain tensor component, namely a higher contribution of the vertical component ε_{zz} in the HWF than in the SF. Looking at the surface-wave responses, this manifests as changes in polarity and amplitude of the waveform. This hints in the direction that each fibre contains different contributions of both the horizontal and vertical component part of the strain-rate tensor as also confirmed by the synthetic modelling shown (based on *Baird* [2020]). It is safe to say that the model is still not complete as it fails to describe the amplitude differences between the HWF and SF in favour of the latter when looking at the reflections (i.e. outside the surface wave cone). This can be done by further investigation of the shaped fibre to the ground where further questions need to be answered, like: *Does the shaped fibre follow the embedded cable material directly or are there some coupling phenomena or strain-transfer functions to its surrounding that need to be considered?*. This will get us one step closer to a multi-component sensor for DAS measurements.

Furthermore, each gauge length in a straight fibre is equal to the length of the cable it is embedded in. For HWF though this is not the case since, depending on the geometrical parameters of the winding (i.e. wrapping angle and radius), the fibre length could be twice the cable length. So the combined use of the fibres is not that straightforward. Therefore, a method to estimate the different components from the combined SF and HWF data should take this into account. Finally, the combined use of straight and helically wound fibres has the potential to become the standard procedure for DAS measurements as the optical fibre cable manufacturing industry is mature enough to provide such a cable. This gives the potential to have custom-built optical fibre cables that have multiple fibres with different wrapping angles to use for obtaining the multi-component information [*Ning and Sava*, 2018a]. Manufacturing cables with multiple helices at different wrapping angles might come with a significant cost. This could lead to questioning whether their utilization offers substantial advantages over conventional point sensors such as multi-component geophones.

■ 6.2.3 On the use of alternative approaches than sinusoidally and/or helically wound fibres

Possible future improvements in interrogator technology, that allow short gauge length measurements (i.e. < 1 m) with decreased noise levels, will promote the adaptations of more direct ways to obtain multi-component DAS data. In a surface-seismic setting, this can be done while deploying the fibres and orienting each section, that corresponds to a single gauge length, to the desired directions. For a horizontal two-component cable configuration, one could have alternating horizontal in-line (x) and horizontal cross-line (y) fibres as shown in Figure 6.1a. The vertical component (z) fibre could also be included by deploying a section to the vertical shallow hole, or coupled and inserted vertically via a pole in the soil (see Figure 6.1b). Similar approaches have been examined previously by *Bakulin et al.* [2017] but here in our case, it requires much smaller gauge lengths (i.e. < 1 m) so we could deploy such arrangements with dense spatial sampling.
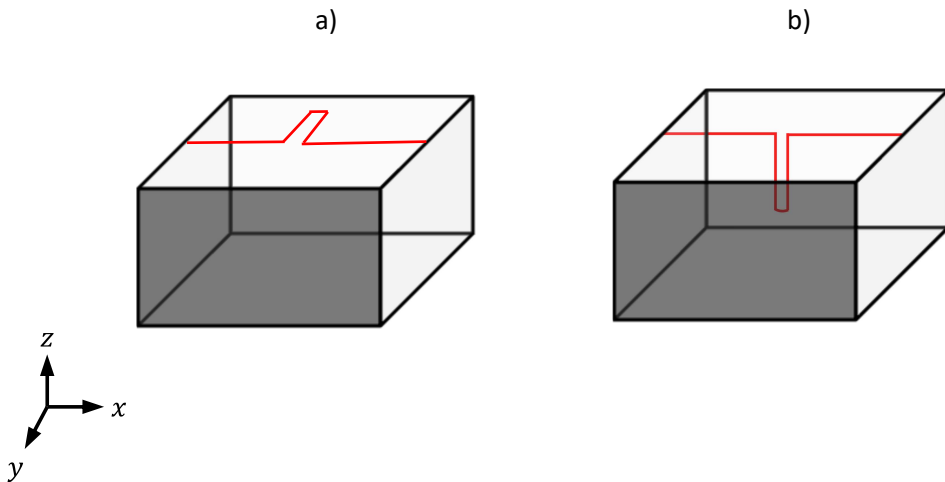
Figure 6.1: *Two-component fibre sensors with horizontal in-line and cross-line configuration (a) and a combination of horizontal in-line and vertical configuration (b).*

A

Supplemental Information to Chapter 2

A.1 Details on Numerical Model (3D)

Here we give details on the numerical model used to validate our analytical model. For in-line and broadside cases, the model consists of two parts, a rigid domain and a portion of a sample under load. The parameters of the model are based on the Conathane® material as used in the experiments (see table 2.1): the sample size is chosen as 1 m (corresponding to the portion under load) with a width of 6 cm and a thickness d of 1.7 cm; the sample material has Young's modulus of 17 MPa and a Poisson's ratio of 0.45. As for the along-strip case, the whole sample of 2 m long is used. The sinusoid is embedded in the middle of the sample.

The boundary conditions of the models for both loading orientations are illustrated in Figures A.1b and c. A rigid body is introduced to support the striped-shaped sample to resemble the laboratory experiment as closely as possible. In the broadside direction, a boundary load on the top of the sample in the negative y-direction is applied, and the sample is free to move along the contact with the rigid domain. For the case of in-line loading, a boundary load is applied in the negative z-direction noted by the stress σ_{zz} and the sample is free to move parallel to the contacts. Finally, for the along-strip case, the strip is fixed from one end, and loaded in the position x-direction in the other. Based on our physical sample, a sinusoid with parameters of $A = 2.4$ cm and $\Lambda = 6$ cm is traced in the sample in the y plane of $0.5d$, where d is the sample thickness. The location of the fibre $\mathbf{f_0}$ is expressed as:

$$\mathbf{f_0} = \begin{bmatrix} x \\ 0.5d \\ A\sin(2\pi\frac{x}{\Lambda}) \end{bmatrix}. \tag{A.1.1}$$

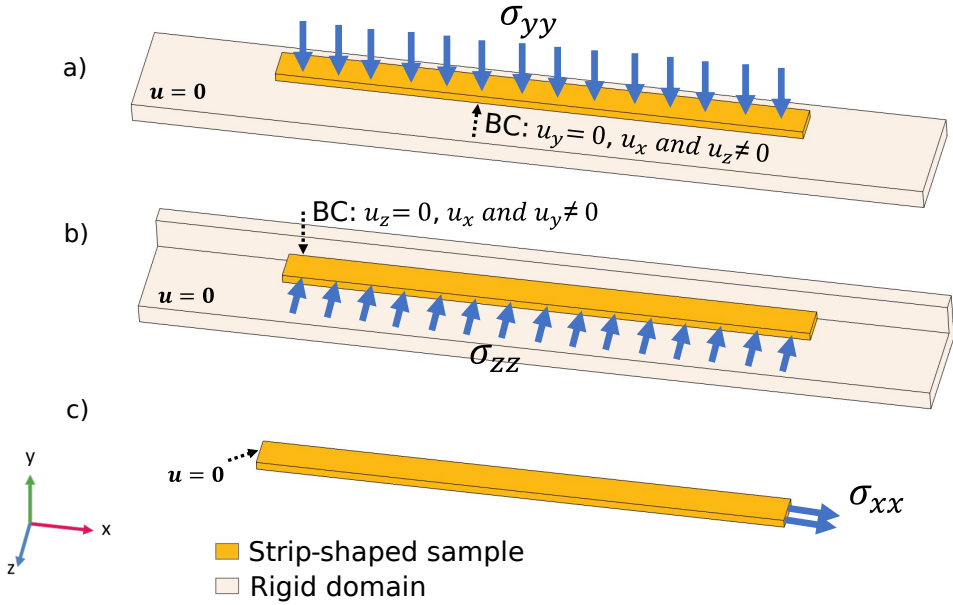Solving this numerical experiment will result in the displacement vector field

Figure A.1: *Loading cases: a) Broadside, b) In-line and c) along-side loading. Note that the boundary load is denoted by the blue arrows and the boundary condition at the contact with a dashed black arrow.*

$\mathbf{u} = [u_x \ u_y \ u_z]^T$ for the whole sample. This is shown in Figure A.2 containing the resultant components of displacements for a load of 1000 Pa.

We see that for all the cases, the difference in behaviour is solely determined by the displacement in the z-direction. This is clearly illustrated for the in-line case as a negative u_z overall that is out-of-phase with the embedded sinusoid. However, for the broadside case, u_z is in-phase with the sinusoid extending it in the y-direction. We also see that u_x is the same for both cases due to the Poisson's ratio. Displacement in y-direction is constant in the broadside direction, therefore no strain and it is very close to zero in the in-line direction. This is consistent with our analytical model. The major difference between our analytical and numerical models is that the deformed state in the former is derived using the strain directly acting on the sinusoid, whereas, in the latter, the displacements are extracted along the sinusoid from the numerical solutions. The location of the deformed fibre is then can be expressed by

$$\mathbf{f_d} = \mathbf{f_0} + \mathbf{u}. \tag{A.1.2}$$

After that arc length of sinusoids $\mathbf{f_0}$ and $\mathbf{f_d}$ are calculated and used in equation 2.2.12 to evaluate the strains.
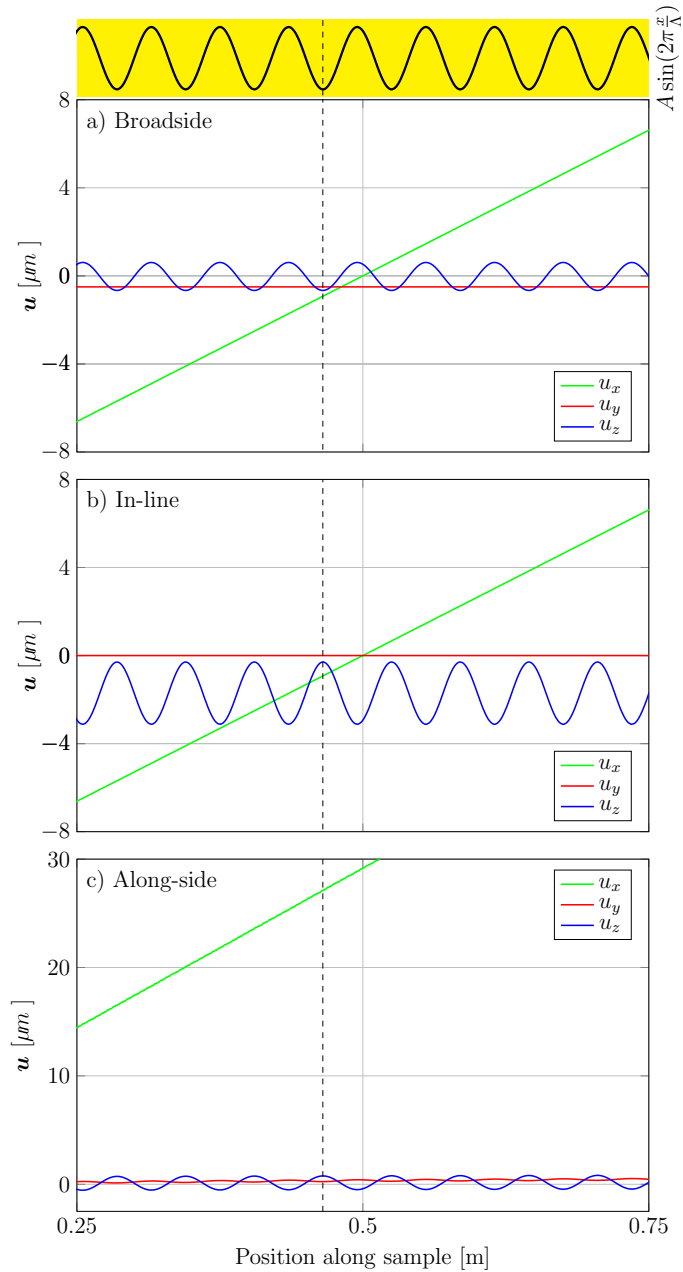
Figure A.2: *Displacement field components along the sinusoid $A \sin(2\pi \frac{x}{\Lambda})$ (highlighted by yellow) for loading of 1000 Pa. Zoomed to x=0.25 to x=0.75 m.*

B

Application of DAS for surface-wave analysis

Note

The following material is a preprint published online in arXiv as Rahimi Dalkhani, A., M. Al Hasani, G. Drijkoningen and C. Weemstra (2023), Transdimensional surface wave tomography of the near-surface: Application to DAS data, *arXiv preprint arXiv: 2304.10678v1.* The data used in this application is the SF data with a gauge length of 2 m using the engineered fibres. It was found to be the most suitable dataset as it had the best S/N ratio and best sensitivity to surface waves. As described in Chapter 4 and 5, the data went through several steps by Al Hasani to be ready for this application including the simultaneously active-source DAS acquisition as well as pre-processing steps.

Transdimensional surface wave tomography of the near-surface: Application to DAS data

Amin Rahimi Dalkhani[1], Musab Al Hasani[1], Guy Drijkoningen[1] and Cornelis Weemstra[1,2]

[1] Department of Geoscience and Engineering, Delft University of Technology, The Netherlands

[2] Seismology and Acoustics, Royal Netherlands Meteorological Institute, The Netherlands

Abstract

Distributed Acoustic Sensing (DAS) is a novel technology that allows sampling of the seismic wavefield densely over a broad frequency band. This makes it an ideal tool for surface wave studies. In this study, we evaluate the potential of DAS to image the near-surface using synthetic data and active-source field DAS data recorded with straight fibers in Groningen, the Netherlands. First, we recover the laterally varying surface wave phase velocities (i.e., local dispersion curves) from the fundamental-mode surface waves. We utilize the Multi Offset Phase Analysis (MOPA) for the recovery of the laterally varying phase velocities. In this way, we take into account the lateral variability of the subsurface structures. Then, instead of inverting each local dispersion curve independently, we propose to use a novel 2D transdimensional surface wave tomography algorithm to image the subsurface. In this approach, we parameterize the model space using 2D Voronoi cells and invert all the local dispersion curves simultaneously to consider the lateral spatial correlation of the inversion result. Additionally, this approach reduces the solution nonuniqueness of the inversion problem. The proposed methodology successfully recovered the shear-wave velocity of the synthetic data. Application to the field data also confirms the reliability of the proposed algorithm. The recovered 2D shear-wave velocity profile is compared to shear-wave velocity logs obtained at the location of two boreholes, which shows a good agreement.

B.1   Introduction

After the first field trials of the Distributed Acoustic Sensing (DAS) [*Bostick III*, 2000; *Molenaar et al.*, 2012; *Johannessen et al.*, 2012], the DAS found many applications in different geophysical problems [*Barone et al.*, 2021]. Due to the dense sampling of the wavefield and the broadband character, DAS is getting popular in surface wave studies both in active [e.g., *Qu et al.*, 2023; *Yust et al.*, 2023] and passive [e.g., *Ajo-Franklin et al.*, 2019a; *Nayak et al.*, 2021b] surveys.

A material's shear-wave velocity directly depends on its shear strength (or stiffness). Consequently, the shear-wave velocity of the near-surface is a valuable parameter in many subsurface engineering applications. And because the velocity of surface waves strongly depends on that shear-wave velocity, near-surface shear-wave velocity models are frequently derived from surface wave measurements [*Socco et al.*, 2010]. Typically, two types of surface waves are recorded: Rayleigh and Love waves [*Aki and Richards*, 2002]. Surface waves are dispersive when the shear-wave velocity varies as a function of depth, meaning that different frequencies propagate with different velocities. A surface wave's propagation velocity at an individual frequency is referred to as that frequency's 'phase velocity'. The first step in surface wave imaging is therefore usually the retrieval of the frequency-dependent phase velocities. An inversion subsequently results in a model of the shear-wave velocity as a function of depth [*Schaefer et al.*, 2011; *Zhang et al.*, 2020].

Conventionally, in an active-source surface wave analysis, a dispersion curve is retrieved from each common shot record using Multichannel Analysis of Surface Waves [MASW; *Park et al.*, 1999b] assuming that the subsurface is a stack of horizontal layers. Then, an inversion algorithm is used to recover a 1D shear-wave velocity profile [e.g., *Vantassel et al.*, 2022b; *Qu et al.*, 2023]. However, due to the fine spatial sampling and the high-frequency content of data recorded in an active-source survey, DAS recordings enhance the lateral resolution significantly [*Barone et al.*, 2021]. Consequently, many authors [e.g., *Neducza*, 2007; *Luo et al.*, 2008; *Vignoli et al.*, 2011; *Barone et al.*, 2021] suggested recovering local dispersion curves (DCs) to take into account the lateral variation of the subsurface velocity structure. These local DCs can then be used in an inversion algorithm to recover a 2D profile of the subsurface shear-wave velocity [*Vignoli et al.*, 2016; *Barone et al.*, 2021].

Several approaches have been proposed to account for lateral variations of the subsurface's shear-wave velocity. The most common approach involves the application of a moving window to the recorded shot gathers in the time-space domain [e.g., *Bohlen et al.*, 2004; *Luo et al.*, 2008; *Socco et al.*, 2009; *Boiero and Socco*, 2010]. The windowed part of the data is then transformed into a spectral domain to estimate the "local" dispersion curve at the location of the center of that window. Alternatively, Multi Offset Phase Analysis [MOPA; *Vignoli et al.*, 2016] can be used to consider lateral variation[*Barone et al.*, 2021]. *Vignoli et al.* [2016]; *Barone et al.* [2021] successfully retrieved fundamental-mode laterally varying dispersion curves using MOPA. Then, they inverted the local dispersion curves at each location independently to recover a 2D shear-wave velocity pseudo-section of the subsurface. It is worth noting that both studies [*Vignoli et al.*, 2016; *Barone et al.*, 2021] applied

the MOPA algorithm to the Geophone recordings.

In this study, we apply the MOPA algorithm to a 2D active-source DAS recording for the first time. We recover the laterally varying fundamental-mode local phase velocities. Then, we propose to invert all the dispersion curves simultaneously using a nonlinear 2D transdimensional tomographic algorithm [*Bodin and Sambridge*, 2009]. This transdimensional inversion algorithm is originally developed for seismic travel time tomography. Later, it has been used for many geophysical problems [e.g., *Dettmer et al.*, 2012; *Rahimi Dalkhani et al.*, 2021; *Ghalenoei et al.*, 2022; *Yao et al.*, 2023]. Here, we develop the algorithm for the purpose of active-source surface waves recorded with DAS to image and recover a 2D shear-wave velocity section of the subsurface with improved lateral correlation. Finally, we validate the inverted 2D shear-wave velocity section by comparing it with the shear-wave velocity logs obtained from two boreholes along the acquisition line.

B.2   Theory & methodology

In this section, we detail the various methods used in this study. First, we describe how the surface waves are obtained from the fiber optic recordings. Subsequently, we explain how we locally estimate the surface waves' phase velocity as a function of frequency. Finally, we provide the details of the McMC implementation.

■ Distributed acoustic sensing (DAS)

In this part, we describe what is measured by DAS and how it relates to geophone measurements. Unlike geophones which are point sensors that record the particle velocity at a specific location, DAS measurements are average strain-rate, i.e. $\dot{\varepsilon}_{xx} = \partial_t(\partial_x u)$, along a specific distance called the gauge length (L_g). Alternatively, DAS response can be equivalently represented by the spatial derivative of the velocity vector, i.e. $\partial_x(\partial_t u) = \partial_x V_x$ [*Daley et al.*, 2016].

We show a schematic illustrating a scenario mimicking our implementation in the field experiment in Figure B.1. A vertical source F_z will generate different types of waves including surface waves that are mostly Rayleigh waves. As DAS relies on the elongation and contraction of the fibre as a function of time, its maximum sensitivity is along its axial direction. So it is safe to say the majority of what is being recorded is the horizontal component of the Rayleigh waves. To compare what is being measured by geophones to DAS, horizontal (x) geophones G_{x_1} and G_{x_2} separated by distance dx is assumed to be recording the horizontal component of the particle velocity V_x at x_1 and x_2, respectively. Equivalent DAS response between the two geophones can be estimated as the spatial derivative of the particle velocity with the following expression adapted from *Zulic et al.* [2022]:

$$DAS\left(\frac{x_2 - x_1}{2}\right) = \frac{V_x(x_2) - V_x(x_1)}{dx}, \qquad \text{(B.2.1)}$$

where, dx is equivalent to the gauge length L_g of the DAS measurement. Given that the gauge length is small and using dense spatial sampling that to satisfy the

spatial Nyquist criterion, the phase velocity is not affected by the use of strain rate instead of the commonly used particle velocity.
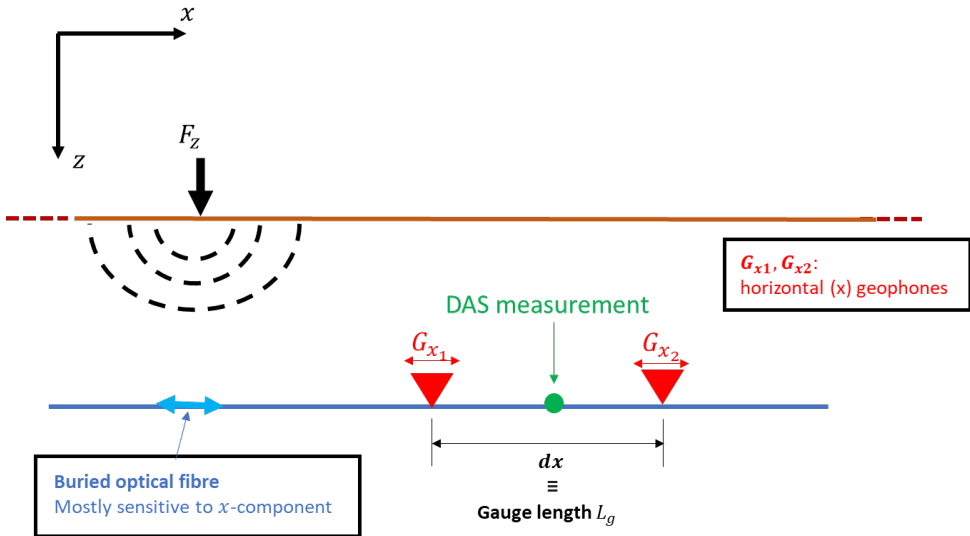

Figure B.1: *An illustration to compare DAS and geophone measurement.*

■ **Phase velocity retrieval**

A variety of methods exist to retrieve a surface wave mode's dispersion curve. The dispersion curve describes the mode's phase velocity as a function of frequency. Often, dispersion curves are estimated by transforming the data into a different (spectral) domain. For example, the recorded data can be transformed from the time-space domain to the phase velocity-frequency [$c - f$; *McMechan and Yedlin*, 1981] domain, to the frequency-wavenumber [$f - k$; *Foti et al.*, 2000] domain, or to the phase-offset [$\phi - x$; *Strobbia and Foti*, 2006] domain. These methods have in common that they rely on the assumption that the subsurface is a stack of horizontal layers. In other words, the subsurface is assumed to be laterally invariant. Consequently, in the case of laterally rapidly varying structure, the retrieved dispersion relation is effectively a (non-exact) average [*Boiero and Socco*, 2010]. In practice, these methods are assumed still to be valid when the subsurface is laterally very smooth.

In case the subsurface is laterally invariant, the relation between the phase (ϕ) and offset (x) will be linear at each discrete frequency (f_i), with the slope coinciding with the wavenumber (k). This can be formulated as [*Strobbia and Foti*, 2006]:

$$\phi(f_i, x) = k(f_i)x + \phi_0(f_i),$$

$$(\text{B.2.2})$$

where ϕ_0 is the phase at the location of the source. Equation (B.2.2) allows the estimation of a wavenumber by means of a least-squares fit of the phase-offset data at each discrete frequency f_i, i.e., using a linear regression [for detailed formulation see *Strobbia and Foti*, 2006]. The estimated wavenumber $(k(f_i))$ can be translated to the frequency-dependent phase velocity $(c(f_i))$ using:

$$c(f_i) = \frac{2\pi f_i}{k(f_i)}, \tag{B.2.3}$$

where $i = 1, 2, ..., N_f$, and N_f denotes the number of discrete frequencies. This approach is referred to as the 'Multi Offset Phase Analysis' [MOPA; *Strobbia and Foti*, 2006; *Vignoli and Cassiani*, 2010].

In the above description, the subsurface is approximated by a single dispersion curve for the whole of x. In the presence of lateral variations, Equation (B.2.2) can be formulated such that the wavenumber k varies as a function of both offset and frequency. That is, $k = k(f_i, x^{(c)})$, where $x^{(c)}$ denotes the center position of a set of adjacent (Fourier transformed) wavefield recordings running from $x^{(c)} - W/2$ to $x^{(c)} + W/2$ (here, W is the spatial window along which $k(f_i, x^{(c)})$ is assumed to be constant). *Vignoli et al.* [2011] "move" this spatial window along the recording line with small steps (i.e., significantly smaller than W). This is done separately for each discrete frequency, allowing W to be frequency dependent [*Vignoli et al.*, 2016]. The wavenumbers are subsequently derived using linear regression according to Equation (B.2.2). These laterally varying wavenumbers are subsequently converted to laterally varying phase velocities $c(f_i, x^{(c)})$ using Equation B.2.3. Since the lateral resolution of the surface waves is directly related to the wavelength [*Barone et al.*, 2021], *Vignoli et al.* [2016] proposed to have the spatial window length W be a function of the wavelength of the surface waves.

In this study, we use the MOPA algorithm of *Vignoli et al.* [2016] to estimate local dispersion curves. Chiefly, this is because of the algorithm's robustness and simplicity. A drawback of the MOPA algorithm, however, is that it can only be applied to a single surface wave mode. Therefore, only one mode will be considered, and the rest of the available surface wave modes and body waves have to be filtered out. Finally, it should be understood that the recovered wavenumbers are associated with the wavefield. That is, they will deviate from the medium's true wavenumber distribution [sometimes referred to as 'structural wavenumbers'; *Wielandt*, 1993], with the discrepancy between the two being larger for more heterogeneous subsurfaces.

■ Transdimensional surface wave tomography

A single dispersion curve, i.e., $c(f_i, x^{(c)})$ for a specific location $x^{(c)}$ (with $i = 1, 2, ..., N_f$), can be "inverted" to recover a (1D) shear-wave velocity profile. Numerous inversion algorithms are described in the literature. Roughly speaking, one can distinguish between linearized algorithms [e.g., *Xia et al.*, 1999b] and nonlinear global search methods. The latter include genetic algorithms [*Yamanaka and Ishida*, 1996], simulated annealing [*Beaty et al.*, 2002], the neighborhood algorithm

[*Wathelet*, 2008], Monte Carlo methdos [*Socco and Boiero*, 2008], particle swarm optimization [*Wilken and Rabbel*, 2012], and a 1D transdimensional algorithm [*Bodin et al.*, 2012a].

In the presence of lateral variations, the dispersion relation varies as a function of location. In that case, the different dispersion curves are often inverted independently using one of the mentioned 1D inversion algorithms [e.g., *Bohlen et al.*, 2004; *Socco et al.*, 2009; *Vignoli et al.*, 2016; *Barone et al.*, 2021], after which the independently inverted 1D profiles are pieced together to obtain a 2D (or 3D) shear-wave velocity pseudo-section (or pseudo-cube). However, by independently inverting the adjacent dispersion curves, lateral correlations in the subsurface structure are ignored [*Zhang et al.*, 2020]. *Socco et al.* [2009] propose to invert all dispersion curves simultaneously to mitigate the solution's non-uniqueness, and retain lateral smoothness. They use a laterally constrained least-squares algorithm in which each 1D model is linked to its neighbors. *Zhang et al.* [2020] invert all dispersion curves simultaneously using a (Bayesian) 3D transdimensional algorithm. In this study, we invert all $c(f_i, x^{(c)})$ simultaneously using a 2D transdimensional algorithm [*Bodin and Sambridge*, 2009]. As such, we retain lateral shear-wave correlations and circumvent (rather arbitrary) smoothing and damping procedures.

The 2D transdimensional tomographic algorithm by *Bodin and Sambridge* [2009] is originally developed for travel time tomography. Here, we modify the algorithm to invert all DAS-derived dispersion curves simultaneously. Our transdimensional algorithm uses a 2D Voronoi tessellation to parameterize the model space ($\mathbf{m}$) in combination with a reversible jump Markov chain. A Voronoi cell is defined by the location of its nucleus and the shear-wave velocity assigned to it. The geometry of each cell is controlled by its neighboring cells. Reversible jump Markov chain Monte Carlo [rjMcMC; *Green*, 1995] allows a variable parameterization of the model space, meaning that the number of Voronoi cells, their locations, and the assigned velocities are all unknowns [*Rahimi Dalkhani et al.*, 2021]. The transdimensional parameterization allows the algorithm to sample the full model space, without the need to introduce any kind of regularization [*Bodin and Sambridge*, 2009].

The rjMcMC algorithm is a Bayesian inference method that aims to sample the posterior probability density of the model parameters given the observed data, $p(\mathbf{m}|\mathbf{d})$. The posterior is proportional to the product of the likelihood $p(\mathbf{d}|\mathbf{m})$ and the prior $p(\mathbf{m})$ [*Bodin and Sambridge*, 2009; *Rahimi Dalkhani et al.*, 2021]:

$$p(\mathbf{m}|\mathbf{d}) \propto p(\mathbf{d}|\mathbf{m})p(\mathbf{m}). \tag{B.2.4}$$

The prior probability distribution, $p(\mathbf{m})$, incorporates all (a priori) known independent information about the model space. Similar to *Bodin and Sambridge* [2009], we consider an uninformative uniform prior for all the model parameters (i.e., number of cells, Voronoi nuclei location, and velocity assigned to each cell).

The likelihood function $p(\mathbf{d}|\mathbf{m})$ plays a fundamental role in the inference of the model space as it provides the probability of the observed laterally varying dispersion

curves given a specific velocity model. It is formulated as:

$$p(\mathbf{d}|\mathbf{m}) = \prod_{i=1}^{N_f} \prod_{j=1}^{N_x} \left(\frac{1}{\sqrt{2\pi}\sigma_{ij}} \exp(-\frac{\left(g_{ij}(\mathbf{m}) - d_{ij}\right)^2}{2\sigma_{ij}^2}) \right), \tag{B.2.5}$$

where N_x is the number of locations $x_j^{(c)}$ for which a dispersion curve is estimated (i.e., $j = 1, 2, ..., N_x$). Data point d_{ij} is the phase velocity at discrete frequency f_i and location $x_j^{(c)}$ (Figure B.3e). The vector $\mathbf{m}$ contains the parameters describing the proposed model. Due to the variable number of Voronoi cells, its length changes while the posterior is being sampled. Furthermore, g_{ij} is the modeled laterally varying phase velocity and σ_{ij} is the data uncertainty or noise level for the phase velocity at the discrete frequency f_i and location $x_j^{(c)}$.

The reversible jump Markov chain draws samples from the posterior distribution by means of a Metropolis-Hasting (MH) algorithm which includes changing the dimension of the model space. Jumping between different dimensions of the model space allows the rjMcMC algorithm to perform a global search and overcome the problem of local minima [*Andrieu et al.*, 1999]. The process starts with some random initial model $\mathbf{m}$. Then, the algorithm draws the next sample of the chain by proposing a new model, $\mathbf{m}'$, based on a known proposal probability function, $q(\mathbf{m}'|\mathbf{m})$, which only depends on the previous state of the model $\mathbf{m}$. The proposed model $\mathbf{m}'$ will be accepted with probability [*Bodin and Sambridge*, 2009]:

$$\alpha(\mathbf{m}'|\mathbf{m}) = min[1, \frac{p(\mathbf{m}')}{p(\mathbf{m})} \frac{p(\mathbf{d}|\mathbf{m}')}{p(\mathbf{d}|\mathbf{m})} \frac{q(\mathbf{m}|\mathbf{m}')}{q(\mathbf{m}'|\mathbf{m})} \times |\mathbf{J}|], \tag{B.2.6}$$

where, $\frac{p(\mathbf{m}')}{p(\mathbf{m})}$ is the prior ratio, $\frac{p(\mathbf{d}|\mathbf{m}')}{p(\mathbf{d}|\mathbf{m})}$ is the likelihood ratio, $\frac{q(\mathbf{m}|\mathbf{m}')}{q(\mathbf{m}'|\mathbf{m})}$ is the proposal ratio, and $\mathbf{J}$ is the Jacobian of transformation from $\mathbf{m}$ to $\mathbf{m}'$ and is needed to account for scale changes involved when the perturbation considers a jump between dimensions [*Green*, 1995].

The acceptance probability, $\alpha(\mathbf{m}'|\mathbf{m})$, is the key to ensuring that the samples will be generated according to the target posterior distribution, $p(\mathbf{m}|\mathbf{d})$ [*Bodin and Sambridge*, 2009]. Similar to *Bodin and Sambridge* [2009], we used four perturbation types to propose a new model ($\mathbf{m}'$) based on the current model ($\mathbf{m}$) including nuclei move, velocity update, birth, and death steps. We followed exactly the same way as *Bodin and Sambridge* [2009] to parametrize the model space and perturb the model space using the four perturbation types. Consequently, the formulas to compute the acceptance probability (Equation B.2.6) are identical to the ones derived by *Bodin and Sambridge* [2009].

It is worth noting that the input data in our case (i.e., laterally varying phase velocities along a 2D line) is different from the travel times used in *Bodin and Sambridge* [2009]. Consequently, a different forward function (g in Equation B.2.5) is necessary to compute the modeled data. For this purpose, we use a MATLAB package developed by *Wu et al.* [2019] using the method proposed in *Buchen and Ben-Hador* [1996]. This algorithm computes the dispersion curve (i.e., phase velocity versus frequency) in a 1D earth model. Therefore, to model the laterally varying

dispersion curves, we take the 1D velocity profile at each location and compute the dispersion curves independently.

B.3   Application to synthetic data

In order to test the proposed workflow, we consider a 2D synthetic model with lateral variation and a low-velocity layer near the surface (Figure B.2a). The wavefield is modeled using a two-dimensional finite-difference elastic wave equation solver [*Thorbecke*, 2017] assuming a free surface at the top of the model and a compressional (p-wave) source type. The source time function is a 12 Hz Ricker wavelet. Since the straight fibers record the radial component of the surface waves, we use the horizontal component of the wavefield recorded at the surface of the synthetic model (Figure B.2b). In this experiment, the recorded surface wave on the horizontal component of the wavefield is the Rayleigh wave. We indicated the fundamental-mode surface wave (R0), higher-modes surface waves (R+), and the direct body wave (DW) on the seismic record in Figure B.2b. The $f - k$ spectrum is shown in Figure B.2c. The fundamental-mode Rayleigh wave is dominant in Figure B.2b-d.
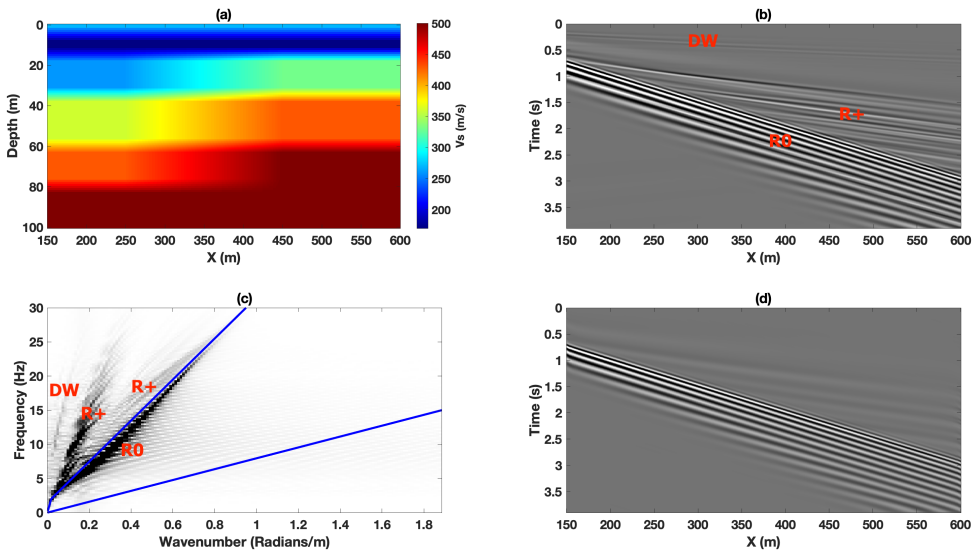
Figure B.2: *Surface wave spectral analysis of a synthetic active seismic record. (a) The prescribed synthetic model. (b) The horizontal component of the wavefield recorded at the surface for a source located at x = 0 m. (c) f − k spectrum. fundamental-mode surface waves (R0), higher-modes surface waves (R+), and direct body waves (DW) are indicated in (b-c). (d) An isolated fundamental-mode is retained after an f-k filter has been applied. The blue lines in (c) represent the corner frequencies of the applied velocity filter.*

■ **Multi Offset Phase Analysis**

To obtain a reliable phase versus offset spectrum that is associated with the fundamental-mode only, we isolate the fundamental-mode (Figure B.2d) by retaining the energy contained by the blue lines in Figure B.2c and muting the rest of the spectrum ($f-k$ filtering). The filtered data, after computation of the inverse transform, is presented in Figure B.2d. Subsequently, each trace of the "cleaned" shot record is transformed to the frequency domain using a Fast Fourier Transform. For each discrete frequency f_i, the phases of the individual traces are unwrapped [e.g., *Weemstra et al.*, 2021], resulting in the $\phi - x$ spectrum. The (unwrapped) phase versus offset is presented for six different frequencies in Figure B.3a.

The retrieved laterally varying dispersion curves using the MOPA are depicted in Figure B.3b for the single shot record of Figure B.2d. Here, we used a spatial window length $W(f_i)$ equal to two wavelengths, where the latter is computed using a reference phase velocity based on the (averaged) phase velocity retrieved through the application of MOPA to the whole shot record. This frequency dependency implies that W decreases with increasing frequency. Linear regression using Equation (B.2.2) for each f_i and $x_j^{(c)}$ separately, subsequently results in the frequency-dependent "local" wavenumbers. These wavenumbers are then transformed into phase velocities using Equation (B.2.3), yielding the set of laterally varying dispersion curves depicted in Figure B.3b.

To improve the quality of the recovered dispersion curves, MOPA is conventionally applied to multiple shots, each located at a different (in-line) position. In this synthetic experiment, we modeled 32 shot records with sources located between 0-150 m and 600-750 m and with a source spacing of 10 m. Additionally, an $f - k$ filter is applied to each (Fourier transformed) shot record to facilitate a reliable phase analysis by isolating the fundamental-mode. Subsequently, laterally varying dispersion curves are estimated through the application of MOPA to each shot record separately. At each position $x_j^{(c)}$, this results in 32 independently estimated dispersion curves. The average of these 32 sections is presented in Figure B.3c. The associated standard deviation is presented in Figure B.3d, which is a measure of the uncertainty of the recovered $c(f_i, x_j^{(c)})$.

Figure B.3e shows the (true) theoretical location-dependent phase velocities as a reference. These are computed by taking the true 1D shear-wave velocity profile at each location and then computing the theoretical dispersion curve using the reduced delta matrix method [*Buchen and Ben-Hador*, 1996; *Wu et al.*, 2019]. Figure B.3c,e show that lower frequencies (less than 3 Hz) and also higher frequencies (higher than 20 Hz) are associated with higher uncertainties and deviate from the theoretical dispersion relation. These are due to the low amplitude of the source time function (i.e., a 12 Hz Ricker) at those frequencies. Additionally, residual higher-modes (visible in Figure B.2d) also affect the quality of the dispersion relation. Finally, the MOPA algorithm does not cover the regions close to the profile ends due to spatial windowing. Since this window length W is larger at lower frequencies, lower frequencies sampled over a shorter spatial interval in Figure B.3b,c.
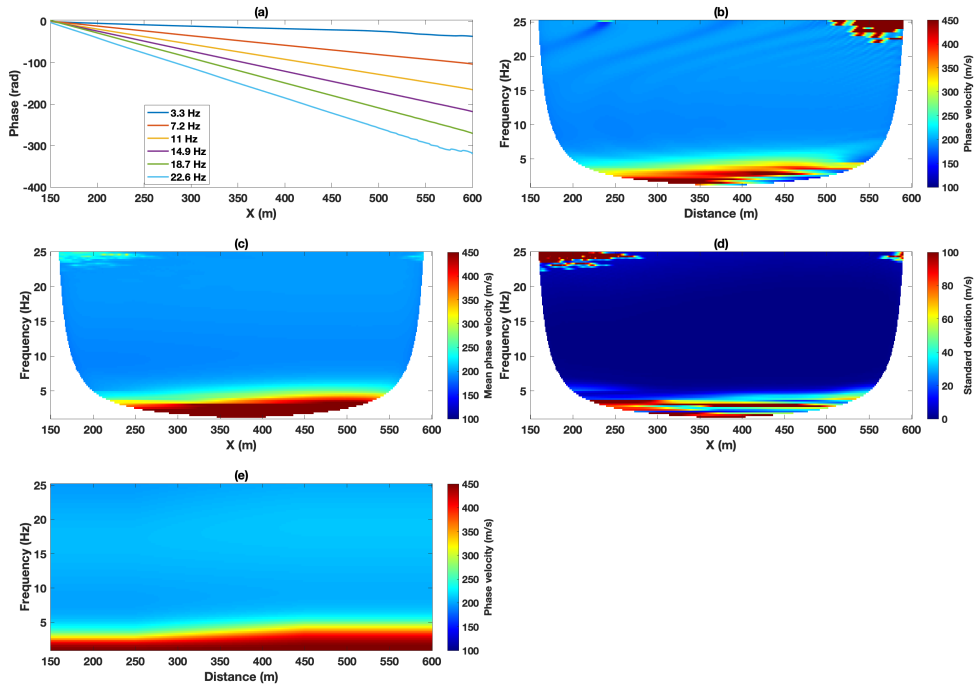
Figure B.3: *Phase velocity retrieval using MOPA: application to synthetic recordings. (a) Phase versus offset for six discrete frequencies of the filtered shot record presented in Figure B.2d. (b) Phase velocities $c(f_i, x_j^{(c)})$ retrieved from one single shot record. (c) Mean local phase velocities retrieved from 32 shots. (d) Standard deviation corresponding to (c). (e) Theoretical (true) laterally varying phase velocities.*

■ Inversion

The recovered local phase velocities are now used in the proposed 2D transdimensional inversion algorithm. We used 20 independent chains to sample the posterior each sampling 700,000 models. The initial model of each chain is generated randomly with a randomly selected number of cells and a randomly chosen location. We only assumed an increasing velocity with depth for the initial model (Figure B.4a). The last collected sample of that chain is shown in Figure B.4b. We discarded the first 200,000 samples as the burn-in period. Then samples are retained at every 100 iterations to avoid collecting correlated samples. Consequently, a total of 100,000 samples are retained and used for the calculation of the posterior mean (Figure B.4c) and the posterior standard deviation (Figure B.4d).

Figure B.4c shows that the proposed algorithm successfully recovered the true shear wave velocity model of Figure B.2a near the surface. In deeper parts of the model, the recovered shear wave velocity is a smoother version of the true velocity model. The uncertainty presented in Figure B.4d is also meaningful by having higher

values in the layer interfaces.
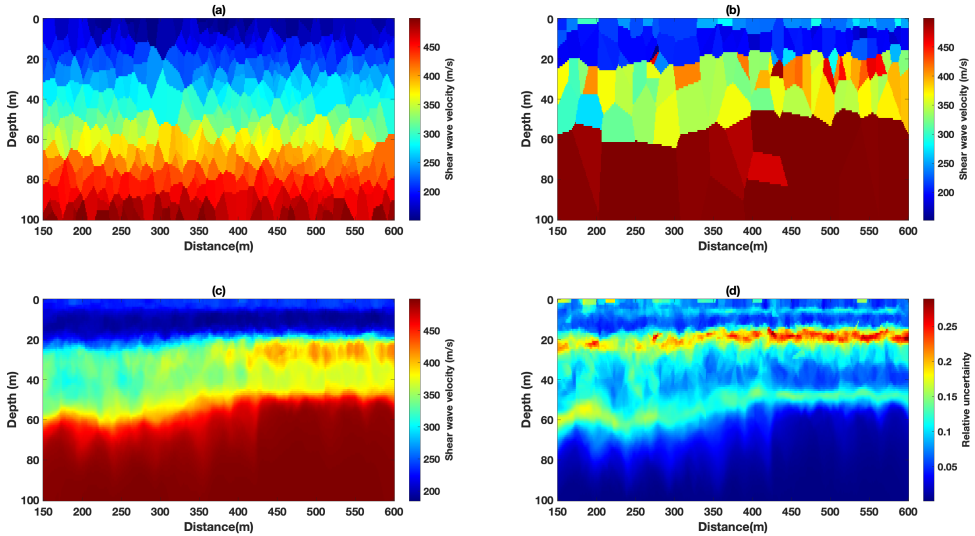
Figure B.4: *(a) A random initial model of a chain. (b) The last collected sample of the chain. (c) The posterior mean of the collected samples from 20 parallel chains. (d) The posterior standard deviation of the retained samples.*

B.4   Application to DAS data recorded near Zuidbroek, Groningen

In this section, we discuss the application of the proposed methodology to a field data set recorded using a straight fiber DAS system. We first introduce the data. Then we recover the local phase velocities followed by a 2D transdimensional inversion. The results are then compared with the shear wave velocity profiles measured at two boreholes along the acquisition line.

■ Data characteristics

The proposed methodology has been applied to data obtained in the area of Groningen in the north of The Netherlands. These data were obtained with fibers as part of a Distributed Acoustic Sensing (DAS) system. Figure 3 shows the acquisition setup of the DAS system. Figure B.5 shows the acquisition setup of the DAS recording system. Several configurations of fibers were used, namely straight and helically wound fibers during the recording [*Al Hasani and Drijkoningen*, 2023], however, we opted for the straight fiber data as it showed the highest sensitivity to the surface waves. The source used is an electrically driven vertical seismic vibrator [*Noorlandt et al.*, 2015] shooting 2 shots per position from x=0 to x=750 every 2 m. The

straight fiber is buried 2m in depth with a length of 450 m from x = 150-600. More information on the acquisition can be found in *Al Hasani and Drijkoningen* [2023].

The receiver spacing of the recordings is 1 m with a gauge length of 2 m. We considered 152 off-end shots on the two sides of the recording line for the application of MOPA. In fact, for the purpose of surface wave analysis and inversion, all shots located at x = 0-150 m and x = 600-750 m are considered in this study, a total of 152 shots.
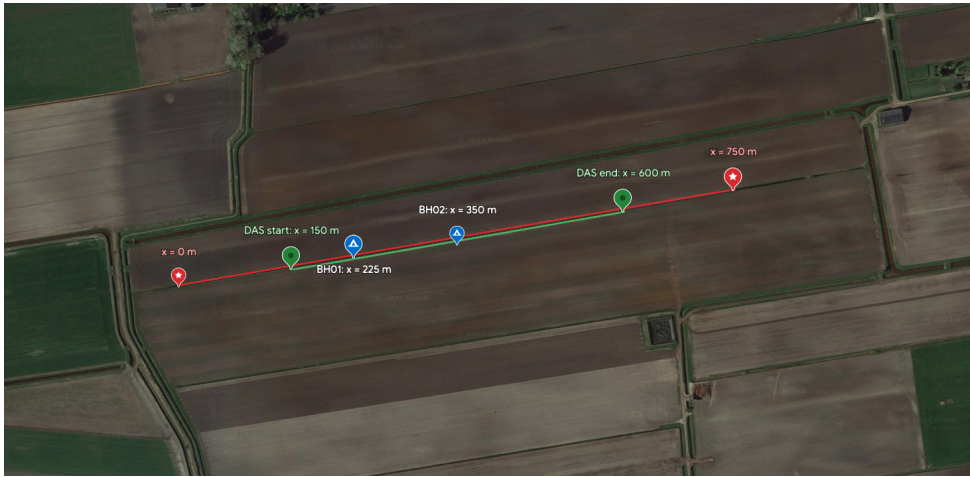
Figure B.5: *The acquisition setup of the recorded DAS data in the Groningen area. The red line shows the source line with a length of 750 m and a source spacing of 2 m. The green line shows the DAS straight fiber buried 2 m in depth and with a length of 450 m. The start of the source line is marked as x = 0 and the end of the source line is marked as x = 750 m. The DAS fiber is also located at x = 150 - 600 m. Two boreholes are also drilled to a depth of 80 m at x = 225 m and x = 350 m to measure the shear-wave velocity directly.*

Figure B.6 shows a sample shot gather of the DAS data recorded at a farm in the Groningen area, the Netherlands. The $f-k$ and $c-f$ spectra are also provided for a better understanding of the data. First, a straight fiber records the radial component of the wave field. Since the vertical source is in line with the fiber (i.e., receivers), the recorded surface wave in the radial direction is the Rayleigh wave. Second, the shot record is dominated by the fundamental-mode Rayleigh wave indicated by **R0**. The fundamental-mode is easily detectable in the frequency range of 4-20 Hz in both $f-k$ and $c-f$ spectra. Third, higher-modes are also clearly visible in both shot records and their corresponding spectra. We have indicated higher-modes by **R+** since more than one higher-mode is visible in the $f-k$ and $c-f$ spectra; it is also difficult to separate them. Finally, the colored lines in the $f-k$ spectra represent phase velocities to design a velocity filter for isolating the fundamental-mode. The velocity lines are also depicted on the $c-f$ spectra for the reader's reference. As you

can see, the red line separating the fundamental-mode from higher-modes is velocity dependent. The $f - k$ spectrum between the blue and the red line is preserved and the rest of the spectrum is filtered out. The filtered record is presented in Figure B.6d representing the fundamental-mode Rayleigh wave. We have applied this velocity filter to all the shots.
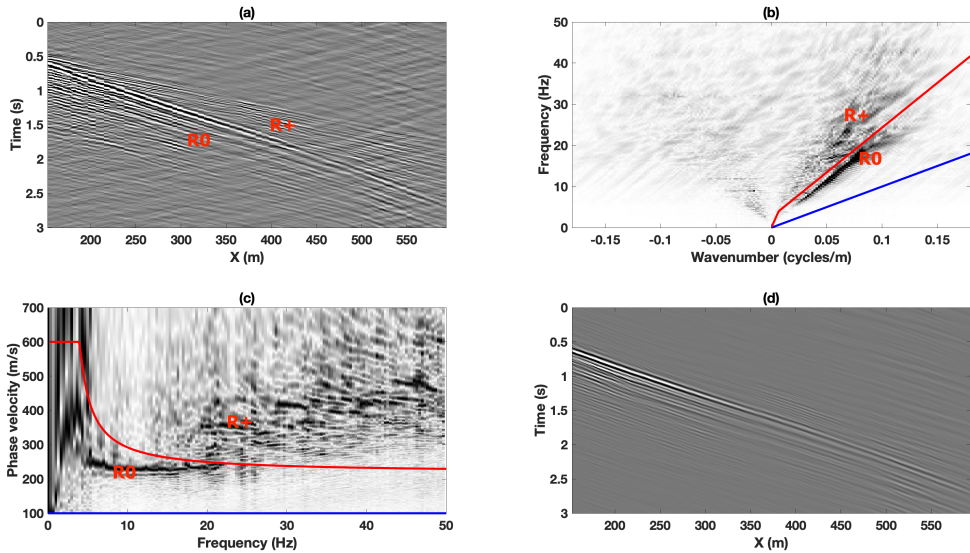
Figure B.6: *A common shot record (a), its corresponding f-k amplitude spectrum (b), and its corresponding dispersion image (c). The source is located at x = 10 m. The fundamental-mode and higher-modes are indicated by R0 and R+, respectively. The blue line indicates the phase velocity of 100 m/s and the red line indicates a frequency-dependent phase velocity between 220-600 m/s. (d) fundamental-mode surface wave shot records corresponding to the shots depicted in (a). An f-k filter is applied to the shot records by keeping the f-k spectrum between the blue and red lines. The rest of the spectrum is filtered out.*

■ **Multi Offset Phase Analysis**

After isolating the fundamental-mode (Figure B.6d), we applied the MOPA algorithm to all 152 off-end shot records of the available DAS data. Figure B.7 shows the results of the MOPA method applied to the field DAS data to retrieve the dispersion curves. The unwrapped phase versus offsets for 7 frequency components of a single shot record (Figure B.6b) are depicted in Figure B.7a. The retrieved laterally varying dispersion curves are presented in Figure B.7b, which are somehow noisy with rather sharp changes. A more smooth and more reliable dispersion curve can be derived by repeating the process for multiple shot records. Figure B.7c presents the average laterally varying dispersion curves derived from 152 shot records. The uncertainty (i.e., standard deviation) is also depicted in Figure B.7d.
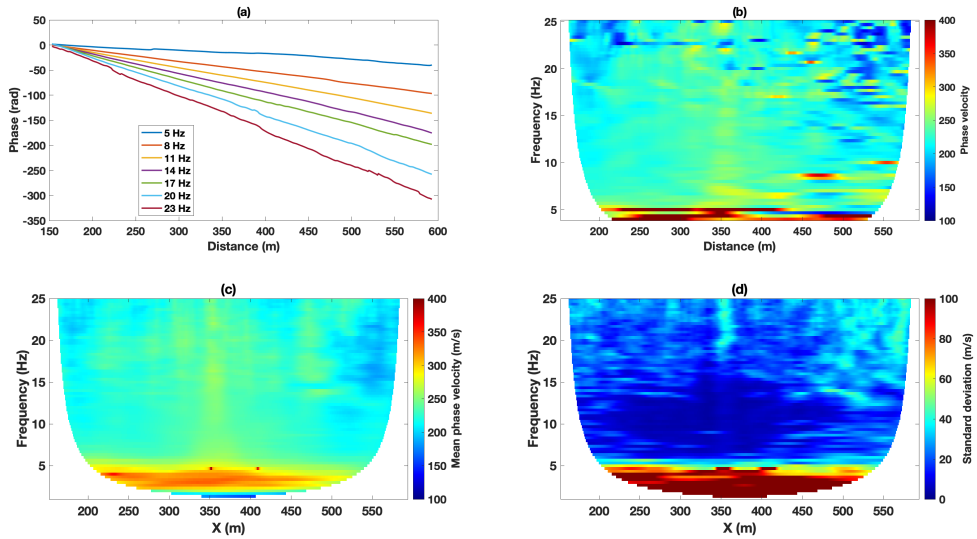
Figure B.7: *MOPA applied to the field DAS data considering the lateral variation of the subsurface. (a) Unwrapped phase versus offset at seven different frequencies (i.e., different colors) for the filtered seismic record depicted in Figure B.6d. (b) laterally varying phase velocity retrieved from the single shot record of Figure B.6d. (c) Mean of the laterally varying dispersion curves retrieved from 152 off-end shots. (d) Standard deviation corresponding to (c).*

■ Prior information

Prior information is the known information from the area of study based on the possible previous studies or the direct measurement of the subsurface properties. In this study, two open boreholes were drilled down to a depth of 80 m, where the shear-wave velocity and p-wave velocity were measured directly using a PS suspension logging tool. In addition to the seismic data, the bulk electrical conductivity and the gamma radiation were also measured. The measured logs are presented in Figure B.8. The main feature observable from the logs is a clear reduction of shear-wave velocity between 10 and 20 m, especially in Figure B.8a. This is due to the higher clay content supported by the conductivity and gamma-ray values having higher values than above and below that layer. In addition, the relatively low electrical conductivity values indicate fresh water and the relatively low gamma ray values indicate a low level of clay content. Consequently, the top 10 m of the subsurface is predominantly sand with fresh water.

This logging information can be used to construct a prior probability distribution for the shear-wave velocity, which is the subject of another study. In this study, we assumed an uninformative uniform prior distribution for the shear-wave velocity with the prior bounds of 50-600 m/s, and we used these logging data to validate our inversion results. Additionally, to compute the surface wave dispersion

(a) BH01

(b) BH02
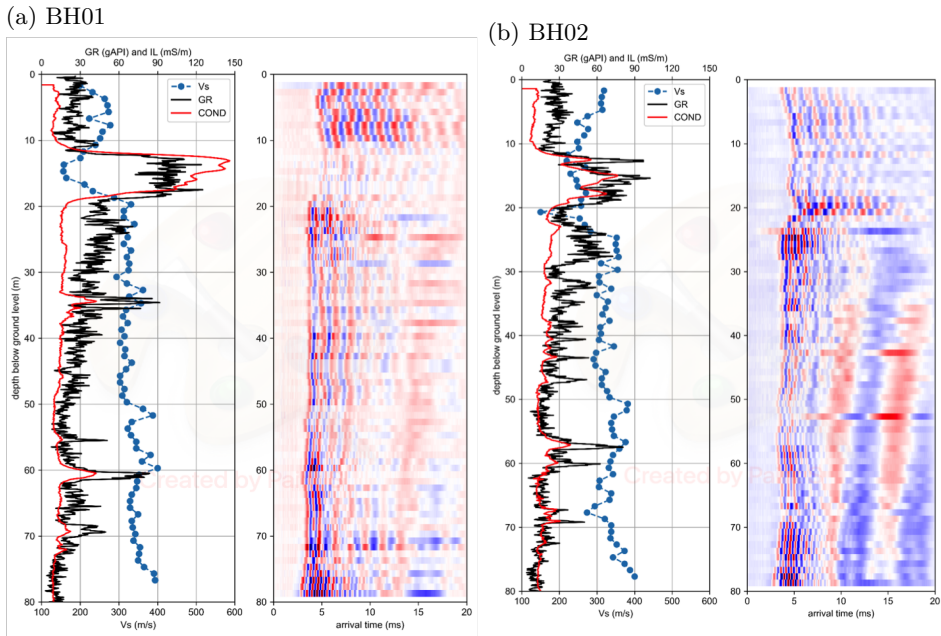
Figure B.8: *The measured Induction-Log readings (IL), Gamma Ray (GR), and shear-wave velocity profile (V_s) together with the far receiver s-wave seismogram of (a) first borehole (BH01) at x = 220 m and (b) second borehole (BH02) at x = 350 m of the recording line.*

curves theoretically, we need the shear-wave velocity (V_s), p-wave velocity(V_p), and density (ρ). However, the shear-wave velocity is mainly controlling the theoretical dispersion curves, and the effect of V_p and ρ is ignored in the literature *Wathelet* [2008]. We used the logging data to get an estimate of the $\dfrac{V_p}{V_s}$ ratio to be used in the theoretical calculation of the dispersion curves. To that end, we first smoothed the shear-wave velocity profile (Figure B.9a) and the compressional-wave velocity profile (Figure B.9b) using a moving average profile. Then, a depth-dependent $\dfrac{V_p}{V_s}$ ratio is computed based on the smoothed blue curves presented in Figure B.9c. During the inversion process, we used a $\dfrac{V_p}{V_s}$ ratio of 5 to relate the shear-wave velocity and the compressional-wave velocity while computing the dispersion curves.

■ **Transdimensional inversion**

The retrieved laterally varying phase velocities (Figure B.7e) are now used in the 2D transdimensional algorithm. We used 20 independent McMC chains running in parallel each sampling 700,000 models. The initial model at each chain is selected
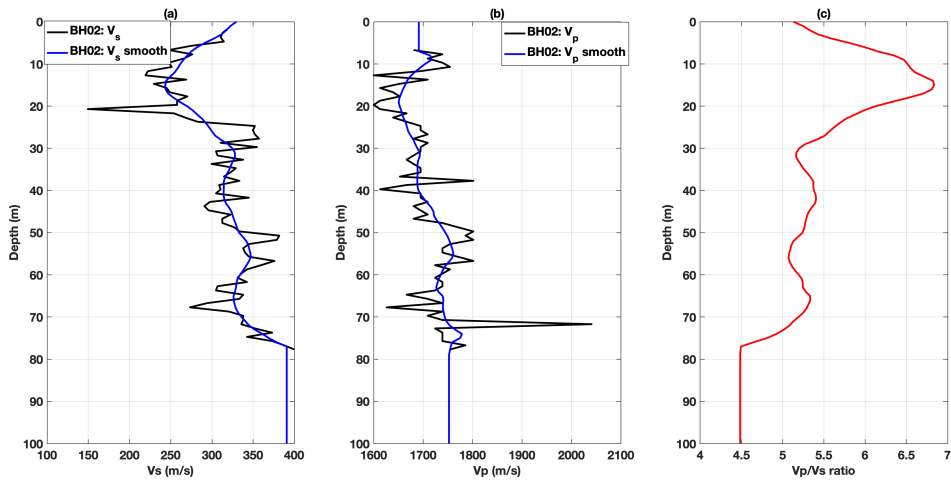
Figure B.9: *shear-wave velocity profile (a) and p-wave velocity profile (b) measured at the second borehole (BH02). The blue curves are the smooth version of the original velocity profiles using a moving average filter. (c) The $\dfrac{V_p}{V_s}$ ratio is computed based on the smooth blue curves.*

randomly with velocity increasing with depth. The first 200,000 samples of each chain are discarded as the burn-in phase. To avoid correlated samples, the samples are retained after every 100 iterations of the McMC. Consequently, a total of 100,000 retained samples are used as the representation of the posterior distribution to compute the posterior mean (i.e., posterior expectation) and standard deviation (i.e., posterior uncertainty).

Figure B.10 presents the recovered shear-wave velocity profile using the 2D transdimensional method. The shear-wave velocity profiles from the well logs are also compared with the transdimensional inverted result. As one can see, the inverted shear-wave velocity is in good agreement with the well log data at the location of the second borehole (i.e., x = 350 m). The inverted result follows the well log data and the main anomalies are resolved. At the location of the first borehole (i.e., x = 220 m), the inverted shear-wave velocity deviates a bit more from the well log data while predicting the low velocity anomaly between the depth of 10-20 m. This deviation at the location of the first borehole is mainly due to the lower quality of the MOPA derived dispersion curves. As one can see in Figure B.7e-f, the retrieved phase velocity at the sides of the model has fewer frequency components and is associated with higher uncertainties.
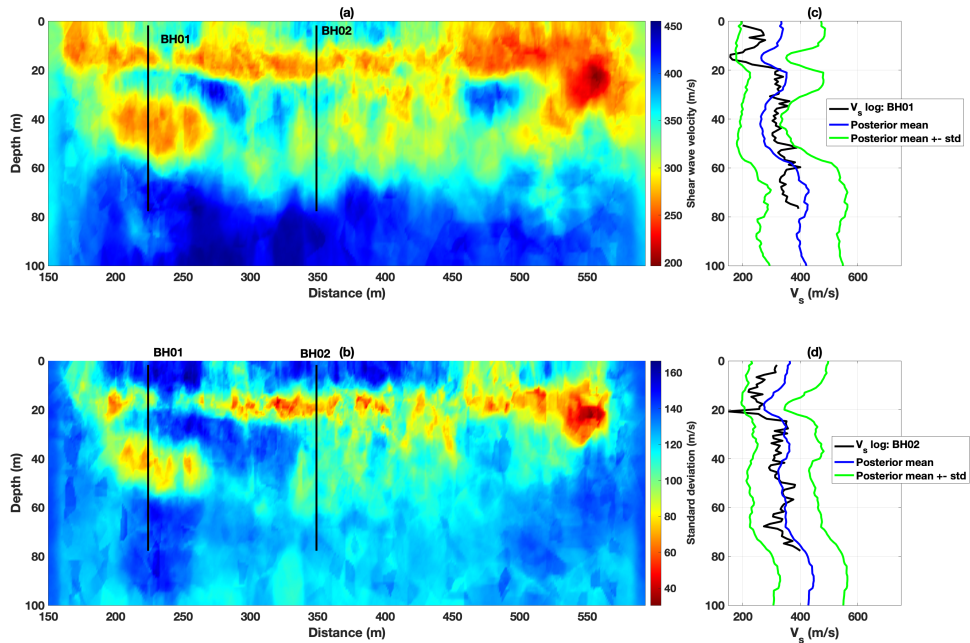
Figure B.10: *2D transdimensional inversion results. (a) Recovered shear-wave velocity 2D section (i.e., posterior mean), (b) recovered model uncertainty (i.e., posterior standard deviation) and comparison with the shear-wave velocity profile available from the first borehole (c) and the second borehole (d).*

B.5   Discussion

There are several points of discussion. First, the agreement between the transdimensional derived shear-wave velocity and the well logs are promising, especially at the location of the second borehole close to the middle of the seismic line. However, at the location of the first borehole where the retrieved phase velocity is missing lower frequencies and associated with higher uncertainties, the results deviate from the more reliable and locally measured log model. This is due to the MOPA algorithm we used in this study. The quality of the dispersion curves at these locations might be improved by the tomography-derived phase velocity retrieval algorithm [*Barone et al.*, 2021].

Second, data uncertainty (σ in Equation B.2.5) plays a crucial role in the convergence of a Bayesian algorithm [*Bodin et al.*, 2012b; *Rahimi Dalkhani et al.*, 2021]. As discussed earlier, the MOPA algorithm we used in this study provides us with an estimate of the data uncertainty (Figure B.3f). In this study, we used this MOPA-derived uncertainty during the McMC sampling of the posterior. However, modeling and other processing errors are also affecting Bayesian inference. Consequently, we suggest further studies to take into account these errors to improve the convergence

of each sampling chain and to enhance the quality of the final inversion result.

Third, the proposed 2D transdimensional algorithm is comparable with the independent 1D inversion of the dispersion curves in terms of computational time This is because in the proposed 2D transdimensional algorithm, at each step of the McMC, we perturb a small portion of the model space. Then, we compute the forward function (i.e., the primary source of the computational demand) only at the updated part of the model space. This reduces the computational time significantly. The added values of the proposed 2D transdimensional scheme are the enhanced lateral correlation and the reduced solution nonuniqueness.

Finally, we assumed a uniform prior whereas we have two boreholes across the line measuring the shear-wave velocity directly. Using this kind of available prior data can improve the inversion result significantly.

B.6   Conclusion

We investigated the potential of straight fiber DAS data in combination with a 2D transdimensional inversion algorithm to recover a 2D reliable shear-wave velocity section. We successfully recovered the laterally varying phase velocities using Multi Offset Phase Analysis. Then, we adopted the 2D transdimensional algorithm to invert all the available laterally varying dispersion curves simultaneously. The recovered shear-wave velocity is smooth with imaging of the lateral variation of the near-surface. The inverted shear-wave velocity section indicates a low-velocity anomaly between 10-20 m depth which is in agreement with the shear-wave velocity logs. The low velocity is due to the high content of clay supported by gamma-ray measurements. In general, the recovered shear-wave velocity section matches the log at the second borehole at 10-65 m depth. Therefore, we were able to retrieve the lateral variability of the subsurface using Rayleigh waves, with a good match with the S-wave logs in two boreholes.

Bibliography

Ajo-Franklin, J. B., S. Dou, N. J. Lindsey, I. Monga, C. Tracy, M. Robertson, V. Rodriguez Tribaldos, C. Ulrich, B. Freifeld, T. Daley, et al. (2019a), Distributed acoustic sensing using dark fiber for near-surface characterization and broadband seismic event detection, *Scientific reports*, *9*(1), 1328.

Ajo-Franklin, J. B., S. Dou, N. J. Lindsey, I. Monga, C. Tracy, M. Robertson, V. R. Tribaldos, C. Ulrich, B. Freifeld, T. Daley, and X. Li (2019b), Distributed acoustic sensing using dark fiber for near-surface characterization and broadband seismic event detection, *Scientific Reports*, *9*(1328), doi:10.1038/s41598-018-36675-8.

Aki, K., and P. G. Richards (2002), *Quantitative Seismology*, University Science Books, Sausalito, California, medium: Hardcover.

Al Hasani, M., and G. Drijkoningen (2023), Experiences with distributed acoustic sensing using both straight and helically wound fibers in surface-deployed cables — a case history in groningen, the netherlands, *GEOPHYSICS*, *88*(6), B369–B380, doi:10.1190/geo2022-0769.1.

Al Hasani, M. A., G. Drijkoningen, and T. Reinsch (2020), Examining directional strain sensitivity of shaped optical fibre embedded in polyurethane strip, arXiv preprint arXiv:2004.07277, doi:10.48550/ARXIV.2004.07277.

Andrieu, C., J. de Freitas, and A. Doucet (1999), Robust full bayesian methods for neural networks, *Advances in neural information processing systems*, *12*.

Baird, A. (2020), Modelling the response of helically wound das cables to microseismic arrivals, pp. 1–5, European Association of Geoscientists and Engineers, EAGE, doi:10.3997/2214-4609.202030019.

Bakku, S. K. (2015), Fracture characterization from seismic measurements in a borehole, *PhD Thesis MIT, USA*, doi:10.1007/s11060-016-2274-y.

Bakulin, A., P. Golikov, R. Smith, K. Erickson, I. Silvestrov, and M. Al-Ali (2017), Smart DAS upholes for simultaneous land near-surface characterization and subsurface imaging, *The Leading Edge*, *36*(12), 1001–1008, doi:10.1190/tle36121001.1.

Barberan, C., C. Allanic, D. Avila, J. Hy-Billiot, A. Hartog, B. Frignet, and G. Lees (2012), Multi-offset seismic acquisition using optical fiber behind tubing, in *74th EAGE Conference and Exhibition incorporating EUROPEC 2012*, pp. 4–7, doi:10.3997/2214-4609.20148798.

Barone, I., J. Boaga, A. Carrera, A. Flores-Orozco, and G. Cassiani (2021), Tackling lateral variability using surface waves: A tomography-like approach, *Surveys in Geophysics*, *42*, 317–338.

Bastianini, F., R. Di Sante, F. Falcetelli, G. Bolognini, and D. Marini (2019), Optical fiber sensing cables for Brillouin-based distributed measurements, *Sensors*, *19*(23), doi:10.3390/s19235172.

Beaty, K. S., D. R. Schmitt, and M. Sacchi (2002), Simulated annealing inversion of multimode rayleigh wave dispersion curves for geological structure, *Geophysical Journal International*, *151*(2), 622–631.

Becker, M. W., C. Ciervo, M. Cole, T. Coleman, and M. Mondanos (2017), Fracture hydromechanical response measured by fiber optic distributed acoustic sensing at millihertz frequencies, *Geophysical Research Letters*, *44*(14), 7295–7302, doi:https://doi.org/10.1002/2017GL073931.

Benioff, H. (1935), A linear strain seismograph, *Bulleting of the Seismological Society of America*, *25*, 283–309.

Bensen, G. D., M. H. Ritzwoller, M. P. Barmin, A. L. Levshin, F. Lin, M. P. Moschetti, N. M. Shapiro, and Y. Yang (2007), Processing seismic ambient noise data to obtain reliable broadband surface wave dispersion measurements, *Geophysical Journal International*, *169*(3), 1239–1260, doi:10.1111/j.1365-246X.2007.03374.x.

Bertholds, A., and R. Dandliker (1988), Determination of the individual strain-optic coefficients in single-mode optical fibres, *Journal of Lightwave Technology*, *6*(1), 17–20, doi:10.1109/50.3956.

Bodin, T., and M. Sambridge (2009), Seismic tomography with the reversible jump algorithm, *Geophysical Journal International*, *178*(3), 1411–1436.

Bodin, T., M. Sambridge, H. Tkalčić, P. Arroucau, K. Gallagher, and N. Rawlinson (2012a), Transdimensional inversion of receiver functions and surface wave dispersion, *Journal of geophysical research: solid earth*, *117*(B2).

Bodin, T., M. Sambridge, N. Rawlinson, and P. Arroucau (2012b), Transdimensional tomography with unknown data noise, *Geophysical Journal International*, *189*(3), 1536–1556.

Bohlen, T., S. Kugler, G. Klein, and F. Theilen (2004), 1.5 d inversion of lateral variation of scholte-wave dispersion, *Geophysics*, *69*(2), 330–344.

Boiero, D., and L. V. Socco (2010), Retrieving lateral variations from surface wave dispersion curves, *Geophysical prospecting*, *58*(6), 977–996.

Bostick III, F. (2000), Field experimental results of three-component fiber-optic seismic sensors, in *SEG Technical Program Expanded Abstracts 2000*, pp. 21–24, Society of Exploration Geophysicists.

Buchen, P., and R. Ben-Hador (1996), Free-mode surface-wave computations, *Geophysical Journal International*, *124*(3), 869–887.

Campillo, M., and A. Paul (2003), Long-range correlations in the diffuse seismic coda, *Science*, *299*(5606), 547–549, doi:10.1126/science.1078551.

Cheng, F., J. B. Ajo-Franklin, and V. R. Tribaldos (2023), High-resolution near-surface imaging at the basin scale using dark fiber and distributed acoustic sensing: Towards site effect estimation in urban environments, *Journal of Geophysical Research: Solid Earth*, p. e2023JB026957.

Cheraghi, S., D. White, K. Harris, and B. Roberts (2018), Initial results of time-lapse processing of VSP geophone and DAS fiber-optic cable at aquistore CO2 injection site, Sask, *80th EAGE Conference & Exhibition*, (June 2018), doi:10.3997/2214-4609.201801472.

Claus, R. O., K. D. Bennett, A. M. Vengsarkar, and K. A. Murphy (1989), Embedded Optical Fiber Sensors for Materials Evaluation, *Journal of Nondestructive Evaluation*, *8*(2).

Cole, S., M. Karrenbach, D. Gunn, and B. Dashwood (2018), Masw analysis of das fiber-optic data for active and passive seismic sources, *2018*(1), 1–5, doi:https://doi.org/10.3997/2214-4609. 201801640.

Correa, J., A. Egorov, K. Tertyshnikov, A. Bona, R. Pevzner, T. Dean, B. Freifeld, and S. Marshall (2017), Analysis of signal to noise and directivity characteristics of DAS VSP at near and far offsets - A CO2CRC Otway Project data example, *The Leading Edge*, *36*(12), 994a1–994a7, doi:10.1190/tle36120994a1.1.

Culshaw, B., and A. Kersey (2008), Fiber-Optic Sensing: A Historical Perspective, *Journal of Lightwave Technology*, *26*(9), 1064–1078, doi:10.1109/JLT.0082.921915.

Curtis, A., P. Gerstoft, H. Sato, R. Snieder, and K. Wapenaar (2006), Seismic interferometry— turning noise into signal, *The Leading Edge*, *25*(9), 1082–1092, doi:10.1190/1.2349814.

Dakin, J. P. (1993), Distributed optical fiber sensors, in *Fibers' 92*, January 1993, p. 102660B, doi:10.1117/12.145193.

Dakin, J. P., and C. Lamb (1990), Distributed fibre optic sensor system. WO Patent 2012030814A3.

Daley, T. M., B. M. Freifeld, J. Ajo-Franklin, S. Dou, R. Pevzner, V. Shulakova, S. Kashikar, D. E. Miller, J. Goetz, J. Henninges, and S. Lueth (2013), Field testing of fiber-optic distributed acoustic sensing (DAS) for subsurface seismic monitoring, *The Leading Edge*, *32*(6), 699–706, doi:10.1190/tle32060699.1.

Daley, T. M., D. E. Miller, K. Dodds, P. Cook, and B. M. Freifeld (2016), Field testing of modular borehole monitoring with simultaneous distributed acoustic sensing and geophone vertical seismic profiles at citronelle, alabama, *Geophysical Prospecting*, *64*, 1318–1334, doi: 10.1111/1365-2478.12324.

Dalkhani, A. R., M. Al Hasani, G. Drijkoningen, and C. Weemstra (2023), Transdimensional surface wave tomography of the near-surface: Application to DAS data, *arXiv preprint arXiv:2304.04384*.

Dean, T., A. Hartog, and B. Frignet (2015a), Seismic without sensors - distributed vibration sensing, in *ASEG Extended Abstracts*, vol. 2015, p. 1, doi:10.1071/ASEG2015ab294.

Dean, T., A. Hartog, B. Papp, and B. Frignet (2015b), Fibre Optic Based Vibration Sensing: Nature of the Measurement, *3rd EAGE Workshop on Borehole Geophysics, Athens, Greece*, (April 2015), BG04.

Dean, T., T. Cuny, and A. H. Hartog (2017), The effect of gauge length on axially incident P-waves measured using fibre optic distributed vibration sensing, *Geophysical Prospecting*, *65*, 184–193, doi:10.1111/1365-2478.12419.

Den Boer, J. J., A. A. Mateeva, J. G. Pearce, J. J. Mestayer, W. Birch, J. L. Lopez, J. C. Hornman, and B. N. Kuvshinov (2012), Detecting Broadside Acoustic Signals with a Fiber Optical Distributed Acoustic Sensing (DAS) Assembly.

Dettmer, J., S. Molnar, G. Steininger, S. E. Dosso, and J. F. Cassidy (2012), Trans-dimensional inversion of microtremor array dispersion data with hierarchical autoregressive error models, *Geophysical Journal International*, *188*(2), 719–734.

Dou, S., N. Lindsey, A. M. Wagner, T. M. Daley, B. Freifeld, M. Robertson, J. Peterson, C. Ulrich, E. R. Martin, and J. B. Ajo-Franklin (2017), Distributed acoustic sensing for seismic monitoring of the near surface: A traffic-noise interferometry case study, *Scientific Reports*, *7*, doi:10.1038/ s41598-017-11986-4.

Draganov, D., X. Campman, J. Thorbecke, A. Verdel, and K. Wapenaar (2009), Reflection images from ambient seismic noise, *GEOPHYSICS*, *74*(5), A63–A67, doi:10.1190/1.3193529.

Farhadiroushan (2010), Method and Apparatus for Optical Sensing. WO Patent 2010136810A2.

Fernández-Ruiz, M. R., L. Costa, and H. F. Martins (2019), Distributed acoustic sensing using chirped-pulse phase-sensitive otdr technology, *Sensors*, *19*(20), doi:10.3390/s19204368.

Foti, S., R. Lancellotta, L. Sambuelli, L. V. Socco, et al. (2000), Notes on fk analysis of surface waves.

Frignet, B. G., and A. H. Hartog (2014), Optical Vertical Seismic Profile on Wireline Cable, in *SPWLA 55th Annual Logging Symposium*, SPWLA, Abu Dhabi.

Frings, J., and T. Walk (2011), Distributed fiber optic sensing enhances pipeline safety and security, *OIL AS European Magazine*, *37*.

Ghalenoei, E., J. Dettmer, M. Y. Ali, and J. W. Kim (2022), Trans-dimensional gravity and magnetic joint inversion for 3-d earth models, *Geophysical Journal International*, *230*(1), 363–376.

Giallorenzi, T., J. Bucaro, A. Dandridge, S. Jr, J. Cole, S. Rashleigh, and R. Priest (1982), Optical fiber sensor technology, *IEEE Journal of Quantum Electronics*, *18*, 626, doi:10.1109/JQE.1982.1071566.

Grandi Karam, S., P. Webster, K. Hornman, P. Lumens, A. Franzen, F. Kindy, M. Chiali, and S. Busaidi (2013), Microseismic Applications using DAS, *4th EAGE Passive Seismic Workshop*, (March 2013), PS02, doi:10.3997/2214-4609.20142338.

Grattan, K. T. V., and B. T. Meggitt (2000), *Optical Fiber Sensor Technology*, Springer US, Boston, MA, doi:10.1007/978-1-4757-6081-1.

Green, P. J. (1995), Reversible jump markov chain monte carlo computation and bayesian model determination, *Biometrika*, *82*(4), 711–732.

Hall, K. W., K. A. Innanen, and D. C. Lawton (2021), Multicomponent DAS sensing: Time-series strain-rate tensor estimation from fiber data, in *SEG International Exposition and Annual Meeting*, p. D011S020R002, SEG.

Hartog, A., and K. Kader (2012), Distributed fiber optic sensor system with improved linearity. US Patent 20120067118A1.

Hartog, A., O. Kotov, and B. Liokumovich (2013), The Optics of Distributed Vibration Sensing, in *EAGE - Second EAGE Workshop on Permanent Reservoir Monitoring*, doi:10.3997/2214-4609.20131301.

Hartog, A., L. Liokumovich, N. Ushakov, O. Kotov, T. Dean, T. Cuny, A. Constantinou, and F. Englich (2018), The use of multi-frequency acquisition to significantly improve the quality of fibre-optic-distributed vibration sensing, *Geophysical Prospecting*, *66*(S1), 192–202, doi:10.1111/1365-2478.12612.

Hartog, A. H. (2017), *An Introduction to Distributed Optical Fibre Sensors*, vol. 136, 23-42 pp., CRC Press, doi:10.1201/9781315119014.

Hartog, A. H., A. P. Leach, and M. P. Gold (1985), Distributed temperature sensing in solid-core fibres, *Electronics Letters*, *21*, 1061–1062.

Hedayati, R., M. J. Mirzaali, L. Vergani, and A. A. Zadpoor (2018), Action-at-a-distance metamaterials: Distributed local actuation through far-field global forces, *APL Materials*, *6*(3), 036,101, doi:10.1063/1.5019782.

Hendi, S., M. Gorjian, G. Bellefleur, C. D. Hawkes, and D. White (2023), Investigation of the effects of surrounding media on the distributed acoustic sensing of a helically wound fibre-optic cable with application to the new afton deposit, British Columbia, *Solid Earth*, *14*, 89–99, doi:10.5194/se-14-89-2023.

Hocker, G. B. (1979), Fiber-optic sensing of pressure and temperature, *Applied Optics*, *18*(9), 1445, doi:10.1364/AO.18.001445.

Hornman, J. C. (2017), Field trial of seismic recording using distributed acoustic sensing with broadside sensitive fibre-optic cables, *Geophysical Prospecting*, *65*(1), 35–46, doi:10.1111/1365-2478.12358.

Innanen, K., and M. Eaid (2018), Towards Discrimination of Elastic Wave Modes with Shaped DAS Fibre-optic Cables, *80th EAGE Conference & Exhibition*, (June 2018), doi:10.3997/2214-4609.201801628.

Innanen, K., D. Lawton, K. Hall, K. Bertram, M. Bertram, and H. Bland (2018), Design and deployment of a prototype multicomponent DAS sensor, *CREWES Research Report*, *30*.

Innanen, K. A. (2017), Determination of seismic tensor strain from hwc-das cable with arbitrary and nested-helix winds, in *SEG 88th Annual Meeting*, vol. 1, pp. 926–930.

Innanen, K. A., D. Lawton, K. Hall, K. L. Bertram, M. B. Bertram, and H. C. Bland (2019), Design and deployment of a prototype multicomponent distributed acoustic sensing loop array, in *SEG International Exposition and Annual Meeting*, p. D023S007R002, SEG.

James, S. R., H. A. Knox, L. Preston, J. M. Knox, M. C. Grubelich, D. K. King, J. B. Ajo-Franklin, T. C. Johnson, and J. P. Morris (2017), Fracture detection and imaging through relative seismic velocity changes using distributed acoustic sensing and ambient seismic noise, *The Leading Edge*, *36*(12), 1009–1017, doi:10.1190/tle36121009.1.

Jin, G., and B. Roy (2017), Hydraulic-fracture geometry characterization using low-frequency DAS signal, *The Leading Edge*, *36*(12), 975–980, doi:10.1190/tle36120975.1.

Jin, G., V. Kazei, A. Lellouch, W. Li, A. Titov, and V. R. Tribaldos (2023), Distributed acoustic sensing in geophysics — introduction, *GEOPHYSICS*, *88*(6), WCi–WCii, doi:10.1190/geo2023-0919-spseintro.1.

Johannessen, K., B. Drakeley, and M. Farhadiroushan (2012), Distributed acoustic sensing-a new way of listening to your well/reservoir, in *SPE Intelligent Energy International*, OnePetro.

Jousset, P., T. Reinsch, T. Ryberg, H. Blanck, A. Clarke, R. Aghayev, G. P. Hersir, J. Henninges, M. Weber, and C. M. Krawczyk (2018), Dynamic strain determination using fibre-optic cables allows imaging of seismological and structural features, *Nature Communications*, *9*(1), doi:10.1038/s41467-018-04860-y.

Juarez, J. C., E. W. Maier, K. N. Choi, and H. F. Taylor (2005), Distributed fiber-optic intrusion sensor system, *Journal of Lightwave Technology*, *23*(6), 2081–2087, doi:10.1109/JLT.2005.849924.

Karrenbach, M., S. Cole, A. Ridge, K. Boone, D. Kahn, J. Rich, K. Silver, and D. Langton (2019), Fiber-optic distributed acoustic sensing of microseismicity, strain and temperature during hydraulic fracturing, *Geophysics*, *84*(1), D11–D23, doi:10.1190/geo2017-0396.1.

KNMI (2022), Knmi seismic and acoustic data tools, `http://rdsa.knmi.nl/dataportal`, accessed: 01-12-2022.

Kuvshinov, B. N. (2016), Interaction of helically wound fibre-optic cables with plane seismic waves, *Geophysical Prospecting*, *64*(3), 671–688, doi:10.1111/1365-2478.12303.

Lancelle, C. E., J. A. Baldwin, N. Lord, D. Fratta, A. Chalari, and H. F. Wang (2021), Using distributed acoustic sensing (das) for multichannel analysis of surface waves (masw), *Distributed Acoustic Sensing in Geophysics: Methods and Applications*, pp. 213–228.

Li, C., J. Tang, Y. Jiang, C. Cheng, L. Cai, and M. Yang (2020), An enhanced distributed acoustic sensor with large temperature tolerance based on ultra-weak fiber bragg grating array, *IEEE Photonics Journal*, *12*(4), 1–11, doi:10.1109/JPHOT.2020.3015262.

Li, D. (2006), Strain transferring analysis of fiber Bragg grating sensors, *Optical Engineering*, *45*(2), 024,402, doi:10.1117/1.2173659.

Li, H.-N., G.-D. Zhou, . L. Ren, and D.-S. Li (2009), Strain transfer coefficient analyses for embedded fiber bragg grating sensors in different host materials, *Journal of Engineering Mechanics*, doi:10.1061/ASCE0733-93992009135:121343.

Lindsey, N. J., E. R. Martin, D. S. Dreger, B. Freifeld, S. Cole, S. R. James, B. L. Biondi, and J. B. Ajo-Franklin (2017), Fiber-optic network observations of earthquake wavefields, *Geophysical Research Letters*, *44*(23), 11,792–11,799, doi:10.1002/2017GL075722.

Lindsey, N. J., T. C. Dawe, and J. B. Ajo-Franklin (2019), Illuminating seafloor faults and ocean dynamics with dark fiber distributed acoustic sensing, *Science*, *366*(6469), 1103–1107.

Lindsey, N. J., H. Rademacher, and J. B. Ajo-Franklin (2020), On the broadband instrument response of fiber-optic das arrays, *Journal of Geophysical Research: Solid Earth*, *125*, doi:10.1029/2019JB018145.

Lumens, P. (2014), Fibre-optic sensing for application in oil and gas wells, Ph.D. thesis, Eindhoven University of Technology, doi:10.6100/IR769555.

Luo, Y., J. Xia, J. Liu, Y. Xu, and Q. Liu (2008), Generation of a pseudo-2d shear-wave velocity section by inversion of a series of 1d dispersion curves, *Journal of Applied Geophysics*, *64*(3-4), 115–124.

Maraschini, M., and S. Foti (2010), A Monte Carlo multimodal inversion of surface waves, *Geophysical Journal International*, *182*(3), 1557–1566, doi:10.1111/j.1365-246X.2010.04703.x.

Masoudi, A., and T. Newson (2017a), High frequency distributed optical fibre dynamic strain sensing: A review, doi:10.3997/2214-4609.201700150.

Masoudi, A., and T. P. Newson (2016), Contributed Review: Distributed optical fibre dynamic strain sensing, *Review of Scientific Instruments*, *87*(1), 011,501, doi:10.1063/1.4939482.

Masoudi, A., and T. P. Newson (2017b), High spatial resolution distributed optical fiber dynamic strain sensor with enhanced frequency and strain resolution, *Optics Letters*, *42*(2), 290, doi:10.1364/OL.42.000290.

Mateeva, A., J. Lopez, H. Potters, J. Mestayer, B. Cox, D. Kiyashchenko, P. Wills, S. Grandi, K. Hornman, B. Kuvshinov, W. Berlang, Z. Yang, and R. Detomo (2014), Distributed acoustic sensing for reservoir monitoring with vertical seismic profiling, *Geophysical Prospecting*, *62*(4), 679–692, doi:10.1111/1365-2478.12116.

Mateeva, A., J. Lopez, D. Chalenski, M. Tatanova, P. Zwartjes, Z. Yang, S. Bakku, K. de Vos, and H. Potters (2017), 4D DAS VSP as a tool for frequent seismic monitoring in deep water, *The Leading Edge*, *36*(12), 995–1000, doi:10.1190/tle36120995.1.

McMechan, G. A., and M. J. Yedlin (1981), Analysis of dispersive waves by wave field transformation, *Geophysics*, *46*(6), 869–874.

Mestayer, J., B. Cox, P. Wills, D. Kiyashchenko, J. Lopez, M. Costello, S. Bourne, G. A. Ugueto, R. Lupton, G. Solano, D. Hill, and A. Lewis (2011), Field trials of Distributed Acoustic Sensing for geophysical monitoring, *SEG San Antonio 2011 Annual Meeting*, pp. 4253–4257.

Michel, Y. P., M. Lucci, M. Casalboni, P. Steglich, and S. Schrader (2015), Mechanical characterisation of the four most used coating materials for optical fibres, in *2015 International Conference on Photonics, Optics and Laser Technology (PHOTOPTICS)*, vol. 1, pp. 91–95.

Mitschke, F. (2010), *Fiber Optics*, vol. 80, Springer Berlin Heidelberg, Berlin, Heidelberg, doi: 10.1007/978-3-642-03703-0.

Molenaar, M. M., D. J. Hill, P. Webster, E. Fidan, and B. Birch (2012), First downhole application of distributed acoustic sensing for hydraulic-fracturing monitoring and diagnostics, *SPE Drilling & Completion*, *27*(01), 32–38.

Muanenda, Y., C. J. Oton, and F. Di Pasquale (2019), Application of raman and brillouin scattering phenomena in distributed optical fiber sensing, *Frontiers in Physics*, doi:10.3389/fphy.2019.00155.

Nayak, A., J. Ajo-Franklin, et al. (2021a), Distributed acoustic sensing using dark fiber for array detection of regional earthquakes, *Seismological Research Letters*, *92*(4), 2441–2452.

Nayak, A., J. Ajo-Franklin, et al. (2021b), Measurement of surface-wave phase-velocity dispersion on mixed inertial seismometer–distributed acoustic sensing seismic noise cross-correlations, *Bulletin of the Seismological Society of America*, *111*(6), 3432–3450.

Neducza, B. (2007), Stacking of surface waves, *Geophysics*, *72*(2), V51–V58.

Niklès, M., L. Thévenaz, and P. A. Robert (1996), Simple distributed fiber sensor based on Brillouin gain spectrum analysis, *Optics Letters*, *21*(10), 758, doi:10.1364/OL.21.000758.

Niklès, M., L. Thévenaz, and P. A. Robert (1997), Brillouin gain spectrum characterization in single-mode optical fibers, *Journal of Lightwave Technology*, *15*(10), 1842–1851, doi:10.1109/50.633570.

Ning, I. L. C., and P. Sava (2018a), Multicomponent distributed acoustic sensing: concept and theory, *GEOPHYSICS*, *83*(2), P1–P8, doi:10.1190/geo2017-0327.1.

Ning, I. L. C., and P. Sava (2018b), High-resolution multi-component distributed acoustic sensing, *Geophysical Prospecting*, *66*, 1111–1122, doi:10.1111/1365-2478.12634.

Noorlandt, R., G. Drijkoningen, J. Dams, and R. Jenneskens (2015), A seismic vertical vibrator driven by linear synchronous motors, *Geophysics*, *80*(2), EN57–EN67, doi:10.1190/geo2014-0295.1.

Nöther, N. (2010), Distributed Fiber Sensors in River Embankments: Advancing and Implementing the Brillouin Optical Frequency Domain Analysis, Ph.D. thesis, Technische Universität Berlin.

Olafsdottir, E. A., B. Bessason, and S. Erlingsson (2018), Combination of dispersion curves from masw measurements, *Soil Dynamics and Earthquake Engineering*, *113*, 473–487, doi:https://doi.org/10.1016/j.soildyn.2018.05.025.

Pak, Y. E. (1992), Longitudinal shear transfer in fiber optic sensors, *Smart Mater. Strucl*, *1*, 57–62.

Papp, B., D. Donno, J. E. Martin, and A. H. Hartog (2017), A study of the geophysical response of distributed fibre optic acoustic sensors through laboratory-scale experiments, *Geophysical Prospecting*, *65*(5), 1186–1204, doi:10.1111/1365-2478.12471.

Park, C. B., R. D. Miller, and J. Xia (1999a), Multichannel analysis of surface waves, *GEOPHYSICS*, *64*(3), 800–808, doi:10.1190/1.1444590.

Park, C. B., R. D. Miller, and J. Xia (1999b), Multichannel analysis of surface waves, *Geophysics*, *64*(3), 800–808.

Park, C. B., R. D. Miller, and J. Xia (2005), *Imaging dispersion curves of surface waves on multi-channel record*, pp. 1377–1380, SEG, doi:10.1190/1.1820161.

Park, C. B., R. D. Miller, J. Xia, and J. Ivanov (2007), Multichannel analysis of surface waves (masw)—active and passive methods, *The Leading Edge*, *26*(1), 60–64, doi:10.1190/1.2431832.

Parker, T., S. Shatalin, and M. Farhadiroushan (2014), Distributed acoustic sensing–a new tool for seismic applications, *first break*, *32*(2).

Paschott, R. (2012), article on 'fibers', `https://www.rp-photonics.com/fibers.html`, accessed: 06-09-2023.

Paschotta, R. (2008), *Field Guide to Optical Fiber Technology*, vol. 3, 52–55 pp., SPIE, doi: 10.1002/opph.201190194.

Pastor-Graells, J., H. F. Martins, A. Garcia-Ruiz, S. Martin-Lopez, and M. Gonzalez-Herraez (2016), Single-shot distributed temperature and strain tracking using direct detection phase-sensitive OTDR with chirped pulses, *Optics Express*, *24*(12), 13,121, doi:10.1364/OE.24.013121.

Pastor-Graells, J., J. Nuno, M. R. Fernandez-Ruiz, A. Garcia-Ruiz, H. F. Martins, S. Martin-Lopez, and M. Gonzalez-Herraez (2017), Chirped-Pulse Phase-Sensitive Reflectometer Assisted by First-Order Raman Amplification, *Journal of Lightwave Technology*, *35*(21), 4677–4683, doi:10.1109/JLT.2017.2756558.

Pirogova, A., R. Pevzner, B. Gurevich, S. Glubokovskikh, and K. Tertyshnikov (2019), Multiwell study of seismic attenuation at the CO2CRC otway project geosequestration site: Comparison of amplitude decay, centroid frequency shift and 1D waveform inversion methods, *Geophysical Prospecting*, *67*(7), 1778–1797, doi:https://doi.org/10.1111/1365-2478.12796.

Posey, R., G. Johnson, and S. Vohra (2000), Strain sensing based on coherent Rayleigh scattering in an optical fibre, *Electronics Letters*, *36*(20), 1688, doi:10.1049/el:20001200.

Qu, L., J. Dettmer, K. Hall, K. A. Innanen, M. Macquet, and D. C. Lawton (2023), Trans-dimensional inversion of multimode seismic surface wave data from a trenched distributed acoustic sensing survey, *Geophysical Journal International*, p. ggad112.

Rahimi Dalkhani, A., X. Zhang, and C. Weemstra (2021), On the potential of 3d transdimensional surface wave tomography for geothermal prospecting of the reykjanes peninsula, *Remote Sensing*, *13*(23), 4929.

Reinsch, T., T. Thurley, and P. Jousset (2017), On the mechanical coupling of a fiber optic cable used for distributed acoustic/vibration sensing applications - A theoretical consideration, *Measurement Science and Technology*, *28*(12), doi:10.1088/1361-6501/AA8BA4.

Reinsch, T., P. Jousset, and C. M. Krawczyk (2021), *Fiber Optic Distributed Strain Sensing for Seismic Applications*, pp. 379–383, Springer International Publishing, Cham, doi:10.1007/978-3-030-58631-7_284.

Reisplanner (2023), Reisplanner trein, `https://treinposities.nl/reisplanner/verbindingen/?frow[van_station]=Zuidbroek&frow[naar_station]=Veendam&frow[via_station]=&frow[datum]=2023-12-18&frow[tijd]=23:46&frow[welketijd]=v`, accessed: 19-12-2023.

Schaefer, J. F., L. Boschi, and E. Kissling (2011), Adaptively parametrized surface wave tomography: methodology and a new model of the European upper mantle, *Geophysical Journal International*, *186*(3), 1431–1453, doi:10.1111/j.1365-246X.2011.05135.x, publisher: Blackwell Publishing Ltd.

Schroeder, J. (1980), Brillouin scattering and pockels coefficients in silicate glasses, *Journal of Non-Crystalline Solids*, *40*(1), 549–566, doi:https://doi.org/10.1016/0022-3093(80)90129-5, proceedings of the Fifth University Conference on Glass Science.

Shan, Y., W. Ji, X. Dong, L. Cao, M. Zabihi, Q. Wang, Y. Zhang, and X. Zhang (2019), An enhanced distributed acoustic sensor based on uwfbg and self-heterodyne detection, *Journal of Lightwave Technology*, *37*(11), 2700–2705.

Shapiro, N. M., and M. Campillo (2004), Emergence of broadband rayleigh waves from correlations of the ambient seismic noise, *Geophysical Research Letters*, *31*(7), doi:https://doi.org/10.1029/2004GL019491.

Shatalin, S., T. Parker, and M. Farhadiroushan (2021), *High Definition Seismic and Microseismic Data Acquisition Using Distributed and Engineered Fiber Optic Acoustic Sensors*, chap. 1, pp. 1–32, American Geophysical Union (AGU), doi:https://doi.org/10.1002/9781119521808.ch1.

Socco, L. V., and D. Boiero (2008), Improved monte carlo inversion of surface wave data, *Geophysical Prospecting*, *56*(3), 357–371.

Socco, L. V., D. Boiero, S. Foti, and R. Wisén (2009), Laterally constrained inversion of ground roll from seismic reflection records, *Geophysics*, *74*(6), G35–G45.

Socco, L. V., S. Foti, and D. Boiero (2010), Surface-wave analysis for building near-surface velocity models—established approaches and new perspectives, *Geophysics*, *75*(5), 75A83–75A102.

Song, X., and H. Gu (2007), Utilization of multimode surface wave dispersion for characterizing roadbed structure, *Journal of Applied Geophysics*, *63*(2), 59–67, doi:https://doi.org/10.1016/j.jappgeo.2007.04.001.

Song, Z., X. Zeng, C. H. Thurber, H. F. Wang, and D. Fratta (2018), Imaging shallow structure with active-source surface wave signal recorded by distributed acoustic sensing arrays, *Earthquake Science*, *31*(4), 208–214, doi:10.29382/eqs-2018-0208-4.

Spica, Z. J., M. Perton, E. R. Martin, G. C. Beroza, and B. Biondi (2020), Urban seismic site characterization by fiber-optic seismology, *Journal of Geophysical Research: Solid Earth*, *125*(3), e2019JB018,656, doi:10.1029/2019JB018656, e2019JB018656 10.1029/2019JB018656.

Spikes, K. T., N. Tisato, T. E. Hess, and J. W. Holt (2019), Comparison of geophone and surface-deployed distributed acoustic sensing seismic data, *Geophysics*, *84*, A25–A29, doi:10.1190/geo2018-0528.1.

Strobbia, C., and S. Foti (2006), Multi-offset phase analysis of surface wave data (mopa), *Journal of Applied Geophysics*, *59*(4), 300–313.

Sun, L., H. Hao, B. Zhang, X. Ren, and J. Li (2016), Strain transfer analysis of embedded fiber Bragg grating strain sensor, *Journal of Testing and Evaluation*, *44*(6), 2312–2320, doi:10.1520/JTE20140388.

Takekawa, J., H. Mikada, S. Xu, M. Uno, S. Kamei, K. Kishida, D. Azuma, M. Aoyanagi, N. Tanaka, and H. Ichikawa (2022), A new das sensor prototype for multicomponent seismic data, *The Leading Edge*, *41*(5), 338–346.

Taylor, H. F., and C. E. Lee (1991), Method For Fiber Optic Intrusion Sensing. US Patent 5194847A.

Thorbecke, J. (2017), 2d finite-difference wavefield modelling, *Delft University*.

Thorbecke, J. W., and D. Draganov (2011), Finite-difference modeling experiments for seismic interferometry, *Geophysics*, *76*(6), H1–H18, doi:10.1190/geo2010-0039.1.

Tribaldos, V. R., J. B. Ajo-Franklin, S. Dou, N. J. Lindsey, C. Ulrich, M. Robertson, B. M. Freifeld, T. Daley, I. Monga, and C. Tracy (2021), *Surface Wave Imaging Using Distributed Acoustic Sensing Deployed on Dark Fiber*, chap. 15, pp. 197–212, American Geophysical Union (AGU), doi:https://doi.org/10.1002/9781119521808.ch15.

Udd, E. (1995), An overview of fiber-optic sensors, *Review of Scientific Instruments*, *66*, 4015, doi:10.1063/1.1145411.

Udd, E., and W. B. Spillman (2011), *Fiber Optic Sensors*, John Wiley & Sons, Inc., Hoboken, NJ, USA, doi:10.1002/9781118014103.

Urosevic, M., A. Bona, S. Ziramov, R. Martin, J. Dwyer, and A. Foley (2018), Reflection Seismic with DAS, Why and Where?, *80th EAGE Conference & Exhibition*, *1*(September 2018), doi:10.3997/2214-4609.201802736.

van Ginkel, J., E. Ruigrok, and R. Herber (2019), Assessing soil amplifications in groningen, the netherlands, *First Break*, *37*(10), 33–38.

van Thienen-Visser, K., and J. N. Breunese (2015), Induced seismicity of the groningen gas field: History and recent developments, *The Leading Edge*, *34*(6), 664–671, doi:10.1190/tle34060664.1.

Vantassel, J. P., B. R. Cox, P. G. Hubbard, and M. Yust (2022a), Extracting high-resolution, multi-mode surface wave dispersion data from distributed acoustic sensing measurements using the multichannel analysis of surface waves, *Journal of Applied Geophysics*, *205*, 104,776, doi: https://doi.org/10.1016/j.jappgeo.2022.104776.

Vantassel, J. P., B. R. Cox, P. G. Hubbard, and M. Yust (2022b), Extracting high-resolution, multi-mode surface wave dispersion data from distributed acoustic sensing measurements using the multichannel analysis of surface waves, *Journal of Applied Geophysics*, *205*, 104,776.

Velázquez-Benítez, A., J. Antonio-López, J. Alvarado Zacarias, N. Fontaine, R. Ryf, H. Chen, J. Hernández-Cordero, P. Sillard, C. Okonkwo, S. Leon-Saval, and R. Amezcua-Correa (2018), Scaling photonic lanterns for space-division multiplexing, *Scientific Reports*, *8*, doi:10.1038/s41598-018-27072-2.

Vermeer, G. J. (1990), *Seismic wavefield sampling*, Society of Exploration Geophysicists and Shell Research BV.

Vignoli, G., and G. Cassiani (2010), Identification of lateral discontinuities via multi-offset phase analysis of surface wave data, *Geophysical Prospecting*, *58*(3), 389–413.

Vignoli, G., C. Strobbia, G. Cassiani, and P. Vermeer (2011), Statistical multioffset phase analysis for surface-wave processing in laterally varying media, *Geophysics*, *76*(2), U1–U11.

Vignoli, G., I. Gervasio, G. Brancatelli, J. Boaga, B. Della Vedova, and G. Cassiani (2016), Frequency-dependent multi-offset phase analysis of surface waves: an example of high-resolution characterization of a riparian aquifer, *Geophysical Prospecting*, *64*(1), 102–111.

Waagaard, O. H., E. Rønnekleiv, A. Haukanes, F. Stabo-Eeg, D. Thingbø, S. Forbord, S. E. Aasen, and J. K. Brenne (2021), Real-time low noise distributed acoustic sensing in 171 km low loss fiber, *OSA Continuum*, *4*(2), 688–701, doi:10.1364/OSAC.408761.

Wang, Z., B. Lu, Q. Ye, and H. Cai (2020), Recent progress in distributed fiber acoustic sensing with ϕ-otdr, *Sensors*, *20*(22), 6594.

Wapenaar, K., D. Draganov, R. Snieder, X. Campman, and A. Verdel (2010), Tutorial on seismic interferometry: Part 1 - basic principles and applications, *GEOPHYSICS*, *75*(5), 75A195–75A209, doi:10.1190/1.3457445.

Wathelet, M. (2008), An improved neighborhood algorithm: parameter conditions and dynamic scaling, *Geophysical Research Letters*, *35*(9).

Weemstra, C., J. I. de Laat, A. Verdel, and P. Smets (2021), Systematic recovery of instrumental timing and phase errors using interferometric surface waves retrieved from large-N seismic arrays, *Geophysical Journal International*, *224*, 1028–1055, doi:10.1093/gji/ggaa504, publisher: Oxford University Press.

White, D., G. Bellefleur, K. Dodds, and Z. Movahedzadeh (2022), Toward improved distributed acoustic sensing sensitivity for surface-based reflection seismics: Configuration tests at the aquistore co2 storage site, *Geophysics*, *87*(2), P1–P14, doi:10.1190/geo2021-0120.1.

Wielandt, E. (1993), Propagation and structural interpretation of non-plane waves, *Geophysical Journal International*, *113*(1), 45–53, doi:10.1111/j.1365-246X.1993.tb02527.x, iSBN: 0956-540X.

Wilken, D., and W. Rabbel (2012), On the application of particle swarm optimization strategies on scholte-wave inversion, *Geophysical Journal International*, *190*(1), 580–594.

Wu, D., X. Wang, Q. Su, and T. Zhang (2019), A matlab package for calculating partial derivatives of surface-wave dispersion curves by a reduced delta matrix method, *Applied Sciences*, *9*(23), 5214.

Xia, J., R. D. Miller, and C. B. Park (1999a), Estimation of near-surface shear-wave velocity by inversion of Rayleigh waves, *GEOPHYSICS*, *64*(3), 691–700, doi:10.1190/1.1444578.

Xia, J., R. D. Miller, and C. B. Park (1999b), Estimation of near-surface shear-wave velocity by inversion of rayleigh waves, *Geophysics*, *64*(3), 691–700.

Xia, J., R. D. Miller, C. B. Park, and G. Tian (2003), Inversion of high frequency surface waves with fundamental and higher modes, *Journal of Applied Geophysics*, *52*(1), 45–57, doi:https://doi.org/10.1016/S0926-9851(02)00239-2.

Yamanaka, H., and H. Ishida (1996), Application of genetic algorithms to an inversion of surface-wave dispersion data, *Bulletin of the Seismological Society of America*, *86*(2), 436–444.

Yao, H., Z. Ren, J. Tang, R. Guo, and J. Yan (2023), Trans-dimensional bayesian joint inversion of magnetotelluric and geomagnetic depth sounding responses to constrain mantle electrical discontinuities, *Geophysical Journal International*, *233*(3), 1821–1846.

Yuan, L., and L. Zhou (1998), Sensitivity coefficient evaluation of an embedded fiber-optic strain sensor, *Sensors and Actuators A: Physical*, *69*(1), 5–11, doi:10.1016/S0924-4247(97)01742-1.

Yust, M. B., B. R. Cox, J. P. Vantassel, P. G. Hubbard, C. Boehm, and L. Krischer (2023), Near-surface 2d imaging via fwi of das data: An examination on the impacts of fwi starting model, *Geosciences*, *13*(3), 63.

Zhang, H., and Z. Wu (2007), Development of no-slip optic fibers as Brillouin scattering based distributed sensors, *The Proceedings of the Symposium on the Motion and Vibration Control*, *2007.10*, 91–96, doi:10.1299/jsmemovic.2007.10.91.

Zhang, X., F. Hansteen, A. Curtis, and S. De Ridder (2020), 1-d, 2-d, and 3-d monte carlo ambient noise tomography using a dense passive seismic array installed on the north sea seabed, *Journal of Geophysical Research: Solid Earth*, *125*(2), e2019JB018,552.

Zhang, Y. X., S. Y. Fu, Y. S. Chen, Z. W. Ding, Y. Y. Shan, F. Wang, M. M. Chen, X. P. Zhang, and Z. Meng (2019), A visibility enhanced broadband phase-sensitive OTDR based on the UWFBG array and frequency-division-multiplexing, *Optical Fiber Technology*, *53*, 101,995, doi:https://doi.org/10.1016/j.yofte.2019.101995.

Zulic, S., E. Sidenko, A. Yurikov, K. Tertyshnikov, A. Bona, and R. Pevzner (2022), Comparison of amplitude measurements on borehole geophone and das data, *Sensors*, *22*, doi:10.3390/s22239510.

List of acronyms

AS	Along-strip
BOFDA	Brillouin Optical Frequency Domain Analysis
BOTDA	Brillouin Optical Time Domain Analysis
BS	Broadside
CMP	Common-mid point
CRG	Common-receiver Gather
CSG	Common-source Gather
DAS	Distributed Acoustic Sensing
DVS	Distributed Vibration Sensing
FBG	Fibre Bragg Gratting
FK	Frequency-Wavenumber
HWC	Helically Wound Cable
HWF	Helically Wound Fibre
IL	Inline
KNMI	Royal Netherlands Meteorological Institute
Low-PR	Low Poisson's ratio
LP	Linearly polarised
MASW	Multi-channel Analysis of Surface Waves
MOPA	Multi-offset Phase Analysis
NMO	Normal move-out
OTDR	Optical Time Domain Reflectometer
PSD	Power Spectral Density
PWS	Phase-weighted stacking
RMS	Root Mean Square

SF	Straight Fibre
UTC	Universal Time Coordinated
VSP	Vertical Seismic Profiling
Zero-PR	Zero Poisson's ratio

Curriculum Vitæ

Musab Mansoor Khalfan Al Hasani

11-10-1992   Born in Muscat, Oman.

Education

2009–2015   General Diploma Certificate
             Al Muhanna Bin Sultan School, Muscat, Oman

2010–2015   B.Sc. in Geophysics
             Sultan Qaboos University, Muscat, Oman

2016–2018   M.Sc. in Geophysics
             Curtin University, Perth, Australia

Thesis: Optimising geophone placement for land seismic measurements

Supervisor: Dr. Timothy Dean

2018–2023   Ph.D. research
             Delft University of Technology, Delft, Netherlands

Promotors: Dr. ir. G.G. Drijkoningen and Prof. dr. ir. C.P.A. Wapenaar

Sponsorship and Employment

2016–present   PDO Scholar linked to the Exploration department,
                Petroleum Development Oman (PDO)

List of publications

■ **Peer-reviewed publications**

[**2**] **Al Hasani, M.** and G. Drijkoningen, (2023), *Experiences with Distributed Acoustic Sensing using both straight and helically wound fibres in surface-deployed cables — a case history in Groningen, the Netherlands*, GEOPHYSICS, 88 (6).   Chapter 4 of this thesis

[**1**] Dean,T., **M. Al Hasani**, (2020),*Seismic noise in an urban environment*, The Leading Edge, 39 (9).

■ **Conferences and workshops**

[**6**] **Al Hasani, M.**, G. Drijkoningen, (2022), *Possibilities of DAS for near-surface seismic using straight and helically wound fibres: a pilot field experiment in Groningen, the Netherlands*, SEG workshop: Near-surface modelling and imaging, Muscat, Oman.

[**5**] **Al Hasani, M.**, G. Drijkoningen, K. Wapenaar, (2022), *On the multi-component information of DAS for near-surface seismic: a pilot field experiment in the Groningen area*, EGU General Assembly Conference Abstracts, EGU22-2563.

[**4**] **Al Hasani, M.**, G. Drijkoningen, (2021), *Near-surface seismic characterization using Distributed Acoustic Sensing with a combination of helically wound and straight Fibres: a pilot field experiment in Groningen area*, AGU Fall Meeting Abstracts 2021, NS23A-04.

[**3**] Dean, T., **M. Al Hasani**, (2018), *Spectral characteristics of seismic noise recorded in an urban environment*, EAGE Extended Abstracts.

[**2**] Dean, T., A. Shem, **M. Al Hasani**, (2018), *Methods for reducing unwanted noise (and increasing signal) in passive seismic surveys*, ASEG Extended Abstracts 2018.

[**1**] Dean, T., **M. Al Hasani**, (2018), *Noise in urban land seismic surveys*, ASEG Extended Abstracts 2018.

Ackowledgements

making this journey pleasant and I wish all the best. Thank you **Pieter** for making the PhD thesis template openly available.

During my stay in the Netherlands, I met my nice neighbour **Yasshin** who spoiled me with pastries and cookies he baked. On many Fridays, I enjoyed the company of a group of Omani expats in HOME cafe (Den Haag). The conversations I had with **Al Ghammari**, **Saud** and others were enriching.

Thank you to my beloved parents, and all nine dear siblings for their endless support. Without it, this journey would have been much more difficult. I am grateful to my friends here in Muscat who kept in touch in those years. My lovely wife, **Amira**, thank you for your unconditional love, patience and support. I am sure that you are as happy as I am, if not more, that I have got to this point.

Musab Al Hasani,
Muscat, cloudy Tuesday (32°),
2023.